4. SITE 717[1]

Shipboard Scientific Party[2]

HOLE 717A

Date occupied: 10 July 1987

Date departed: 10 July 1987

Time on hole: 3.75 hr

Position: 0°55.785'S, 81°23.408'E

Water depth (sea level; m, bottom felt): 4734.7

Penetration (m): 9.5

Number of cores: 1

Total length of cored section (m): 9.5

Total core recovered (m): 9.64

Core recovery (%): 101

Deepest sedimentary unit cored:
Depth sub-bottom (m): 5.5
Nature: micaceous silts and calcareous clays
Age: Quaternary
Measured vertical sound velocity (km/s): 1.55

HOLE 717B

Date occupied: 10 July 1987

Date departed: 10 July 1987

Time on hole: 2.75 hr

Position: 0°55.785'S, 81°23.408'E

Water depth (sea level, m, bottom felt): 4734.7

Penetration (m): 13.5

Number of cores: 2

Total length of cored section (m): 13.5

Total core recovered (m): 13.43

Core recovery (%): 99.6

Deepest sedimentary unit cored:
Depth sub-bottom (m): 5.5
Nature: micaceous silts and calcareous clays
Age: late Quaternary
Measured vertical sound velocity (km/s): 1.55

HOLE 717C

Date occupied: 10 July 1987

Date departed: 19 July 1987

Time on hole: 9.6 days

Position: 0°55.785'S, 81°23.408'E

Water depth (sea level, m, bottom felt): 4734.7

Penetration (m): 828.2

Number of cores: 91

Total length of cored section (m): 814.8

Total core recovered (m): 480.2

Core recovery (%): 58.9

Deepest sedimentary unit cored:
Depth sub-bottom (m): 533.2
Nature: silt and silt mud turbidites
Age: late Miocene
Measured vertical sound velocity (km/s): 1.7 to 2.0

SITE 717 SUMMARY

Principal Results: The stratigraphic section recovered at Site 717 ranges from late Quaternary to the base of the late Miocene and has been divided into five main lithologic units. The dominant lithologies and ages of the stratigraphic sequence are as follows:

Unit I (0–5.5 mbsf): Muds, mud turbidites and pelagites of Holocene to latest Pleistocene age.

Unit II (5.5–152.0 mbsf): Micaceous silty turbidites with thin intervening muds and calcareous clays of late Pleistocene age.

Unit III (152.0–303.2 mbsf): Biogenic mud turbidites and mud turbidites with thin interbedded pelagic clays of Pleistocene and late Pliocene age.

Unit IVA (303.2–340.8 mbsf): Silt turbidites with thin muds and mud turbidites of late Pliocene age.

Unit IVB (340.8–456.0 mbsf): Mud turbidites with interbedded pelagic clays of late Pliocene to late Miocene age.

Unit IVC (456.0–465.2 mbsf): Silt and silt to mud turbidites with minor amounts of mud of late Miocene age.

Unit IVD (465.2–533.2 mbsf): Mud turbidites with interbedded pelagic clays of late Miocene age.

Unit V (533.2–828.2 mbsf): Silt and silt to mud turbidites with rare intervals of pelagic clay and organic rich mud turbidites of upper Miocene age.

Sedimentation at Site 717 is dominated by fan sedimentation processes and consists mainly of a sequence of turbidites. A thin layer of mud (5.5 m) overlies a sequence dominated by micaceous silt turbidites which accumulated very rapidly during the late Pleistocene at a rate probably in excess of 350 m/m.y. This unit comprises a distinctive seismic stratigraphic unit which in places truncates lower reflectors. These coarser grained, rapidly deposited turbidites may reflect the Pleistocene sea-level lowstand. Units III and IV together represent a thick section of mainly mud turbidites with thin interbedded pelagic clays that accumulated at a slower average rate of about 70 m/m.y. through the latest Miocene and upper Pliocene. Distinctive green, biogenic turbidites characterize Unit III and at least two pulses of coarser silty turbidites occur in Unit IV. The lowest unit consists of a monotonous sequence of micaceous silt and silt-mud turbidites separated by intervals of muds and pelagic clays. The average accumulation rate for the whole of this unit is 90–100 m/m.y.

The sequence of lithostratigraphic units at Site 717 gives a very good record of sedimentation on the distal fan showing the nature, thickness, and vertical succession of turbidites that have been transported over 2500 km. At least three different sources of turbidites can be tentatively identified: silts and muds from the Ganges-Brahmaputra delta, dark-gray organic rich muds from the upper slope of the Bay of Bengal, and greenish biogenic turbidites probably from the Afanasy-Nitikin Seamount group. One of the main controls on sedimentation appears to have been sea-level variation. A second important factor w as probably changes in rates of erosion related to Himalayan uplift history. Local tectonic effects, perhaps related to

[1] Cochran, J. R., Stow, D.A.V., et al., 1988. *Proc. ODP, Init. Repts.*, 116: College Station, TX (Ocean Drilling Program).
[2] Shipboard Scientific Party is as given in the list of Participants preceding the contents.

the intraplate deformation, may have resulted in the more local supply of biogenic turbidites from adjacent seamounts.

The biostratigraphic control at Site 717 is based primarily on nannofossils. The site has clearly been close to or below the carbonate compensation depth for at least the past 10 m.y. Siliceous microfossils are almost completely absent in spite of the location of the site within the supposed equatorial high-productivity zone.

Site 717 successfully established a reference section for comparison with other sites higher up the fault blocks. There is some evidence, from physical property measurements, of horizontal stress but the heat flow is normal for 78-Ma crust and a complete sedimentary sequence was recovered with no marked unconformities. The seismic unconformity that appears to mark the onset of intraplate deformation occurs within Unit V and does not correspond to a change of lithology. Interpolation between well established paleontological dates gives an age of 7.5 Ma for the beginning of the deformation.

BACKGROUND AND OBJECTIVES

Background

Site 717 is one of three closely-spaced sites located near 1°S, 81°24′E in the central Indian Ocean approximately 800 km south of Sri Lanka and 200 km northwest of the Afanasy Nitikin Seamount group (Fig. 1). It lies at the distal end of the Bengal Fan within a large area of intraplate deformation that affects both the ocean crust and the thick pile of overlying sediments.

Both deposition and deformation in this part of the central Indian Ocean have been affected by the collision between the Indian and Asian plates. This plate interaction began in the Eocene at anomaly 22 time (approximately 53 Ma ago) with a *soft collision*, possibly between continental India and an island arc lying seaward of Asia. This collision led to a halving of the spreading rate to 4 cm/yr (Sclater and Fisher, 1974; Curray et al., 1982). A regional unconformity observed on the proximal and mid fan areas (Curray and Moore, 1971) has been dated to this time by extrapolation from DSDP Site 218 (Moore et al., 1974).

During the Oligocene, the spreading rate decreased still further to 2.5 cm/yr, the spreading direction of the Southeast Indian Ridge changed from N-S to NE-SW (Sclater et al., 1976), and sedimentation in the area now covered by the Bengal Fan probably increased. The *hard* continent–continent collision may have occurred at that time, although other estimates are as late as late Miocene (Powell and Conaghan, 1973). A second prominent regional unconformity in the area of the Bengal Fan has also been dated as late Miocene by drilling at DSDP Site 218 (Thompson, 1974). The unconformity marking the onset of deformation in the distal fan is inferred by extrapolation to be this same event (Weissel et al., 1980).

Rapid terrigenous sedimentation on an incipient Bengal Fan began in the Eocene as a response to the first interplate collision (Curray and Moore, 1971), and has continued to the present day, constructing the world's largest submarine fan—over 2500 km long and over 12 km thick—under the northern Bay of Bengal. In the area of Site 717, the sediment is approximately 1.5–2 km (2 s) thick under the very distal part of the fan. This enormous volume of sediments is assumed to have been derived principally from denudation of the uplifting Himalayan Mountains and then supplied to the delta front via the Ganges-Brahmaputra river system.

Sediments are funneled very efficiently to the fan via a delta-front trough, the "Swatch of No Ground." This trough is presently connected to only one active fan channel, but has been effectively cut off from rapid sediment supply since the most recent rise in sea level, probably about 7,000–10,000 yr ago. The fan channel appears to terminate some 50–100 km north of Site 717, and no channel or levee-type features have been observed on seismic reflection records in the Leg 116 study area.

The increased resistance to subduction and to shortening across the Himalayas since the continent-continent collision, combined with continued spreading on the southeast Indian Ridge, has placed the central Indian Ocean under a large north–south compressive stress regime (Stein and Okal, 1978). As a result, the ocean crust and most of the overlying sediments have been deformed into long-wavelength (100–300 km) undulations with peak-to-trough amplitudes of 1–3 km over a large area, which extends roughly from the the Chagos-Laccadive Ridge in the west to the Ninetyeast Ridge and from 5°N to 10°S latitude (Weissel et al., 1980; Geller et al., 1983).

Superimposed on the long-wavelength undulations are faulted and rotated blocks, 5–20 km wide, interpreted as showing a reverse sense of displacement on the faults separating them (Geller et al., 1983), which is consistent with north–south shortening. The top of the ocean crust is seen to be offset across these faults by up to 0.5 s (> 500 m) on seismic reflection records (Fig. 2). The lower portion of the sedimentary sequence is deformed along with the basement. A prominent unconformity separates the predeformation sequence from an upper syndeformation sequence, which thins towards the tops of blocks and shows pinching out of individual beds.

Objectives

Site 717 is located in 4730 m water depth within the thickest sedimentary section between adjacent fault-block highs (Fig. 2). On the seismic reflection records, the unconformity noted higher up the tilted block becomes conformable in the thicker section, which appears to show continuous sedimentation without marked discontinuities or deformation. The principal objectives of the Site were:

1. To establish a reference hole in the area, for comparison with the other sites where the section is less complete, and to calibrate the regional seismic stratigraphy to a depth of about 800 m;
2. To measure the physical and hydrological properties in an undisturbed area;
3. To characterize the main lithofacies and determine the depositional processes responsible;
4. To establish the provenance of sediments on the distal fan and to assess to what extent compositional variations reflect the uplift history of the Himalayas; and
5. To characterize the nature of early diagenesis in the reference section of fan sediments.

OPERATIONS

JOIDES Resolution sailed from the port of Colombo, Sri Lanka, at 1715 hr local time, 7 July 1987, to begin Leg 116. The magnetometer was deployed after crossing the Sri Lanka continental shelf and the ship proceeded directly to Site 717. A distance of 882 km (476 nmi) was covered in 36.5 hr at 13.04 kt. At 0545 hr, 9 July 1987, the ship slowed to deploy the seismic gear and began a site survey. A seismic line was run from north to south 6 km to the east of the site and a parallel line was run back to the north over the proposed locations of all three Leg 116 sites. The beacon was dropped at 1115 hr, 9 July 1987, at 00°55.785′S, 81°23.408′E. By 1230 hr the ship was on location and began setting pipe.

The first APC core from Hole 717A was brought on deck at 0305, 10 July 1987. A full 9.64-m core was recovered, indicating that the bit had been below the mud line. The ship was moved and Hole 717B spudded in at 0345 hr. The first two APC cores penetrated 13.5 m, recovering 13.43 m of sediment. However,

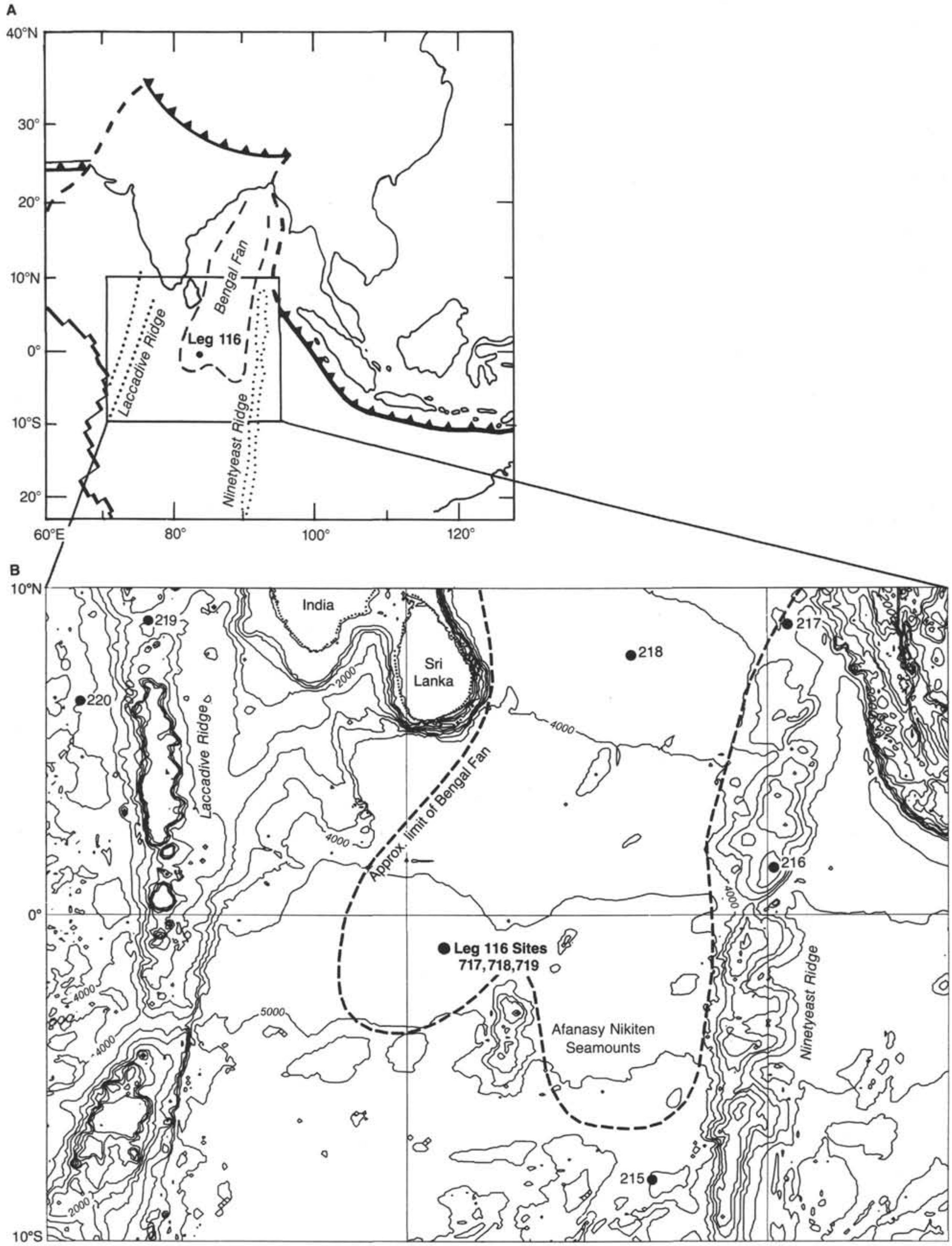

Figure 1. Location maps for the Leg 116 sites. A. Setting of Leg 116 sites relative to tectonic elements of the eastern Indian Ocean. Heavy solid line represents mid-ocean ridge axes, dashed lines are transform plate boundaries and saw-tooth pattern shows convergent plate boundaries. B. Setting of Leg 116 sites within the north central Indian Ocean. Bathymetry is machine-contoured DBDB10 gridded data set at 500-m intervals. Location of other DSDP drill sites within the region is also shown.

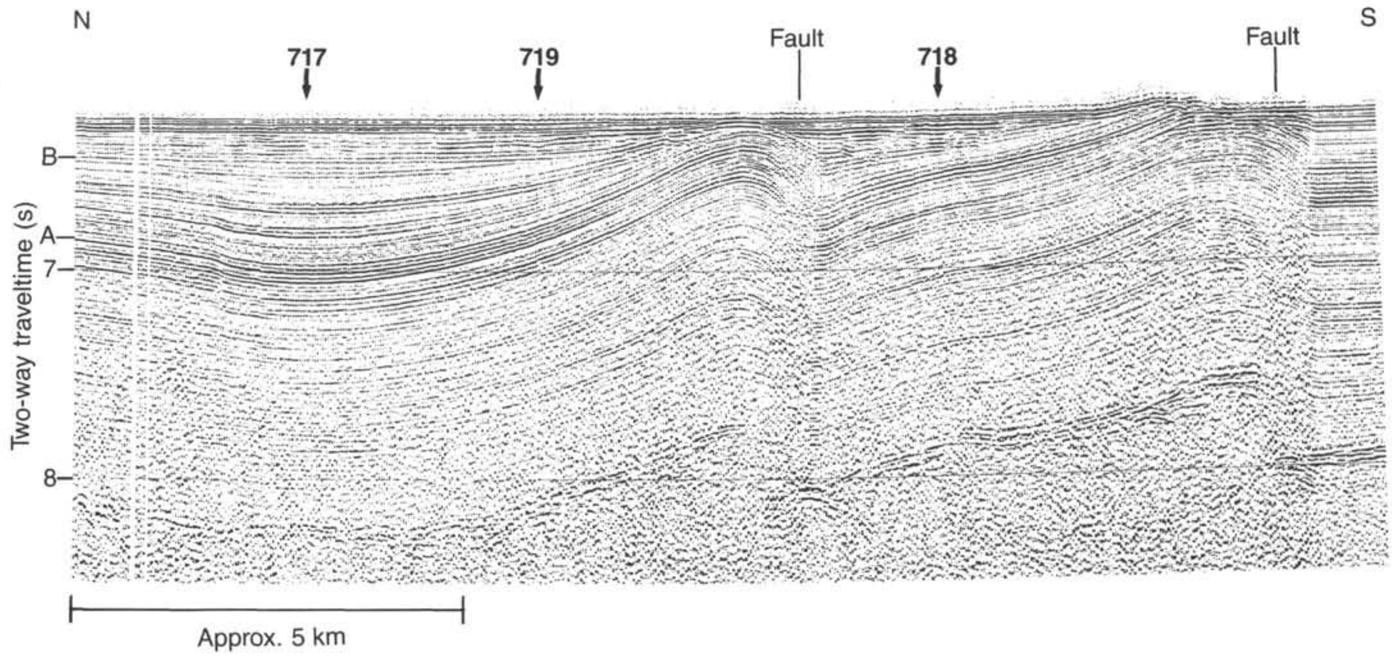

Figure 2. North–South seismic reflection profile across the Leg 116 drill sites. Locations of Sites 717, 718, and 719 are shown. Also noted are the locations of the faults bounding the tilted blocks and prominent unconformities "A" and "B".

on the third APC core, the core barrel was snapped with the loss of an APC heat flow shoe.

The ship was moved forward 10 m and Hole 717C spudded in at 0800 hr, 10 July 1987, and washed down to 13.5 m. At Hole 717C, Core 116-717C-3H came up with the core barrel bent. It was concluded that the bottom consists of a layer of soft clay on top of hard fine sand that could not be penetrated by the APC system. Therefore, at 17.5 mbsf APC coring was terminated and the XCB deployed. Continuous coring with the XCB continued to a depth of 828.2 mbsf, setting a record for XCB penetration. The last core was brought on deck at 1100 hr, 16 July 1987. Recovery in clay and mud turbidites was generally excellent. Recovery in turbidites with quantities of silt and fine sand was generally quite poor. A total of 814.7 m was cored at Site 717C with a recovery of 480.2 m or 58.9%. The details of the coring operation are given in Table 1.

The hole was then conditioned, the bit released, and the drill pipe picked up to 66 mbsf in preparation for logging. The Schlumberger logging tools were prepared and the side entry sub (SES) was installed. The tools did not function properly and it was necessary to lay them on the deck for testing and repair. After 14 hr of work the tools and SES were finally ready for deployment. The logging tools were run down the pipe to a wireline measurement of 4735 m, at which point they would not go any further. The sonic tool indicated that the tool string was not in the pipe.

The logging tools and SES were recovered and the drill pipe pulled. It was found that the bottom hole assembly (BHA) was missing below the bottom of the top drill collar. The logging tools had appearently gone out the bottom of the pipe and hit the seafloor. The reason for the parting of the BHA is not known. No additional logging operations were possible at Hole 717C so the ship got underway for the next site at 2116 hr, 19 July 1987.

LITHOSTRATIGRAPHY

Lithofacies

The stratigraphic sequence penetrated at Site 717 consists predominantly of interbedded clays, silty clays, and silts, with lesser amounts of sandy silts and calcareous clay, ranging in age from Quaternary to late Miocene. The sediments can be divided into seven distinct facies on the basis of texture, sedimentary and biogenic structures, color, organic carbon content, and the presence or absence of calcareous microfossils.

Facies 1. Silt and Silt-Mud Turbidites. (F1)

Facies 1 consists of sharp-based, upward-fining beds of dark-gray silt, or less commonly sandy silt, which grade upward through silty clay to clay. Internally the beds may be massive or rarely show a faint horizontal lamination in the basal few centimeters (e.g., Sample 116-717B-2H-3, 60–112 cm) (Fig. 3). The beds of this facies range from 7–140 cm thick, averaging 40 cm. Bioturbation and calcareous microfossils are rare.

Facies 2. Organic-poor Mud Turbidites. (F2)

Facies 2 consists of sharp-based, thickly to very thickly (30–220 cm) bedded, light-gray to gray, silty clays which pass upward into clay. Typically silt comprises only 10% of the sediment and is concentrated in the lowermost third of the beds. The bases of beds are often marked by clean silt laminae, one grain diameter to several millimeters thick. The silt fraction consists mainly of quartz with mica (less than 10%) and feldspar (traces). Plant debris ranges from zero to 1%. Bioturbation and calcareous microfossils are largely absent.

Facies 3. Organic-rich Mud Turbidites. (F3)

Facies 3 is characterized by large amounts (2%–15%, avg. 5%) of plant debris and consists of very dark-gray to black, sharp-based, upward-fining beds 50–100 cm thick (avg. 80 cm) of silty clay. The beds generally commence with silty clay (less than 80% silt) and pass upward into clay. Typically the basal few centimeters exhibit a horizontal lamination that passes upward into a faint wispy lamination and finally into a massive interval. Pyrite (after wood, burrows, and as concretions) is ubiquitous (see below). The tops of the beds are commonly bioturbated.

Facies 4. Biogenic Mud Turbidites. (F4)

This facies consists of sharp-based, upward fining, olive-gray calcareous silty clays (with a silt content less than 10%) and clay. Beds of this facies range in thickness from 10 to 290 cm (avg. 50 cm). A thin (less than 3 cm) basal silt layer may occur. Rarely, a faint horizontal lamination is present but most commonly the beds appear massive. In contrast to the other facies (with the exception of the basal silts of Facies 6) calcareous microfossils (mainly nannofossils, but with common foraminifers) are ubiquitous, making up to 20% of the sediment. In addition, unidentified calcareous silt and clay-sized material accounts for 20 to 30% of the sediment. The tops of the beds are commonly bioturbated.

Facies 5. Pelagic Clays. (F5)

This facies consists of gradationally based beds of clay 5 to 25 cm thick, varying in color from a mottled red-green to gray. Bioturbation and ferromanganiferous(?) chemical fronts characterize the facies. Calcareous microfossils are rare to absent; those that remain show evidence of extreme dissolution.

Facies 6. Pelagic Calcareous Clays. (F6)

Facies 6 consists of light to dark-gray bioturbated clays with approximately 5% silt. It is characterized by an abundant fauna of nannofossils (up to 50%) and foraminifers (up to 5%). Bioturbation is common and intense.

Facies 7. Structureless Muds. (F7)

Facies 7 consists of beds (2–100 cm thick) of dark to light-gray silty clay and clay with indistinct bed boundaries. The beds may or may not be bioturbated. Ferromanganiferous(?) chemical fronts are absent. Calcareous microfossils are largely absent but occasionally occur in trace amounts.

Lithologic Units

On the basis of the distribution of these facies the sedimentary sequence penetrated at Site 717 has been divided into five lithologic units, with Unit IV being divided into four subunits (Fig. 4).

Unit I. Cores 116-717B-1H and 116-717B-2H; 0 to 5.5 mbsf

Unit I is 5.5 m thick and is composed of interbedded structureless muds (F7), organic-poor mud turbidites (F2), and calcareous clays (F6).

Unit II. Cores 116-717B-2H to 116-717C-20X; 5.5 to 152 mbsf

Unit II consists of 146.5 m of predominantly facies 1 silt and silt-mud turbidites, with thin interbeds of structureless muds (F7) and calcareous clay (F6).

Unit III. Cores 116-717C-20X to 116-717C-36X; 152 to 303.2 mbsf

Unit III is 151.2 m thick and is characterized by the presence of biogenic mud turbidites (F4), which decrease in abundance with depth through the unit. Interbedded with the biogenic mud turbidites are organic-poor (F2) and organic-rich mud turbidites (F3), together with structureless muds (F7) and pelagic clays (F5). The latter tend to occur as thin caps on both turbidite facies.

Unit IV. Cores 116-717C-36X to 116-717C-60X; 303.2 to 533.3 mbsf

This unit has been subdivided into four subunits on the basis of the presence, abundance and thickness of silt and silt-mud turbidites.

Subunit IVa. Cores 116-717C-36X to 116-717C-39X; 303.2 to 340.8 mbsf

Subunit IVa is 37.6 m thick and is characterized by an abundance of facies 1, silt turbidites (Fig. 3), although thin structureless muds (F7) and mud turbidites of Facies 2 and 3 also occur.

Subunit IVb. Cores 116-717C-40X to 116-717C-52X; 340.8 to 456 mbsf

Subunit IVb is 115.2 m thick and consists of interbedded organic-rich (F3) and organic-poor (F2) mud turbidites, structureless muds (F7) and pelagic clays (F5), differing from Unit III in that the biogenic mud turbidites (F4) are absent, and that rare silt-mud turbidites (F1) occur.

Subunit IVc. Cores 116-717C-52X to 116-717C-53X; 456 to 465.2 mbsf

Subunit IVc is 9.2 m thick and is characterized by the abundance of silt and silt-mud turbidites (F1) with minor amounts of structureless mud (F7).

Subunit IVd. Cores 116-717C-53X to 116-717C-60X; 465.2 to 533.2 mbsf

Subunit IVd is 68 m thick and is broadly similar to Subunit IVb, the only difference being the presence of rare, thin calcareous clays (F6).

Unit V. Cores 116-717C-60X to 116-717C-91X; 533.2 to 828.2 mbsf

This unit is a monotonous sequence (295 m thick) of predominantly silt and silt-mud turbidites (F1) with rare, thin intervals of pelagic calcareous clay (F6), structureless mud (F7), and organic-rich mud turbidites (F3).

Maximum Quartz Grain Size

Maximum grain size was determined at approximately 10-m intervals at Site 717. In each case the coarsest and/or thickest lithology in the individual core (generally from the base of the coarsest turbidite) was chosen for smear-slide analysis and the largest equant quartz grain measured. Results of the analysis are shown graphically in Figure 5.

The analysis reveals that the maximum grain-size range is from 30 to 440 μm (coarse silt to medium sand on the Wentworth Scale). Not surprisingly the coarsest maximum grain size corresponds to the sandy silt and silt turbidites of Facies 1 within Units II and V and Subunits IVa and IVc. However, the background values throughout the sequence show that coarse silt-sized material was able to reach this most distal fan setting via turbidity currents throughout the interval from the late Miocene to the Quaternary sampled at Site 717.

Carbonate Content

Results of analysis of carbonate content at Site 717 is shown in Figure 6. The graph reveals a slight increase with depth. Superimposed on this general trend are two facies effects. First, the coarser facies show higher carbonate contents than adjacent finer lithologies (with the exception of Facies 4) reflecting either diagenetic carbonate precipitation or the presence of transported(?) biogenic carbonate. Second, the few very high values correspond to the biogenic mud turbidite facies (F4) reflecting their high biogenic calcite content.

Pyrite Occurrence

Pyrite is ubiquitous in Facies 3. It appears most commonly as tube fillings 1–2 mm in diameter, 5 to more than 20 mm long,

Table 1. ODP Site 717 coring summary.

Hole	Core no.	Date (July 1987)	Time	Top (mbsf)	Bottom (mbsf)	Meters cored (m)	Meters recovered (m)	Percent recovery
A	1H	10	0305	0.0	9.5	9.5	9.64	101.0
						9.5	9.64	
B	1H	10	0405	0.0	4.0	4.0	4.00	100.0
B	2H	10	0455	4.0	13.5	9.5	9.43	99.2
						13.5	13.43	
C	1W	10	0715	0.0	13.5		0.00	0.0
C	2H	10	0835	13.5	17.5	4.0	2.82	70.5
C	3X	10	1030	17.5	27.0	9.5	0.03	0.3
C	4X	10	1145	27.0	36.5	9.5	0.64	6.7
C	5X	10	1315	36.5	46.0	9.5	1.94	20.4
C	6X	10	1445	46.0	55.5	9.5	2.35	24.7
C	7X	10	1630	55.5	65.0	9.5	2.15	22.6
C	8X	10	1810	65.0	74.5	9.5	2.58	27.1
C	9I	10	2045	74.5	74.5	0.0	0.00	
C	10X	10	2200	74.5	84.0	9.5	1.83	19.2
C	11X	10	2330	84.0	93.5	9.5	0.08	0.8
C	12X	11	0105	93.5	103.0	9.5	0.12	1.3
C	13I	11	0305	103.0	103.0	0.0	0.00	
C	14X	11	0420	103.0	112.5	9.5	2.82	29.7
C	15X	11	0545	112.5	122.0	9.5	2.35	24.7
C	16X	11	0715	122.0	131.5	9.5	1.66	17.5
C	17I	11	0845	131.5	131.5	0.0	0.00	
C	18X	11	1010	131.5	141.0	9.5	0.20	2.1
C	19X	11	1140	141.0	150.5	9.5	1.46	15.3
C	20X	11	1330	150.5	160.0	9.5	5.50	57.9
C	21X	11	1540	160.0	169.5	9.5	6.08	64.0
C	22X	11	1725	169.5	179.0	9.5	7.10	74.7
C	23X	11	1920	179.0	188.5	9.5	9.70	102.0
C	24X	11	2115	188.5	198.0	9.5	9.67	102.0
C	25X	11	2310	198.0	207.5	9.5	7.67	80.7
C	26X	12	0105	207.5	217.0	9.5	9.62	101.0
C	27X	12	0250	217.0	226.5	9.5	9.29	97.8
C	28X	12	0430	226.5	236.0	9.5	8.12	85.5
C	29X	12	0615	236.0	245.5	9.5	9.56	100.0
C	30X	12	0800	245.5	255.0	9.5	9.68	102.0
C	31X	12	0945	255.0	264.5	9.5	3.90	41.0
C	32X	12	1115	264.5	274.0	9.5	7.66	80.6
C	33X	12	1310	274.0	283.5	9.5	9.73	102.0
C	34X	12	1505	283.5	293.0	9.5	5.28	55.6
C	35X	12	1700	293.0	302.5	9.5	9.73	102.0
C	36X	12	1855	302.5	312.0	9.5	9.73	102.0
C	37X	12	2035	312.0	321.5	9.5	4.14	43.6
C	38X	12	2215	321.5	331.0	9.5	5.71	60.1
C	39X	12	2345	331.0	340.5	9.5	1.64	17.2
C	40X	13	0150	340.5	350.0	9.5	9.68	102.0
C	41X	13	0350	350.0	359.5	9.5	0.78	8.2
C	42X	13	0520	359.5	369.0	9.5	9.27	97.6
C	43X	13	0830	369.0	378.5	9.5	9.80	103.0
C	44X	13	1020	378.5	388.0	9.5	9.45	99.5

often vertically oriented and abundant in sections of the core a few centimeters thick. These occurrences are interpreted as burrow fills. They are commonly associated with vertical veinlets (up to 1 mm in diameter) filled by an unidentified (X-ray opaque) material that may represent burrows, gas, water escape pipes, or microfractures. The other occurrences of iron sulfide are: small isolated concretions or nodules, less than 5 mm in size, in brown to dark-gray clays; fine lenses or layers (no more than 2–3 mm thick) of pyritic silt or sandy silt found in clays or sometimes at the bases of layers rich in plant debris; and as replacement of fossils such as plant fragments or occasionally microfossils (especially radiolarians).

Geochemistry of Sediments

Table 2 shows the data generated by X-ray fluorescence analysis, including the sum of the concentrations of the oxides (column TOTAL) and the Loss on Ignition (column LOI). Also shown are the color values assigned to the samples in the Visual Core Descriptions.

The first conclusion we draw from these data is that the ignition technique in use is not completely calcining the calcium carbonate in the carbonate-rich samples. The samples with the four highest CaO concentrations are also the samples whose total weight is least. LOI is also highest for these samples, but is insufficient to explain the discrepancy. Silica and alumina are highly correlated but this is mostly a function of dilution by calcium carbonate. When concentrations are recalculated to a CaO-free basis to remove this dilution effect, silica is weakly inversely correlated with alumina, reflecting variations in the proportions of quartz and alumina-rich clay minerals in the noncarbonate fraction.

There is a moderately significant inverse relationship between Fe_2O_3 and MnO. This probably represents the geochemical separation of iron and manganese in reducing environments, with

Table 1 (continued).

Hole	Core no.	Date (July 1987)	Time	Top (mbsf)	Bottom (mbsf)	Meters cored (m)	Meters recovered (m)	Percent recovery
C	45X	13	1215	388.0	397.5	9.5	9.79	103.0
C	46X	13	1405	397.5	407.0	9.5	5.86	61.7
C	47X	13	1615	407.0	416.5	9.5	4.76	50.1
C	48X	13	1805	416.5	426.0	9.5	9.72	102.0
C	49X	13	1850	426.0	435.5	9.5	6.74	70.9
C	50X	13	2140	435.5	445.0	9.5	9.68	102.0
C	51X	13	2315	445.0	454.5	9.5	6.26	65.9
C	52X	14	0445	454.5	464.0	9.5	4.51	47.5
C	53X	14	0915	464.0	473.5	9.5	9.79	103.0
C	54X	14	1115	473.5	483.0	9.5	9.70	102.0
C	55X	14	1300	483.0	492.5	9.5	4.21	44.3
C	56X	14	1405	492.5	502.0	9.5	9.86	104.0
C	57X	14	1610	502.0	511.5	9.5	9.73	102.0
C	58X	14	1750	511.5	521.0	9.5	7.33	77.1
C	59X	14	1935	521.0	530.5	9.5	9.77	103.0
C	60X	14	2130	530.5	540.0	9.5	3.97	41.8
C	61X	14	2300	540.0	549.5	9.5	3.10	32.6
C	62X	15	0045	549.5	559.0	9.5	1.16	12.2
C	63X	15	0230	559.0	568.5	9.5	3.31	34.8
C	64X	15	0415	568.5	578.0	9.5	4.95	52.1
C	65X	15	0630	578.0	587.5	9.5	8.42	88.6
C	66X	15	0830	587.5	597.0	9.5	6.55	68.9
C	67X	15	1015	597.0	606.5	9.5	3.36	35.3
C	68X	15	1200	606.5	616.0	9.5	8.36	88.0
C	69X	15	1345	616.0	625.5	9.5	4.41	46.4
C	70X	15	1520	625.5	635.0	9.5	9.42	99.1
C	71X	15	1700	635.0	644.5	9.5	8.03	84.5
C	72X	15	1840	644.5	654.0	9.5	3.64	38.3
C	73X	15	2010	654.0	663.5	9.5	2.56	26.9
C	74X	15	2140	663.5	673.0	9.5	2.19	23.0
C	75X	15	2320	673.0	682.5	9.5	5.63	59.2
C	76X	16	0115	682.5	692.0	9.5	6.04	63.6
C	77X	16	0305	692.0	701.5	9.5	9.74	102.0
C	78X	16	0530	701.5	711.0	9.5	9.57	101.0
C	79X	16	0800	711.0	720.5	9.5	9.31	98.0
C	80X	16	0950	720.5	730.0	9.5	5.01	52.7
C	81X	16	1145	730.0	739.5	9.5	1.30	13.7
C	82X	16	1345	739.5	749.0	9.5	1.23	12.9
C	83X	16	1545	749.0	758.5	9.5	1.15	12.1
C	84X	16	1755	758.5	768.0	9.5	4.61	48.5
C	85X	16	2010	768.0	777.5	9.5	9.63	101.0
C	86X	16	2205	775.5	787.0	9.5	0.57	6.0
C	87X	16	2345	787.0	796.5	9.5	3.39	35.7
C	88X	17	0302	796.5	806.0	9.5	1.33	14.0
C	89X	17	0505	806.0	809.2	3.2	0.80	25.0
C	90X	17	0750	809.2	818.7	9.5	2.02	21.2
C	91X	17	1100	818.7	828.2	9.5	6.21	65.3
						814.7	480.20	

manganese migrating to oxidizing environments where it precipitates as MnO_2, and iron migrating to reducing environments where it precipitates as FeS_2 and/or its precursors. Color value and Fe_2O_3 also show a moderately significant correlation; higher Fe_2O_3 leading to darker colors. This is also a function of the abundance of iron sulfide minerals.

The most enigmatic relationship between elements results from comparing the MgO/Al_2O_3 ratio to the K_2O/Al_2O_3 ratio. By normalizing to Al_2O_3, the effects of dilution of the raw concentrations by quartz and calcium carbonate are eliminated, and the variation in the aluminous (presumably clay) phase(s?) can be studied. The MgO in the calcium carbonate component is not important; in fact, CaO and MgO are not correlated in these samples.

The correlation between MgO/Al_2O_3 and K_2O/Al_2O_3 is fairly strong ($r^2 = 0.808$) and unexpectedly, positive. It was expected that an inverse correlation would exist between the two, representing the mixing of Mg-rich, K_2O-poor smectites and K_2O-rich, MgO-poor illites. Phengite, a form of illite, contains magnesium in the octahedral layers, where it substitutes for aluminum. This leads to a positive correlation between MgO/Al_2O_3 and K_2O/Al_2O_3 in phengite, but at compositions much more potash-rich than those measured here. The MgO and K_2O-rich component may be biotite but the correct explanation of the positive correlation between magnesium and potassium in these samples is unknown and awaits a comparison with X-ray diffraction data.

In conclusion, there are three important components in these sediments: calcium carbonate, quartz, and an alumino-silicate phase in which MgO and K_2O are positively correlated. A secondary component is represented by the redox sensitive elements, manganese and iron, which migrate in response to chemical conditions in the pore waters.

Additional data is required for chlorine, which would permit the correction of other concentrations for occluded sea salt, and for sulfur, to help understand the distribution of iron.

BIOSTRATIGRAPHY

General

Site 717 yielded usable silicious microfossils—radiolarians, diatoms, silicoflagellates–only in the upper part of the section,

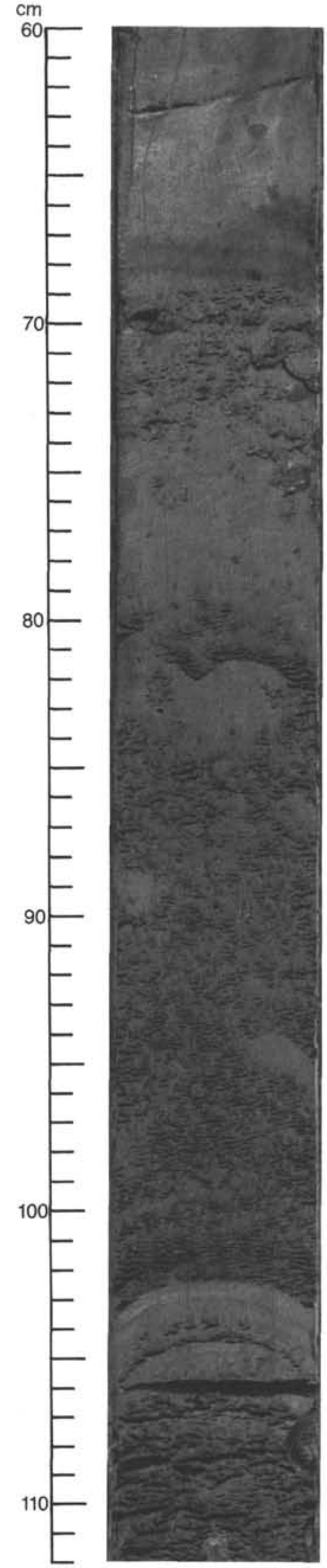

Figure 3. Photograph of a silt-mud turbidite (Sample 116-717B-2H-3, 60–112 cm).

i.e., Cores 116-717B-1H, -717C-26X, and -717C-27X. Radiolarians and silicoflagellates are generally poorly preserved, while diatoms are represented by delicate forms, most of them, however, broken. The siliceous microfossils indicated a Pliocene-Pleistocene age. Pyritized diatoms also were recovered sporadically at several levels in the section. These remains, when complete, can easily be identified to the species level because the extremely fine pyrite coating did not alter the finest structure of the diatom frustules. Low diversity of recovered diatom assemblages is probably caused by selective dissolution of frustules prior to pyritization. Siliceous skeletons of radiolarians and polyaxial sponge spicules are nearly completely replaced with pyrite and yet their fine skeletal structures are preserved.

Calcareous microfossils are found in much of the cored interval but their occurrence is sporadic. They occur most consistently and in greatest abundance, although all of the assemblages are severely corroded, as the residue of the most solution-resistant species. Nevertheless, the biostratigraphy is based primarily on the calcareous nannofossils. Planktonic foraminifers occur more rarely in the section, often together with the calcareous nannofossils, and consist nearly always of corrosion-fragmented specimens of large species, or of very small, possibly juvenile specimens, neither yielding much insight into the history of the sediments at this site. Benthic foraminifers occur more consistently than planktonic species. These too, however, are represented by very small, often extremely delicate species of limited usefulness for interpreting the sediment.

In nearly every sample the redeposition of some micro- and nannofossils is apparent from the age inconsistencies in the assemblage. Therefore, all ages must be suspect to some degree. It is reasonable to think that many of the assemblages are redeposited, probably penecontemporaneously in most instances. Consequently all ages should be considered maximum ages, and the true age may, in fact, be younger than the age assigned to it here.

Radiolarians

Radiolarians are generally absent or poorly preserved throughout the cores at Site 717 and age assignments were not possible for most samples. Age assignment was only possible for the Sample 116-717B-1H, CC which contained an abundant moderately preserved assemblage including the following diagnostic taxa: *Spongaster tetras*, *Theocorythium trachelium trachelium*, *Didymocyrtis tetrathalamas*, *Pterocanium praetextum*, *Lithopera bacca*, *Collosphaera tuberosa*, and *Phormosticoartus corbula*. Although looked for, *Buccinosphaera invaginata* was not found. This sample may be assigned to the *Collosphaera tuberosa* Zone of Quaternary age.

The remainder of the sporadic radiolarian occurrences were concentrated in samples from Cores 116-717C-21X, 116-717C-27X, and 116-717C-29X including the following samples: 116-717C-21X, CC; 116-717C-26X, CC; 116-717C-27X-1, 24–26 cm; 116-717C-27X-5, 12–14 cm; 116-717C-27X-5, 32–34 cm; 116-717C-27X-5, 70–72 cm; 116-717C-27X-5, 91–95 cm; 116-717C-27X-5, 116–118 cm; 116-717C-29X, CC; 116-717C-59X-2, 34–36 cm; 116-717C-59X-4, 11–13 cm. In these samples radiolarian abundances are low and most specimens are fragmented and pyritized, which makes species identification difficult. Among these Sample 116-717C-27X-1, 24-26 cm, contains a moderately diverse assemblage including *Botryocyrtis scutum*, *Cornutella profunda*, *Tetrapyle octacantha*, *Carpocanarium papillosum*, *Spirocyrtis* cf. *subscalaris*, *Carpocanarium* sp. D (Ling, 1975), *Theocalyptra* sp., and several spongodiscid species.

Silicoflagellates

Silicoflagellates were encountered only in three samples, but no definite age assignment can be made. Sample 116-717C-

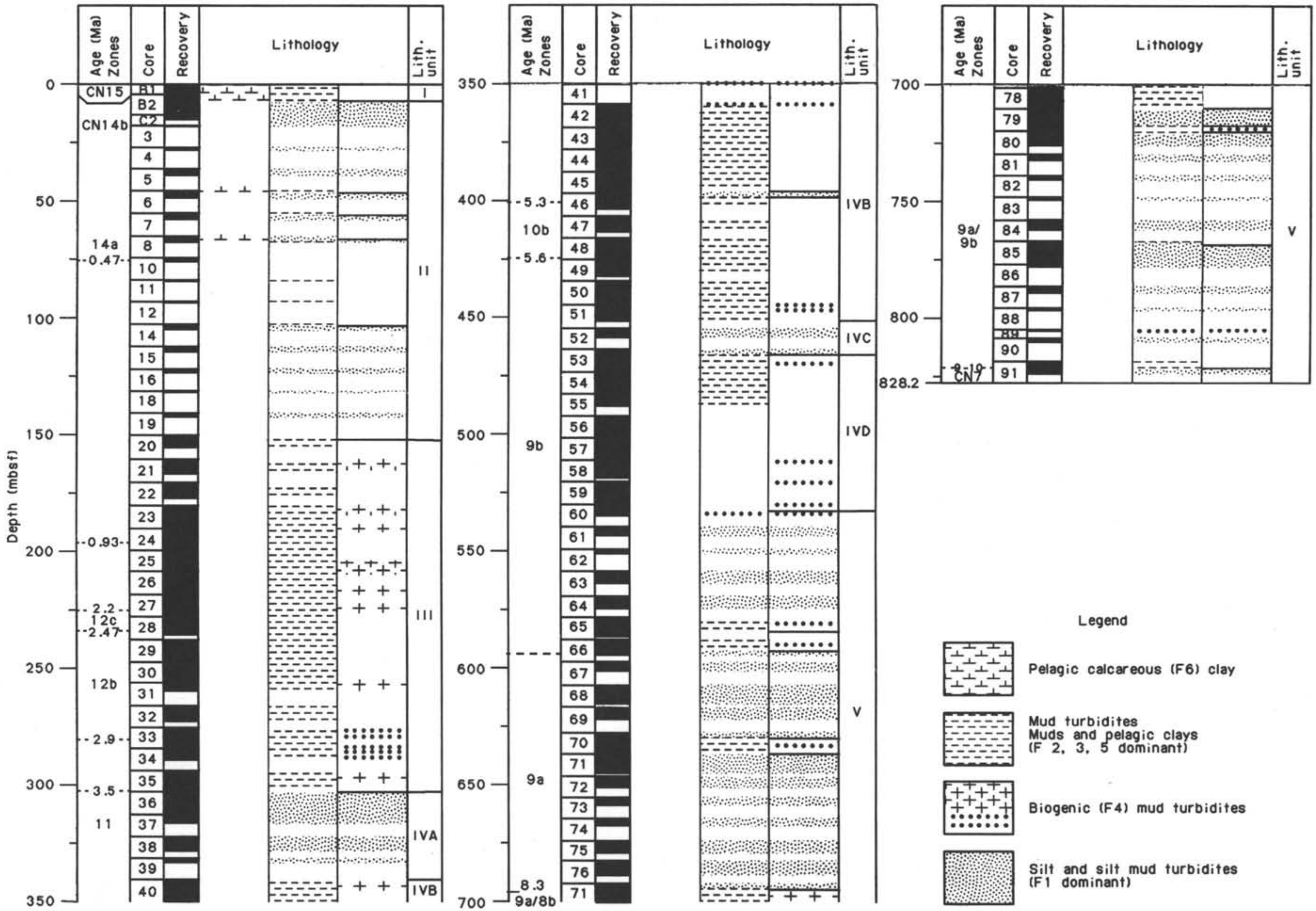

Figure 4. Lithology of Site 717.

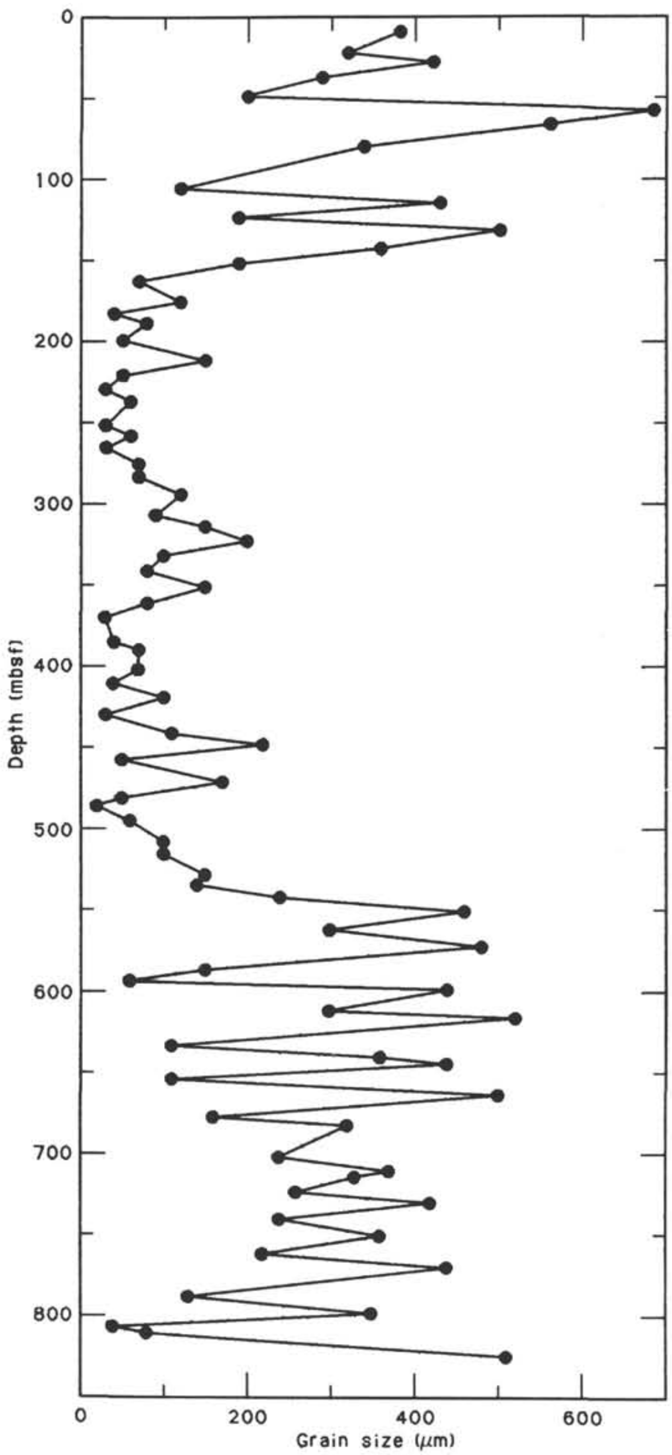

Figure 5. Maximum grain size vs. depth, Site 717.

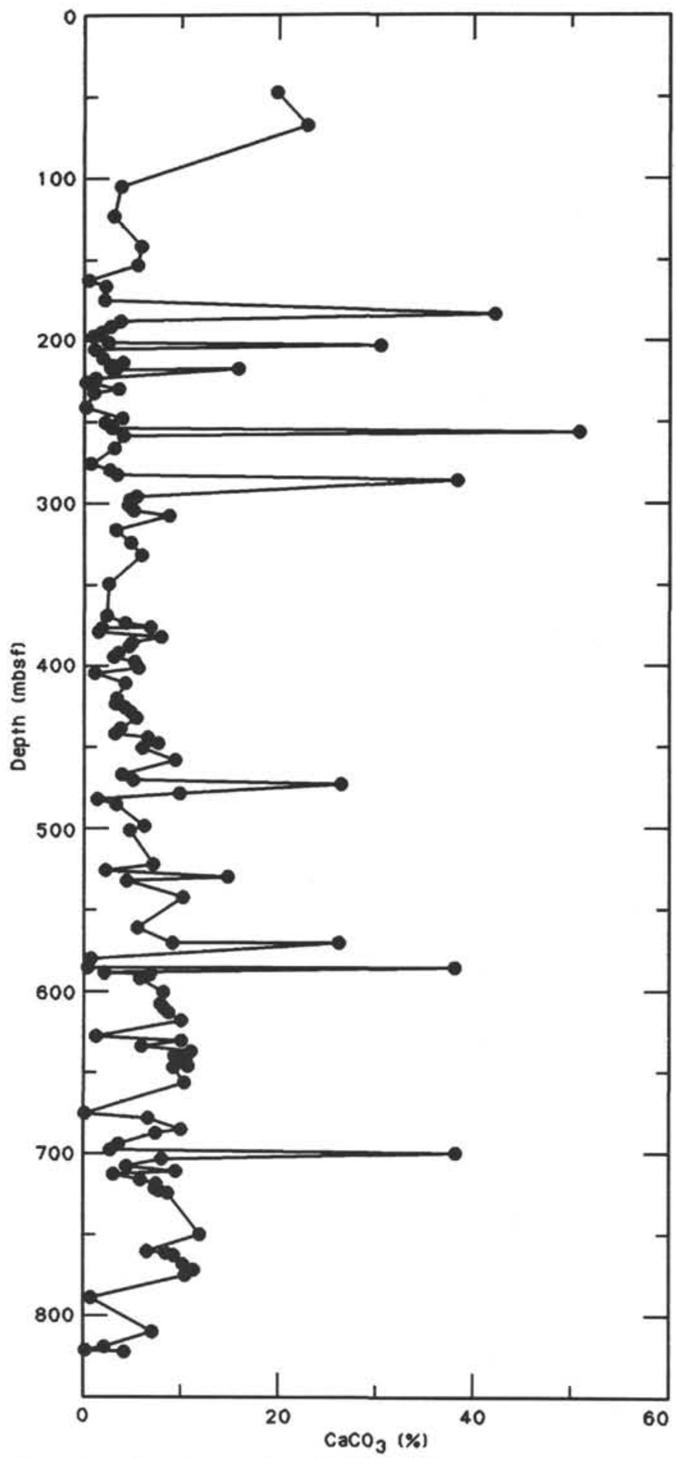

Figure 6. Carbonate content vs. depth, Site 717.

27X-1, 24-26 cm, contains few *Mesocena quadrangula* and rare *Distephanus* sp. A (Perch-Nielsen, 1985) and *Dictyocha longa*. In the Tropical Pacific the first appearance of *M. quadrangula* is in the late Miocene and the species reached an acme in the middle Pleistocene before its disappearance at about 1 Ma. (Bukry, 1985; Locker and Martini, 1986). Sample 116-717C-27X-5, 91-95 cm, contains rare specimens of *Dictyocha*? *delicata*. Sample 116-717C-78X-4, 92-94 cm, contains rare *Dictyocha breviospina ausonia*.

Approximately 50% of silicoflagellate specimens in Sample 116-717C-27X-1, 24-26 cm, and most of those in Samples 116-717C-27-5, 91-95 cm, and 116-717C-78X-4, 92-94 cm, are pyritized. In all three cores silicoflagellates coexist with pyritized radiolarians.

Diatoms

Diatoms are rare to absent in most samples examined from Site 717C. They are present mainly in the soft dark-brown or yellow-green biogenic turbidites along with other siliceous microfossils. Most abundant are spiculae of sponges, endoskeletons of radiolarians, silicoflagellates, ebridians, and occasionally, especially in the upper cores, terrestrial phytolithes. How-

Table 2. Major element X-ray fluorescence analysis data, Hole 717C.

Sample	SiO_2	TiO_2	Al_2O_3	Fe_2O_3	MnO	MgO	CaO	Na_2O	K_2O	P_2O_5	Total	LOI	Color
116-717C-													
28X-5, 90–92	41.22	0.55	12.30	7.66	0.51	2.43	29.19	1.40	1.85	0.28	97.39	23.23	6.0
28X-5, 108–112	20.27	0.24	6.22	3.64	1.35	0.00	64.62	0.00	0.09	1.01	97.44	35.56	7.0
30X-1, 15–19	59.69	0.97	20.42	9.51	0.74	3.51	1.76	1.78	3.86	0.11	102.35	8.30	5.0
30X-1, 126–131	55.90	1.76	20.60	12.57	0.19	2.91	1.85	1.97	2.13	0.11	99.99	12.27	3.0
30X-2, 80–85	53.93	1.61	20.27	12.98	0.18	3.03	2.44	1.88	2.14	0.12	98.58	12.12	2.5
30X-3, 10–15	27.20	0.43	10.44	7.48	0.53	1.07	39.21	1.33	1.13	0.60	89.42	28.02	3.0
30X-3, 105–110	58.91	0.87	19.75	8.63	0.24	3.40	2.73	1.65	3.85	0.13	100.16	8.31	6.0
33X-2, 48–53	65.73	0.81	16.75	6.36	0.18	3.07	2.76	1.65	3.95	0.11	101.37	6.30	5.0
33X-3, 118–123	37.38	0.69	14.60	7.10	0.42	1.35	31.09	1.47	1.51	0.41	96.02	25.46	4.0
33X-5, 21–26	58.30	0.95	20.27	9.46	0.16	3.54	0.83	1.68	4.14	0.14	99.47	7.85	7.0
34X-1, 45–49	59.41	0.94	19.73	8.56	0.18	3.73	1.44	1.82	4.24	0.10	100.15	7.45	5.0
34X-1, 94–98	62.18	0.66	13.38	9.74	0.21	3.15	3.56	1.84	3.29	0.09	98.10	5.36	6.0
34X-2, 94–99	55.35	1.73	22.13	13.80	0.14	2.60	1.28	2.07	1.92	0.10	101.12	19.62	4.0
34X-2, 140–145	61.83	0.82	17.45	8.29	0.16	3.66	2.51	1.68	4.20	0.11	100.71	6.82	6.0
44X-2, 48–53	53.87	1.48	20.79	11.59	0.15	2.44	4.75	1.69	2.22	0.11	99.09	14.13	2.5
45X-6, 130–136	55.52	1.62	22.28	12.56	0.16	2.71	1.08	1.70	2.06	0.09	99.78	13.42	2.5

ever, two samples from Cores 116-717C-26X and 116-717C-27X contain some moderately preserved and fairly abundant diatom frustules of pelagic diatoms. Samples from Cores 116-717C-26X and 116-717C-27X contain an admixture of displaced, neritic diatoms. Below this level only isolated or rare specimens of robust taxa were found (Cores 116-717C-30X, -717C-56X, -717C-59X, -717C-65X, -717C-66X, -717C-70X, -717C-78X, and -717C-82X). With very rare exceptions, especially below the level of Core 116-717C-27X, all diatoms are pyritized.

Few species present in the younger samples (Cores 116-717C-26X to 116-717C-30X); *Actinocyclus divisus*, *Coscinodiscus africanus*, *Thalassiosira oestrupii*, and *Ethmodiscus rex*, have biostratigraphic and paleoceanographic significance even in such a depauperate assemblage. The first three, *A. divisus*, *C. africanus*, and *T. oestrupii*, have been recorded in the Indian and Pacific Oceans from Pleistocene and Pliocene age sediments.

Ethmodiscus rex is well known for its role in formation of the *Ethmodiscus* ooze. Its stratigraphic range is long, but in Indian Ocean sediments it is present in abundance, although intermittently, only during Pleistocene and Pliocene. Therefore, its presence in Hole 717C may reflect its true contribution to the formation of pelagic *Ethmodiscus*-rich sediments down to the level of Core 116-717C-30X. From these originally deposited sediments, only species most abundant and resistant to dissolution were preserved. Therefore, the section including the studied samples of Cores 116-717C-26X to -30X are no older than Pliocene.

In Section 116-717C-78X-4 from the older part of the hole, several fragments and one well-preserved valve of *Coscinodiscus temperi* var. *delicata* were encountered. Stratigraphic distribution of this diatom has been shown to be restricted to the interval 10–12 m.y. in the low-latitude Pacific.

The majority of biogenic siliceous remains in Hole 717C, especially those below 225 mbsf (Core 116-717C-27X), are pyritized; diatoms appear to be covered with a fine pyrite coating revealing the finest structural details. Elemental analysis of pyritized diatoms reveals the presence of silica. It is assumed that pyritization occurred following the onset of postdepositional dissolution of biogenic silica, and the fact that any hydrous siliceous microfossils (diatoms, silicoflagellates) are present at all in these sediments may be due to the pyrite seal.

Foraminifers

Although 170 samples were examined, Hole 717C yielded only a few poor to moderately preserved specimens which allow a biostratigraphic assignment. Unfortunately, these samples are also strongly affected by dissolution and contain only poor-diversity assemblages. Foraminifers are rare or absent in most parts of the sequence. Abundant and well-preserved foraminifer assemblages have been found only in biogenic turbidites.

Pleistocene

The interval 116-717C-1W to -717C-16X, CC, is referred to the Pleistocene, based on the occurrence of *Globoroalia truncatulinoides* in Section 116-717C-16X, CC. The interval below this core down to Core 116-717C-28X is only tentatively referred to the Pleistocene. In fact, the taxa occurring there, *Globorotalia tumida tumida*, *G. menardii*, *G. menardii cultrata*, *Sphaeroidinella dehiscens*, *Neogloboquadrina dutertrei*, *Pulleniatina obliquiloculata*, and *Globigerina conglomerata*, are particularly common in the Pleistocene but not restricted to this epoch, being also present in the Pliocene.

Pliocene

The interval 116-717C-29X-3, 11–13 cm, to 116-717C-47X, CC, yields *Globoquadrina altispira altispira*, *Globigerinoides obliquus*, and *Sphaeroidinellopsis seminulina*, taxa whose range encompasses the late Miocene to early Pliocene. However, Sample 116-717C-40X-3, 52–54 cm yields *Globorotalia margaritae*, which indicated an early Pliocene age (Zones N18–N19).

Miocene

Based on the planktonic foraminifer occurence, a Miocene age is recognized only in two sections: 116-717C-70X, CC, and 116-717C-75X, CC. The latter, which contains *Globigerinoides obliquus extremus*, *G. bulloideus*, *Globigerina nepenthes*, *Globoquadrina altispira altispira*, *Globorotalia* cf. *merotumida*, is referred to the late Miocene with strong certainty.

All the samples downhole from this level are barren or contain very rare foraminifers of no stratigraphic utility.

Environmental Considerations

From the environmental point of view the foraminifer analysis, carried out mainly on the core catchers and on supplementary samples from the cores, gives the following indications:

1. Pelagic oozes (Samples 116-717C-10X-1, 70–72 cm; -717C-22X-5, 37–39 cm; -717C-24X-5, 20–22 cm; -717C-25X-4, 112–114 cm; -717C-38X-4, 40–44 cm) were deposited below the lysocline. They contain mainly fragmented planktonic foraminifer tests and somewhat better-preserved benthic ones. Several other samples completely devoid of planktonic foraminifers, and yielding only few benthic forms together with phosphatic remains or pyritized siliceous tests, are presumed to have been deposited

below the CCD (e.g., Section 116-717C-32X, CC; Sample 116-717C-34X-1, 133–135 cm; Section 116-717C-43X, CC; etc).

2. Downslope displacement is documented by occurrence of (a) shelf benthic foraminifers such as *Ammonia beccarii*, *Elphidium* spp., etc., particularly in the upper part of the sequence (lithologic Units I and II, Sections 116-717C-3X, CC; -717C-4X, CC; -717C-5X, CC; -717C-24X, CC); (b) plant debris, echinoid remains, mollusk fragments; (c) abundant size-selected, very small foraminifers whose good preservation suggests rapid transport and burial (Cores 116-717C-20X to -717C-31X).

3. Evidence of reworking has also been detected in Sections 116-717C-15X, CC; 116-717C-16X, CC; and 116-717C-28X, CC.

Calcareous Nannofossils

Coccoliths, discoasters, and associated forms occur sporadically throughout the section. In some instances they occur in what appear to be thin, pelagic ooze layers; often they are preserved in thin black or green layers of fine-grained sediments, between sandy-silty turbidite beds. In many cases rare nannofossils are found as part of the fine-grained matrix or the fine silt- to clay-size fraction in the sandy, silty turbidites. In the latter case assemblages are always sparse and not always diagnostic. All of the nannofossil assemblages recovered are residual; they show strong evidence of corrosion and dissolution, with only the most resistant species remaining recognizable. Fortunately, many of the key late-Neogene index species, the discoasters, are among the most solution-resistant elements of the assemblage.

The zonal designation used throughout this section is that of Okada and Bukry (1980). Where appropriate, that zonation will be modified to express more clearly the age of a particular level, expanding zones where greater resolution can be achieved than is indicated in the zonation, contracting zones where required by the limitations of the assemblage recovered. The ages assigned to the various depths in the hole are derived principally from the compilation of Berggren et al. (1985). Given the sparseness of the nannofossils and the sometimes inconveniently poor core recovery, these age assignments are not as precise as can be achieved in pelagic sections.

Biostratigraphic Evaluation

One core was recovered in Hole 717A and it yielded late Pleistocene nannofossils. Sections 116-717A-1H-1 through 116-717A-1H-3 contain *Emiliania huxleyi*, which assigns this interval to Zone CN15 and makes it not older than 0.28 m.y. Section 4 yielded no nannofossils, but the core catcher yielded an assemblage without *Emiliania huxleyi* and without *Pseudoemiliania lacunosa*, but with *Gephyrocapsa oceanica*. This combination indicates that this level belongs to nannofossil Zone CN14b. The two cores recovered from Hole 717B also belong to Zone CN14b, although the core catcher of Core 116-717B-2H yielded only a very poor, nondiagnostic assemblage.

Hole 717C was washed to 13.5 m before the first core was taken. The first core from this hole, designated as Core 116-717C-2H, starts within Zone CN14b and this same zone continues into Sample 116-717C-8X-2, 59–61 cm (about 67 mbsf). *Pseudoemiliania lacunosa* occurs consistently from Sample 116-717C-8X, CC, downward and the highest occurrence of this species marks the top of Zone CN14a. The age associated with this datum is 0.47 m.y. Zone CN14a, the *Pseudoemiliania lacunosa* Zone, continues to Core 116-717C-24X-5, 20–22 cm (about 196.2 mbsf). The assemblages down to this level are mostly sparse but typically of late Pleistocene aspect, although contamination by redeposited older–mostly Pliocene–species is common. The assemblage in Section 116-717C-24, CC is dominated overwhelmingly by small *Gephyrocapsa* and lacks *Gephyrocapsa oceanica*. This level is, therefore, assignable to the small *Gephyrocapsa* acme interval and is equivalent to the upper part of Zone CN13b. The top of the small *Gephyrocapsa* acme interval corresponds closely to the top of the Jaramillo magnetic event and has an estimated age of 0.93 m.y. Thus, approximately the upper 197 m of section at this site represents only the younger half of the Pleistocene.

Cores 116-717C-25X and -717C-26X yielded rare to common nannofossils at several levels, the assemblages being chiefly of early Pleistocene aspect although some contain late Pliocene components such as *Discoaster brouweri* and abundant small *Reticulofenestra*. The Pliocene species are judged redeposited and the cores are assigned an early Pleistocene age (Zone CN13). Section 116-717C-26X, CC contains particularly abundant nannofossils, but the assemblage is a mixture of late Miocene, Pliocene, and early Pleistocene components. The age derived from this assemblage is judged unreliable because it is too old relative to several subjacent samples. The top of Zone CN12c is next below in Section 116-717C-27X-5, 100 cm, marked by the highest occurrence of *Discoaster pentaradiatus*. By inference, the Pliocene-Pleistocene boundary is between Sections 116-717C-26X, CC and -717C-27X-5, 100 cm within an unpromising lithology. Next is the top of Zone CN12b in Sample 116-717C-28X-5, 114–116 cm, marked by the highest occurrence of *Discoaster asymmetricus* (which is equivalent to the highest occurrence of *Discoaster surculus*). This is followed by the top of Zone CN12a in Section 116-717C-28X-5, 141 cm, marked by the highest occurrence of *Discoaster variabilis*. The ages associated with the upper limit of each zone are as follows: Zone CN12d—1.9 m.y; Zone CN12c—2.2 m.y; Zone CN12b—2.47 m.y; Zone CN12a—2.9 m.y. This succession of late Pliocene zones should be viewed with a certain amount of caution because it may be based on redeposited or mixed assemblages, some of which are only marginally datable. The very uneven thickness of the late Pliocene zones reinforces the above caution. The late Pliocene continued downward to Section 116-717C-40X, CC although a layer particularly rich in nannofossils and containing both *Sphenolithus abies* and *Reticulofenestra pseudoumbilica* occurs at Section 116-717C-35X, CC. However, this layer is succeded downward by the late Pliocene assemblages and is therefore considered to be redeposited.

Next below is the top of Zone CN11 in Section 116-717C-40X, CC, marked by the highest consistent occurrence of *Sphenolithus abies* and *Reticulofenestra pseudoumbilica*. This corresponds approximately to the midpoint of the Pliocene, or very close to the 3.5-m.y. level. Much of the Pliocene below this level cannot be readily broken down into zones because of the generally less-reliable nature of early Pliocene markers and the even less-reliable record obtained at this site. Zone CN10b is identified in Samples 116-717C-46X, CC, and 116-717C-47X, CC, based on the presence of *Ceratolithus armatus*, a surrogate marker in the absence of other ceratoliths. In any case, the above marks the base of the Pliocene in this section because the very next lower sample, from Sample 116-717C-48X-6, 41-43 cm, contains *Discoaster quinqueramus*, the marker species for the late Miocene Zone CN9b. The precise position of the Miocene/Pliocene boundary within Core 116-717C-48X is uncertain. Zone CN10a, which is thought to be the the youngest identifiable nannozone within the Miocene, was not recognized and must, in any case, be of very short duration.

The next lower useful datum is the occurrence of *Amaurolithus amplificus* in Section 116-717C-52X-3; 76 cm and Sample 116-717C-54X-5, 106–108 cm, which indicates an age not greater than 5.9 m.y. for these levels.

The late Miocene contains few marker species at this site and none is sufficiently consistent in occurrence to be considered totally reliable. One possible useful point may be the occurrence of *Discoaster neohamatus* in Section 116-717C-77X-3, 130 cm, which indicates this level as assignable to Zone CN8b which, in turn, implies an age between 8.2 and 8.4 m.y.

The oldest useful nannofossil date is from the base of the section, in Section 116-717C-91X-2, 20 cm, where a residual but diagnostic assemblage was recovered, which contains *Discoaster hamatus*, *Catinaster coalitus*, and *Discoaster bellus*. These species place the sample within the top of Zone CN7, with an associated age of about 9.5 m.y.

Sediment Accumulation Rate

The ages derived from paleontological analysis—chiefly nannofossils—and the corresponding depths are given in tabular form in Table 3. They are also given on a depth vs. age plot in Figure 7, to yield a sediment accumulation rate curve. Sediment accumulation is greatest for the late Pleistocene, particularly for the interval from 0.47 to 0.93 m.y., when sediment accumulated at the rate of 260 m/m.y. (Not surprisingly, this corresponds to the maximum density of massive turbidites.) The rate for the latest Pleistocene is somewhat lower at approximately 145 m/m.y. In marked contrast is the accumulation rate for the early Pleistocene, which is less than 20 m/m.y. Indeed, there may be a significant hiatus in the early Pleistocene, as no sediments of this age were identified. During the Pliocene, sediment accumulated at an average rate of about 55 m/m.y., although there seems to be considerable variation around that average. During the late Miocene, sediment accumulated at a higher rate also, especially during the latest Miocene (Messinian), with an overall average rate of approximately 100 m/m.y.

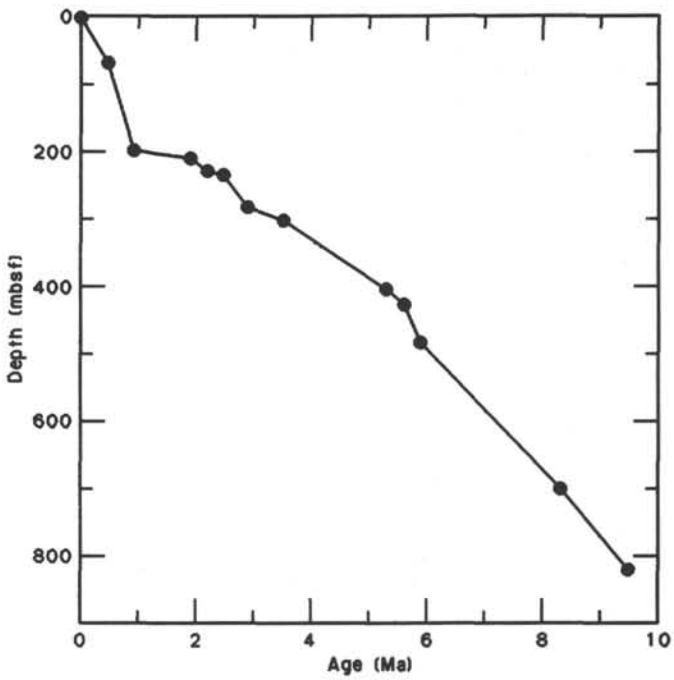

Figure 7. Sediment accumulation rate, Site 717 (not corrected for compaction).

ORGANIC GEOCHEMISTRY

The organic geochemical program at Site 717 consisted of measurements of hydrocarbon gases, organic carbon, and Rock-Eval pyrolysis characteristics on selected samples. In addition, interstitial water and sediment samples were collected for shore-based organic geochemical studies.

Hydrocarbon

Vacutainer Gases

Vacutainers were prepared by using the laboratory freeze dryer to remove contaminants and to establish a vacuum of about 40 in. Hg following the method of Kvenvolden and McDonald (1986). Gases within the core liner were recovered directly by means of a hollow punch equipped with a valve. After the punch penetrated the core liner, gas vented through the valve into a 20-mL vacutainer. The gases were analyzed by gas chromatography (Hach-Carle Gas Chromatograph) and the results are listed on Table 4. Gas pockets were observed only in Cores 116-717C-19X (142 mbsf) and 116-717C-20X (154 mbsf) and were analyzed. The C_1 concentrations are 84.7% and 34.1%, respectively. The presence of those gases can be explained in terms of the sulfate reduction-methane generation model (Claypool and Kaplan, 1974). In this model, the generation of C_1 is a result of the complete removal of sulfate by sulfate-reduction bacteria in the presence of sufficient organic material. At this site, the sulfate concentration decreases quickly to a few millimoles by Core 116-717C-4X. C_2 concentrations show 75 and 3.1 ppm, respectively, in the two samples, but C_3 was not found. Values for the C_1/C_2 ratio of vacutainer samples are high, about 1×10^5. It appears that the gases result from microbiological generation.

Table 3. Selected depths with ages of corresponding nannofossil biohorizons.

Depth (mbsf)	Age (m.y.)
67.5	0.47
198	0.93
205	1.9
224	2.2
233	2.47
282	2.9
321.5	3.5
404	5.3
425	5.6
482	5.9
697	8.3
820.4	9.5

Extracted Gases

Whole pieces of sediment (approx. 3 to 5 cm in length) were sealed in headspace vials and maintained at 70°C for a minimum of 1.5 hr. Volumes (0.25 mL) of headspace gas were then analyzed on the HP Natural Gas Analyser system.

The C_1 content of the sediment ranges between 10 and 20 ppm down to Core 116-717C-4X and increases rapidly below Core 116-717C-5X (38 mbsf) (Fig. 8). The rapid increase in C_1 concentration at Core 116-717C-5X (38 mbsf) correlates inversely with a rapid decrease in sulfate concentration. The C_1 concentration is mostly in the range 2000 to 7000 ppm between depths of 30 and 250 mbsf but then drops to within the range 30 and 2000 ppm from there to Core 116-717C-51X (450 mbsf) except for Core 116-717C-38X (326 mbsf). However, at a depth of 480 mbsf (Core 116-717-54X), the concentration increases abruptly to 5000 ppm. Below Core 116-717C-54X, the C_1 concentration again decreases slowly with depth to the bottom core (825 mbsf) (Table 5 and Fig. 8).

The decrease in C_1 content with depth is sharp above Core 116-717C-49X, but more gradual below Core 116-717-54X. This difference suggests a difference of origin or source of organic materials. However, the consistently low concentrations of C_2 throughout the section at Site 717C does not indicate any change in source.

Table 4. Vacutainer gases, Site 717.

Sample (interval, cm)	Depth (mbsf)	C_1 (%)	C_2 (ppm)	C_1/C_2
717C-19X-1 (103-108)	142	84.7	7.5	1.1×10^6
717C-20X-3 (80-85)	154	34.1	3.1	1.1×10^6

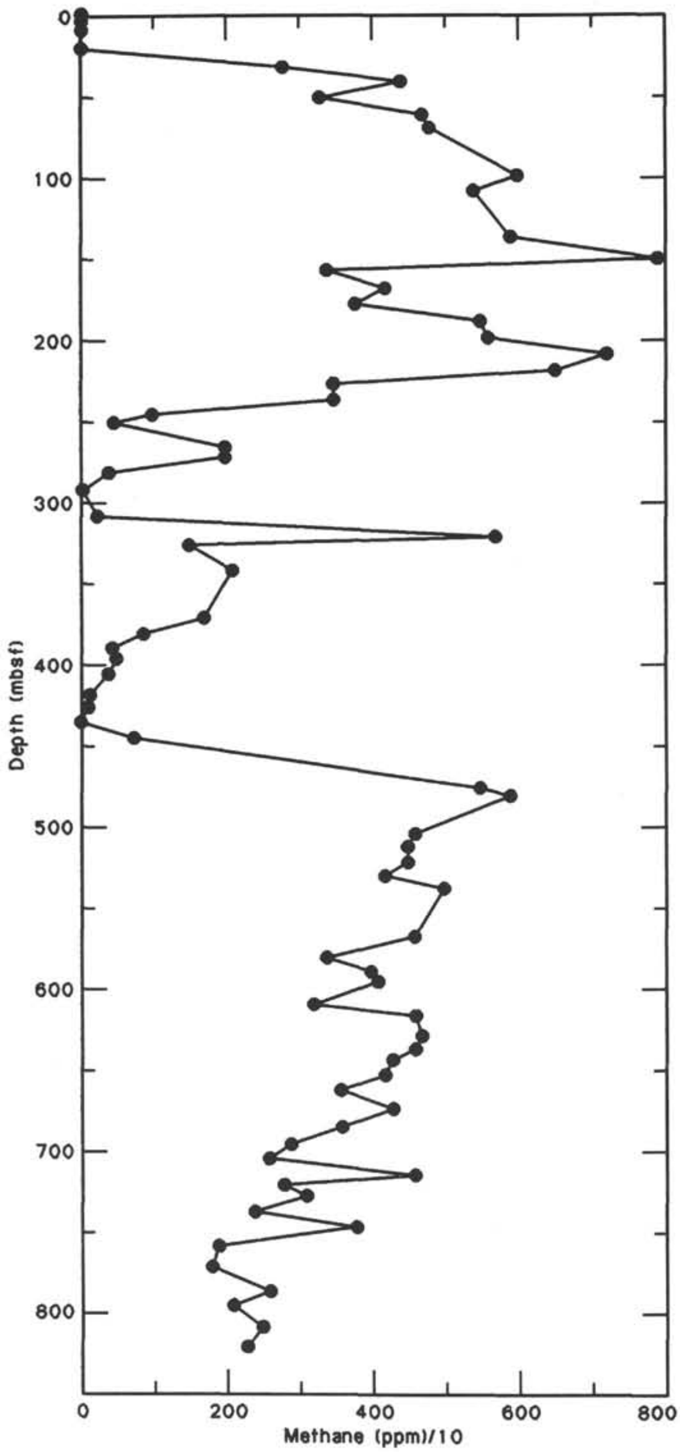

Figure 8. Extracted methane concentrations vs. depth, determined by the headspace procedure at Hole 717C.

Carbon

A portion of each of 73 sediment samples above the depth of 822 mbsf was analyzed for total carbon, carbonate carbon, and organic carbon. The results are given in Table 6 and displayed in Figure 9. These results indicate less than 4.60% carbonate carbon (see "Lithostratigraphy" section, this chapter). Organic carbon values are high (greater than 7% in one sample at a depth of 102.8 mbsf). The large amount of organic material stimulated bacterial activity that generated the vacutainer gases (Table 4). The organic carbon concentration is an average of about 1.0% above a depth of 500 mbsf and less than 0.5% below 500 mbsf. In the lower section there is little variation, indicating a low uniform input of organic carbon in turbidity currents and/or rapid consumption by bacterial action. In the upper section, there appears to be a cyclic alternation, typically between about 0.1% and 2.5% organic carbon. This averages approximately the same weight as that found beneath the high productivity zone in the Arabian Sea (i.e., about 1%). But primary production shows 150-250 mg C/m^3 $\times$ day in the Bay of Bengal, which is less than half that in the Arabian Sea (500 mg C/m^3 $\times$ day) (Degens and Mopper, 1976). Clearly, much of the large volume of organic material is terrestrial and ultimately derived from the Ganges and Brahmaputra rivers.

Rock-Eval

Rock-Eval results are given in Table 7. The Hydrogen Index (HI) and Oxygen Index (OI) values fall in the field for Type III (terrestrial wood) when they are plotted on a van Krevelen-like diagram (Tissot and Welte, 1984) (Fig. 10). These results suggest that all of the carbon is derived from terrestial sources, which would be consistent with an origin from plants growing on the Ganges-Brahmaputra river/delta plain. In the data, the primary productivity in this area was not high because Type II (marine origin) does not exist. T_{max} values range from 380 to 440°C, which indicate that the organic matter is *immature* with respect to petroleum potential.

INORGANIC GEOCHEMISTRY

Methods

Methods employed for interstitial water (IW) studies are those described in Gieskes and Peretsman (1986). When the amount of IW collected was too low to allow regular shipboard analyses, we measured alkalinity on 1 cm^3 rather than 5 cm^3 and pH on the volume of sample left after shipboard analyses. In this case the uncertainty of the pH measurements was about 0.05 pHu. Separate titration analyses were made for Mg, Ca, Cl, SO_4, PO_4, NO_3, NH_4, Si, and total salinity. Other analyses that will be carried out in shore-based laboratory include K, Sr, $^{87}Sr/^{86}Sr$, trace metals, $^{18}O/^{16}O$, and D/H. A check for methane concentrations that should favor hydrate formation and decrease chlorinity was carried out following Blanc et al. (1986).

Results

The results of shipboard measurements of interstitial water composition are given in Table 8, in Figures 11 through 18, and as discussed below.

Chloride (Cl) and Sodium plus Potassium (Na + K)

The concentrations of Cl as well as Na + K show very large variation, ranging over almost 20%. Such scatter in biogenic sediments is not uncommon (Sayles and Manheim, 1975) but has rarely been observed in terrigenous sediments. Possible pollution by the different drill fluids was investigated as a cause,

Table 5. Headspace gases at Site 717.

Core-Section (Interval, cm)	Depth (mbsf)	C_1 (ppm)	C_2 (ppm)	C_1/C_2
Hole 717A				
1H-5 (0-5)	6.0	19		
Hole 717B				
2H-5 (0-5)	10	13		
Hole 717C				
2H-2 (0-5)	15	12		
4X-1 (0-5)	27	9		
5X-1 (115-120)	37.7	2800		
6X-1 (48-53)	48	4400		
7X-1 (145-150)	57	3300	0.3	10000
8X-2 (0-5)	66.5	4700		
10X-1 (145-150)	76	4800	0.5	9600
14X-2 (0-5)	104.5	6000	3.2	1900
15X-2 (0-5)	114	5400	1.4	3800
19X-1 (103-108)	142	5900	1.7	3500
20X-4 (0-5)	156.5	7900	0.4	20000
21X-3 (0-5)	163	3400	0.3	11000
22X-4 (0-5)	174	4200	0.4	11000
23X-4 (0-5)	183.5	3800	0.3	13000
24X-4 (0-5)	193	5500	0.3	18000
25X-5 (0-5)	202.5	5600	1.1	5100
26X-5 (0-5)	213	7200	1.7	4200
27X-5 (0-5)	223	6500	1.1	5900
28X-5 (0-5)	232.5	3500	0.4	8800
29X-5 (0-5)	242	3500		
30X-5 (0-5)	251.5	1000	0.6	1700
31X-2 (0-5)	256.5	470		
32X-5 (0-5)	270.5	2000		
33X-3 (0-5)	277	2000		
34X-3 (0-5)	286.5	400		
35X-4 (0-5)	297.5	30		
37X-2 (0-5)	313.5	240		
38X-4 (0-5)	326	5700	2.0	2900
39X-1 (0-5)	331	1500	0.4	3800
40X-5 (0-5)	346.5	2100	0.3	7000
43X-5 (0-5)	375	1700	0.4	4200
44X-5 (0-5)	384.5	870		

Table 5 (continued).

Core-Section (Interval, cm)	Depth (mbsf)	C_1 (ppm)	C_2 (ppm)	C_1/C_2
45X-5 (0-5)	394	440		
46X-3 (0-5)	400.5	500		
47X-3 (0-5)	410	390		
48X-5 (0-5)	422.5	130		
49X-4 (0-5)	430.5	100	0.5	2000
50X-4 (0-5)	440	—		
51X-4 (0-5)	449.5	730		
54X-5 (0-5)	479.5	5500	3.2	1700
55X-2 (0-5)	484.5	5900	4.3	1500
57X-5 (0-5)	508	4600	1.6	2900
58X-4 (0-5)	516	4500	2.0	2300
59X-4 (0-5)	525.5	4500	1.8	2500
60X-3 (0-5)	533.5	4200	0.4	11000
61X-2 (0-5)	541.5	5000	2.0	2500
64X-3 (0-5)	571.5	4600	1.9	2400
65X-5 (0-5)	584	3400	0.7	4900
66X-4 (0-5)	592	4000	0.8	5000
67X-2 (0-5)	598.5	4100	1.6	2600
68X-5 (0-5)	612.5	3200	1.2	2600
69X-3 (0-5)	619	4600	2.2	2100
70X-5 (0-5)	631.5	4700	1.6	2900
71X-4 (0-5)	639.5	4600	3.2	1400
72X-2 (0-5)	646	4300	1.9	2300
73X-2 (0-5)	655.5	4200	3.0	1400
74X-2 (0-5)	665	3600	1.3	2800
75X-3 (0-5)	676	4300	3.7	1200
76X-4 (0-5)	687	3600	2.9	1200
77X-5 (0-5)	698	2900	1.1	2600
78X-5 (0-5)	707.5	2600	1.4	1800
79X-5 (0-5)	717	4600	2.2	2100
80X-3 (0-5)	723.5	2800	1.4	2000
81X-1 (0-5)	730	3100	0.4	7700
82X-1 (0-5)	739.5	2400	1.2	2000
83X-1 (0-5)	749	3800	2.2	1700
84X-3 (0-5)	761.5	1900	0.8	2400
85X-5 (0-5)	774	1800	2.5	7100
87X-2 (0-5)	788.5	2600	3.7	700
88X-1 (97-102)	797.5	2100	4.9	400
90X-1 (145-150)	810.6	2500	3.7	660
91X-3 (125-130)	825	2300	1.2	1900

but no evidence in its favor was found. Figures 11 and 12 present two different trends of these elements with depth:

1. The low Cl and Na + K values correspond to clay-rich sediment (dashed curve).
2. The high Cl and Na + K values correspond to sand-type sediments (dash-dot curve).

The (Na + K)/Cl ratios were always lower than bottom seawater except for the last sample collected at a depth of 823 m. The interpretation of these trends is not yet clear, although it may reflect early diagenetic changes in different clay minerals.

These results may be attributed to:

1. Low values: expulsion of water from smectite-type minerals resulting from continental weathering, and replacement of Ca by K and Mg in interstitial sheet position;
2. High values: clay diagenesis in sandstone-type sediment. It is accompanied by uptake of water for the hydrolysis and hydration sphere of metals in interstitial sheet position.

Calcium (Ca)

In the upper 250 m, Ca values are lower than in bottom seawater with a small increase between 60 and 100 mbsf superimposed on the general trend (Fig. 13). From 250 to 500 mbsf Ca increases; from 500 to 800 mbsf the value is almost level, with a small step increase near 700–723 mbsf. There is an abrupt increase in the lowest sample (823 mbsf).

The upper part corresponds to the precipitation of calcite and/or high magnesium carbonate. From 250 mbsf downward the exchange of Ca by other cations in clay minerals is the main controlling factor of Ca in IW. The offset of Ca near 60 to 130 mbsf could correspond to dolomite replacement of calcite, which is possible as sulfate has almost been completely reduced at this depth range. This explanation was also suggested by a large decrease of the IW Mg content at the same depth.

Magnesium (Mg)

The general trend of Mg vs. depth was toward lower values (dashed line, Fig. 14). This can be explained by Mg replacing Ca in clay minerals. This behavior of Ca and Mg is one of the main characteristic features found in numerous IW measurements in previous DSDP and ODP legs. However, there was a large scatter of values for Mg. Some of this scatter could be a result of deposition of high Mg carbonates or dolomite (60–130, 510 mbsf).

Alkalinity (Alk.) Calcium Carbonate Saturation

The general trend of Alk. vs. depth was toward lower values (dashed line, Fig. 15). A large scatter occurred in the upper 300 m. Between 70 and 230 mbsf Alk. variations were correlated with those of Mg and hence are opposed to those of Ca. This is a reflection of the IW-carbonate chemistry already mentioned.

This characteristic can be checked with the Ion Activity Product (I.A.P.) of calcium carbonate vs. depth as shown in Figure 16. In this graph no correction for borate content of alkalinity

Table 6. Organic carbon and carbonate carbon, Site 717.

Core section (Interval, cm)	Depth (mbsf)	Inorganic carbon (%)	Organic carbon (%)
Hole 717A			
1H-4 (60-65)	5.1	0.64	0.56
2H-2 (80-82)	6.3	0.41	0.05
Hole 717B			
2H-6 (113-115)	12.7	0.58	0.39
Hole 717C			
2H-2 (113-118)	6.7	0.60	1.81
4X-2 (60-65)	29.1	0.45	1.36
5X-1 (110-113)	37.6	0.53	0.26
6X-1 (113-118)	47.1	0.39	1.07
7X-2 (2-4)	57.0	0.50	0.07
8X-2 (64-69)	67.1	2.77	1.48
14X-2 (19-22)	104.7	0.48	0.62
16X-1 (72-77)	122.7	0.39	0.66
19X-1 (86-89)	141.9	0.73	0.76
20X-2 (89-93)	152.9	0.68	0.58
21X-4 (66-70)	165.2	0.28	2.12
22X-4 (84-89)	174.9	0.27	7.36
23X-6 (60-65)	187.1	0.47	1.59
24X-7 (60-65)	196.6	0.12	2.05
25X-6 (60-64)	206.1	0.14	1.99
26X-7 (10-14)	216.6	0.40	1.73
27X-4 (65-68)	225.2	0.04	0.35
28X-4 (63-67)	231.6	0.14	1.19
29X-4 (62-65)	241.0	0.03	1.66
30X-6 (63-67)	253.5	0.36	2.08
31X-3 (20-24)	258	0.51	1.84
32X-1 (117-121)	267	0.39	0.61
33X-6 (60-66)	282	0.43	0.46
34X-2 (90-94)	286	4.63	1.21
35X-6 (60-64)	306	0.57	1.66
36X-4 (60-64)	316	1.09	0.54
37X-3 (73-76)	318	0.42	0.44
38X-2 (88-90)	324	0.60	0.44
39X-1 (38-41)	331	0.74	0.65
40X-6 (47-50)	348.5	0.32	2.04
42X-6 (104-107)	368	0.31	1.58
43X-4 (0-150)	373.5	0.53	1.71

Table 6 (continued).

Core section (Interval, cm)	Depth (mbsf)	Inorganic carbon (%)	Organic carbon (%)
43X-5 (0-150)	375	0.24	1.93
46X-4 (59-61)	402.5	0.15	1.93
47X-2 (60-62)	409	0.53	1.70
48X-6 (41-46)	424.5	0.53	0.44
49X-4 (63-64)	431	0.67	2.05
50X-6 (26-28)	443	0.82	0.78
51X-4 (41-42)	450	0.75	0.72
52X-2 (134-139)	457.3	1.17	0.30
53X-6 (120-122)	474	3.21	1.39
54X-6 (142-144)	482.5	0.18	0.43
55X-2 (73-75)	485	0.41	2.27
56X-6 (126-129)	501.2	0.59	0.79
59X-6 (139-144)	520.4	1.81	0.14
60X-2 (62-66)	532.6	0.55	0.18
61X-2 (128-132)	540.8	1.27	0.31
63X-2 (50-53)	561	0.69	0.46
64X-2 (38-42)	570.4	3.19	0.64
65X-6 (21-23)	585.7	0.06	0.32
66X-3 (21-23)	591.3	0.72	0.42
67X-2 (120-122)	599.7	1.02	0.35
68X-5 (70-72)	611.2	1.09	0.27
69X-2 (33-36)	617.8	1.25	0.29
70X-6 (70-72)	633.7	0.74	0.33
71X-CC (14-16)	644.2	1.31	0.32
72X-2 (84-86)	646.8	1.15	0.25
73X-2 (61-63)	656	1.29	0.26
75X-4 (65-70)	678	0.84	0.40
76X-6 (46-51)	690.5	0.93	0.32
77X-6 (40-44)	700	4.64	0.85
78X-6 (143-146)	710.5	1.19	0.40
79X-6 (24-26)	718.8	0.94	0.41
80X-3 (105-108)	824.5	1.09	0.36
83X-1 (65-69)	749.7	1.48	0.22
84X-CC (11-13)	767.6	1.17	0.34
85X-5 (123-125)	775.2	1.31	0.46
87X-2 (87-91)	789.4	0.11	0.17
90X-1 (35-39)	809.5	0.89	0.31
91X-3 (38-40)	822	0.53	0.18

was done, so the data are displaced by a factor with respect to the true I.A.P. and hence with respect to the solubility product. One can see that most of the samples collected below 300 mbsf can be considered at equilibrium with calcite.

The last sample shows a large increase of Alk. and I.A.P., which was quite unexpected at 823 mbsf. Upon sampling, a strong odor of polyalkylamine was noted in the same depth range. This could be a result of the extensive fermentation of organic matter, mostly from siliceous-type plankton. The resulting content of organic matter in the corresponding sediment was low (0.2%) as compared with the remainder of the core, and no siliceous tests were observed at this depth. The formation of an indurated sandstone layer, with visible carbonate veins near 790 mbsf, may be related to this large alkalinity increase following degradation of organic matter.

Sulfate (SO_4)

As expected in organic-rich pelagic and terrigenous mud, SO_4 showed a strong decrease in the first 25 m. Below 150 mbsf, the values was scattered around 2 to 3 mmol. This scatter can be partly attributed to oxidation of pyrite during the various sampling operations. Between 50 and 100 mbsf there was a small increase in SO_4 following the offset of Ca. This could be the result of release of residual SO_4 from the surface of calcite upon its transformation into dolomite as already noted.

Punch-in tests for the presence of free hydrogen sulfide were done by inserting a specific electrode in the sediment. The results were always negative. This can be attributed to the formation of iron sulfides (FeS_2, Fe_3S_4) owing to the release of iron from terrigenous clays or oxides and reaction with H_2S/HS. The presence of these sulfides was often noted in the sediment.

Silica (SiO_2)

SiO_2 has moderate concentrations in IW at most depths except near 150–250 mbsf and at the bottom of the core near 823 mbsf. This low level is indicative of the low concentration of biogenic silica. The peak near 200 mbsf corresponded to a layer where radiolarians were preserved because of an iron sulfide coating. Note that the width of the peak is about 200 m. This corresponds to a diffusive path length with a time scale about 1 Ma, which is also the age attributed to this layer. The high in SiO_2 around 200 mbsf may be caused mainly by one source layer rich in decomposing siliceous tests.

There was also a very large increase of SiO_2 at 823 mbsf. This corresponds to the large Alk. and Ca increases. Increased SiO_2 may be attributed to fermentation of siliceous plankton. However, no siliceous test was observed at this depth, casting some doubt on the diagenetic origin for the Ca-Alk.-SiO_2 increases.

Phosphate (PO_4), Ammonia (NH_4), and Nitrate (NO_3)

PO_4 concentrations in IW were significant in the upper 250 m. In the deeper parts, they were low. The peak at 150 mbsf correlated well with Alk. Hence, this zone can effectively be the source of Alk. and PO_4.

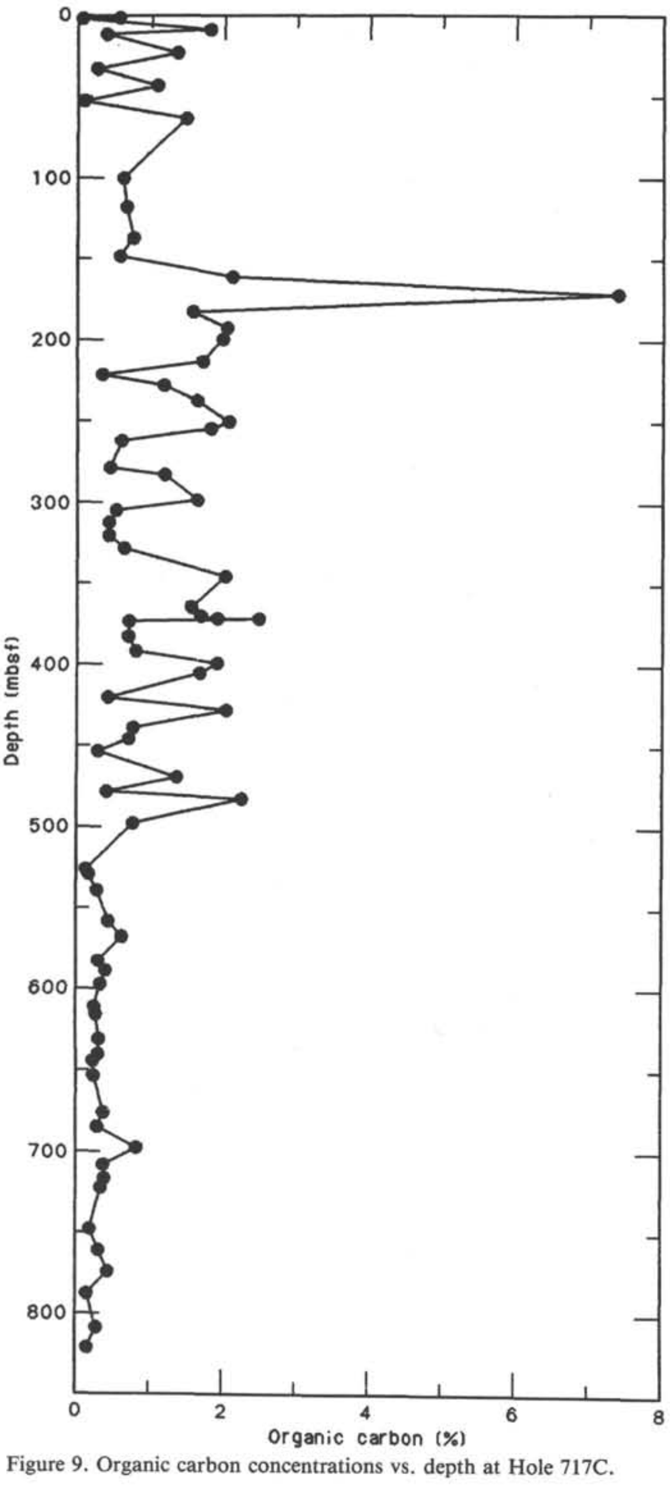

Figure 9. Organic carbon concentrations vs. depth at Hole 717C.

PO_4 and NH_4 concentrations at 823 mbsf were very low, which does not favor the attribution of increases of Ca-Alk.-SiO_2 to organic fermentation, as based on the sole Alk. result.

NH_4 was in the normal range found for the type of sediment encountered at Site 717. The maximum value near 150 mbsf is in good correlation with Alk. and PO_4.

The NO_3 measurements were done only in the upper 350 m. They yielded essentially zero, which they should when sulfate reduction has occurred. The value at 150 mbsf was most probably due to oxidation of NH_4.

Discussion

Most of the results obtained are quite clear but will have to wait for the shore-based laboratory analyses before more extensive discussion of the first conclusions is possible. In the following only the implications of the large anomalies found at 823 mbsf are discussed.

The large anomalies for Alk., SiO_2, and Ca at first suggest they are from extensive diagenesis of organic matter; however, several contrary observations refute this interpretation. First is the lack of siliceous and carbonate tests and the low total organic carbon content, second is the lack of an increase of NH_4 and PO_4 as observed elsewhere in the same core, where extensive organic diagenesis is occuring.

The anomalies of Alk., SiO_2, and Ca could be associated with lateral circulation of a fluid that has acquired these characteristics elsewhere. Vertical circulation from 823 to 790 mbsf must be limited or the vertical gradient would be much smoother than observed. The zone between 823 and 790 mbsf may therefore be the location of, at least, a local barrier for vertical circulation and diffusion.

An interpretation of some of the characteristics of the IW collected at 823 mbsf is that it originates from a place at higher temperature and that it has retained some properties acquired by higher temperature water-rock interactions, i.e., increase in Ca, decrease in Mg, and perhaps increase in Na + K. In this case the SiO_2 anomaly corresponds to near equilibrium with amorphous silica at the temperature/pressure conditions at 823 mbsf and the Alk. anomaly corresponds to more extensive rock alteration at higher temperature. This interpretation implies convective-type fluid circulation in the vicinity of Site 717.

Conclusions

The IW samples collected at Site 717 show the following characteristics:

1. Clear differentiation between clay and sandstone sediments;
2. Clay sediments show a decrease of Cl and Na + K perhaps attributable to expulsion of interstitial water from sheets of smectite-type minerals;
3. Sandstones show an increase of Cl and Na + K attributed to the uptake of water in the interlayer position of clay minerals;
4. Clay minerals from terrestrial sources exchange Ca and Mg, thus leading to a decrease of Mg and an increase of Ca in IW;
5. Calcium carbonate and/or high Mg carbonate should precipitate at different depths, 0–30, 150–250, and 510 mbsf; dolomite may precipitate at 60–130 mbsf;
6. At depths deeper than about 800 mbsf there should be a lateral circulation of IW with limited vertical movement upward above 790 mbsf; this fluid may be part of a convective system.

PALEOMAGNETISM

Major precruise objectives for paleomagnetic work at this site were a magnetostratigraphic study of the late Miocene through Holocene sediments and a careful examination of various geomagnetic phenomena including field excursions and polarity transitions. The expected high sedimentation rate in this region and the anticipated completeness of the sedimentary section promised ideal conditions to study the fine structure of the geomagnetic field over the past 10 Ma. Such studies, however, require oriented and relatively undisturbed core material. As described below, these conditions were not attained at this site and consequently little information regarding the behavior of the geomagnetic field could be obtained. However, interesting magnetic in-

Table 7. Rock-Eval summary, Site 717.

Core Section (interval, cm)	Depth (mbsf)	T_{max}	S_1	S_2	S_3	TOC	HI	OI
Hole 717A								
1H-4 (60-65)	5.1	427	0.10	0.74	2.58	0.56	130	460
2H-2 (113-118)	6.7	427	0.18	0.77	2.58	1.81	41	143
Hole 717B								
2H-6 (113-118)	12.7	440	0.08	0.32	1.21	.39	82	310
Hole 717C								
2H-2 (80-82)	6.3	435	0.28	0.44	2.33	0.05	880	4660
4X-2 (60-65)	29.1	481	0.24	1.04	2.46	1.36	77	181
5X-1 (110-113)	37.6	402	0.04	0.21	0.46	0.26	81	177
6X-1 (113-118)	47.1	386	0.06	0.14	1.51	1.07	13	141
7X-2 (2-4)	57.0	382	0.01	0.07	0.09	0.07	100	129
19X-1 (86-89)	141.9	436	0.08	0.37	3.41	0.76	487	449
20X-2 (89-93)	152.9	435	0.08	0.30	2.18	0.58	52	376
21X-4 (66-70)	165.2	440	0.08	0.32	1.21	2.12	15	55
22X-4 (84-89)	174.9	435	0.28	0.44	2.33	7.36	6	32
23X-6 (60-65)	187.1	481	0.24	1.04	2.46	1.59	176	155
24X-6 (60-65)	196.6	402	0.04	0.21	0.46	2.05	10	22
25X-6 (60-65)	206.1	386	0.06	0.14	1.51	1.99	7	76
26X-7 (10-14)	216.6	382	0.01	0.07	0.19	1.73	4	11
27X-6 (65-68)	225.2	436	0.08	0.37	3.41	0.35	106	974
28X-4 (63-67)	231.6	435	0.08	0.30	2.18	1.19	25	183
29X-4 (62-65)	241	377	0.18	0.96	2.84	0.66	145	430
30X-6 (63-67)	253.5	409	0.12	0.42	5.76	2.08	20	276
31X-3 (20-24)	258	396	0.08	0.28	5.56	1.84	15	302
32X-1 (117-121)	267	374	0.06	0.17	2.32	0.61	27	380
33X-6 (60-66)	282	377	0.03	0.00	2.00	0.46	0	434
34X-2 (90-94)	286	407	0.14	0.82	4.89	1.21	67	404
35X-6 (60-64)	306	406	0.08	0.28	5.20	1.66	16	313
36X-4 (60-64)	316	377	0.07	0.07	2.55	0.54	12	472
37X-3 (73-76)	318	275	0.09	0.07	1.49	0.44	15	338
38X-2 (88-90)	324	242	0.03	0.00	2.64	0.44	0	600
39X-1 (38-41)	331	317	0.03	0.06	2.20	0.65	9	338
40X-6 (47-50)	348.5	397	0.16	0.56	6.54	2.04	27	320
42X-6 (104-107)	368	401	0.08	0.30	4.33	1.58	18	274
43X-4 (0-150)	373.5	402	0.10	0.45	4.73	1.71	26	276
43X-5 (0-150)	375	401	0.13	0.64	4.87	1.93	33	252
46X-4 (59-61)	402.5	415	0.09	0.49	4.52	1.93	25	234
47X-2 (60-62)	409	406	0.07	0.37	5.15	1.7	21	302
49X-4 (63-64)	431	395	0.10	0.34	4.03	2.05	16	196
53X-6 (120-122)	474	409	0.12	0.84	4.67	1.39	60	335
55X-2 (73-75)	485	399	0.10	0.29	5.95	2.27	12	262

Abbreviations: S_1 mg (HC/g rock) = volatile hydrocarbons; S_2 (mg HC/g rock) = kerogen-derived hydrocarbons; S_3 (mg CO_2/g rock) = organic CO_2 from kerogen; TOC = total organic carbon; HI (100 S_2/C_{org}) = Hydrogen Index, OI (100 S_3/C_{org}) = Oxygen Index; T_{max} = temperature (°C) of maximum hydrocarbon generation from kerogen.

tensity and susceptibility results were obtained and will be used in conjunction with rock magnetic studies of these sediments.

Few measurements were made upon individual discrete samples, as the shipboard laboratory was not considered sufficiently free of spurious magnetic fields to avoid problems with viscous remanence to which the sediments seem prone. Consequently, remanence measurements of discrete samples were deferred to shore-based facilities where a controlled, shielded magnetic environment can be used to store samples prior to measurement. Four discrete samples from the second piston core of Hole 717B were subjected to stepwise AF demagnetization through 30 mT and their remanence measured. Two of these samples yielded stable end points in the demagnetization process, and two appeared to acquire an ARM in the Schonstedt demagnetizer. The samples displaying stable end points yielded magnetic inclinations of −12.5 and −21.9 degrees, compatible with the present day field value for the site location.

Remanent Magnetic Intensity

The remanent magnetization of the archive half of each core from Holes 717B and 717C was measured using a pass through, three-component cryogenic magnetometer made by 2-G Enterprises. The magnetometer is fitted with a three-axis alternating field (AF) demagnetizer with a maximum field of 9 mT. Discrete samples were also measured using this system. Demagnetization of discrete samples beyond 9 mT, however, was carried out using a Schonstedt AC Geophysical Specimen Demagnetizer (Model GSD-1). The natural remanent magnetization (NRM) of most core sections was measured using a 5-cm spacing. Each core section was then demagnetized and its remanence remeasured. Initially, several sections were demagnetized over a range of AF field values to monitor the effect of the demagnetization upon the intensity and direction of remanence. Based upon the results of these measurements, all subsequent cores were demagnetized using the maximum field available (i.e., 9 mT). The range of NRM intensities observed was very large, from 0.03 mA/m to greater than 1000 mA/m. Prior to demagnetization, approximately 20% of the 222 sections measured contained sediments too magnetic to be measured with the cryogenic magnetometer. In all but two cases, the AF demagnetization reduced the intensity to the point where the remanence could be measured, although many cores remained strongly magnetic (> 100 mA/m).

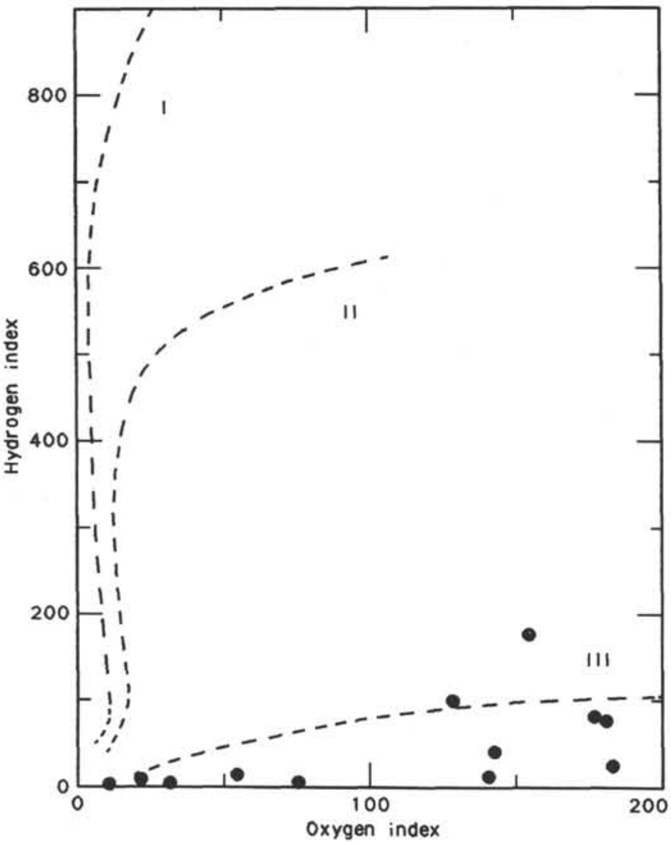

Figure 10. Hydrogen and Oxygen indices (HI and OI) obtained from Rock-Eval pyrolysis of 18 samples from Hole 717C and plotted on a van Krevelen-type diagram.

More often than not, where the sediments were too magnetic to measure, it was the vertical component of the magnetization that exceeded the measurement capability of the magnetometer. Thus a strong axial field, directed vertically upward, appears to have been imparted to the core by either the core barrel or drill pipe. In an attempt to remove this magnetic overprint, core barrels were demagnetized (using the AF setting on the Magnaflux apparatus) until the field measured with a hand-held magnetometer was less than 0.1 mT over most of their lengths. After only one trip down the drill pipe, however, the core barrels were found to be strongly magnetized once again. It seemed that either the drill pipe or the rotating barrel of the XCB produces a strong vertical magnetic field through which the core material must pass on its way to the surface. This overprint was substantially, but not completely, removed by subjecting the core to alternating fields of 9 mT. Figure 19 shows a comparison of the intensity of magnetization of Core 116-717C-29X for NRM, 5- and 9-mT demagnetization measurements. The strongly magnetized portion of the core underwent a dramatic reduction in intensity during demagnetization suggesting that the overprint in this portion was carried mostly by low-coercivity grains. The more weakly magnetized portion, on the other hand, appeared little changed by exposure to the 9-mT alternating field. When these changes in intensity were compared with the associated changes in magnetic inclination (Fig. 20), it is clear that a nearly vertical field component was removed by the demagnetization process. The overprint, however, was not completely removed by the 9-mT AF treatment, and inclinations were still biased towards higher than expected negative values.

Figure 21 shows the variation in magnetic intensity with depth of Hole 717C core material after AF demagnetization with a 9-mT field. Although there was a large scatter in the values, there were a number of significant peaks that clustered into zones. These zones were observed at depths of 45–70, 100–120, 280–320, 580–630, and 760–820 mbsf and presumably reflect either greater concentrations of magnetic grains in these layers or, alternatively, a change in the magnetic mineralogy at these depths. The zones correspond approximately with concentrations of sand and silt layers although not all such layers were associated with large remanent intensities. There are several depth intervals where the remanent intensity was significantly lower, e.g., 180–200 and 480–540 mbsf. In the upper part of the hole many of these low values appeared to correspond with the greenish biogenic turbidites seen in Unit III (see "Lithostratigraphy" section, this chapter). In the lower part of the hole, the low values were more closely related to the gray muds and pelagic clays which occur in Subunit IVd. The corresponding lithology in Unit III, however, was associated with both high and low values and, consequently, a more detailed study of the relationship between the remanent magnetization and lithologic type is required before the any meaningful correlations can be developed. The correlation of the remanent intensity with the susceptibilty depth profile is discussed below.

Magnetostratigraphy

Site 717 is located very near to the Equator and, consequently, there is no appreciable change in magnetic inclination associated with a reversal of the geomagnetic field. Reversals must be identified, therefore, by a 180-degree change in declination. Consequently, to identify the magnetic reversal pattern of the sediments, it is necessary to either azimuthally orient the core or have long sections in which there is little or no rotation of core material. In this hole, piston coring was abandoned after only 13.5 m and the remainder of the hole cored with the XCB, which rotates as it cores. The magnetic inclinations and declinations obtained from the limited piston core material were relatively uniform yielding inclinations of about −10 to −20 degrees. With the XCB it is not possible to obtain oriented cores with which to determine reliable declinations and as a consequence very little magnetostratigraphic information is available for this site. The almost random pattern of magnetic declinations obtained from the XCB core material may be attributed to the coring process, although in the upper part of the section there is little visual evidence of the biscuiting that becomes ubiquitous below approximately 350 mbsf. The lower 450 m of the core was strongly disturbed by drilling, and many of the biscuited pieces are tilted as well as presumably rotated in the core barrel, resulting in the inclination data also being unreliable.

Predicted magnetic inclinations are close to zero for this site but observed values differed appreciably from this (Fig. 20). The measurements were substantially biased, especially NRM measurements, toward more negative values with some exceeding −70 degrees. While this bias was partially removed during demagnetization, some of it certainly remained in the paleomagnetic data, so many measured inclinations are suspect. In spite of this, an attempt was made to characterize the magnetic inclinations observed after AF demagnetization by looking at the predominance of polarity within individual sections of the core. The inclination data showed three major zones: (a) 0–150 mbsf, in which the values were almost entirely negative (i.e., normal polarity); (b) 220–400 mbsf, which was characterized by many reverse polarity zones; and (c) 500–825 mbsf, which was nearly all normal polarity.

Magnetic Susceptibility

Measurements of volume susceptibility, k, were made on whole, unsplit 1.5-m sections of core from Holes 717B and 717C.

Table 8. Interstitial water geochemical data, Site 717.

				Interval (cm)		Method:		T	T	R	T	T	T	I	S	S	S	S			
Hole	Core	Type	Sect.	Top	Bot	Depth (mbsf)	Water (mL)	pH	Alkalinity mmol/L	Salinity g/kg	Mg mmol/L	Ca mmol/L	Cl mmol/L	SO_4 mmol/L	PO_4 µmol/L	NO_3 µmol/L	NH_4 µmol/L	Si µmol/L	Na + K mmol/L	$\frac{Na + K}{Cl}$	I.A.P. $Ca^{2+}(Alk.)(H_3O^+)$
A	1	H	4	145	150	4.6	60	7.41	9.52	34.0	49.08	10.25	557	21.7	20.1	0.0	640	505	485	0.871	281
C	5	X	1	145	150	37.9	17	8.35	14.50	33.2	41.68	6.00	560	0.6	19.3	0.9	2100	215	480	0.857	2181
C	8	X	1	140	150	66.4	64	7.60	8.69	33.8	40.18	6.53	560	2.9	20.4	0.0	2300	330	481	0.859	253
C	14	X	1	140	150	104.4	75	7.48	7.38	33.3	40.38	6.80	558	4.3	16.6	0.0	2900	340	480	0.860	170
C	20	X	3	140	150	154.9	12	8.40	16.31	32.5	44.17	4.05	551	1.4	40.1	7.5	2900	410	474	0.860	1860
C	23	X	3	140	150	183.4	14	8.25	15.00	33.1	45.21	5.15	552	2.9	11.1	0.0	1500	465	472	0.855	1540
C	26	X	4	140	150	213.4	20	—	11.70	32.0	40.72	6.75	553	1.4	9.8	0.0	1800	645	472	0.854	—
C	29	X	4	140	150	241.9	30	—	8.90	31.7	36.72	7.34	556	2.0	6.2	0.0	1800	575	481	0.865	—
C	32	X	4	140	150	270.4	9	8.15	5.45	31.7	39.62	9.49	532	4.3	—	0.2	1600	255	448	0.842	818
C	35	X	3	140	150	297.3	16	8.05	5.07	32.2	34.81	10.38	545	2.9	2.46	0.2	1900	305	465	0.853	661
C	38	X	3	140	150	325.8	71	7.88	5.09	32.4	33.09	12.18	544	4.3	3.12	0.0	1140	203	467	0.858	527
C	42	X	4	140	150	365.3	10	8.10	3.90	29.8	33.27	14.27	521	1.4	4.2	0.0	850	260	435	0.835	785
C	45	X	4	140	150	393.9	7	8.15	3.40	31.9	32.88	15.26	542	7.2	6.5	2.7	1170	253	403	0.854	821
C	48	X	4	140	150	422.4	7	8.00	3.45	31.3	33.25	16.23	528	3.7	3.4		820	215	440	0.833	627
C	51	X	3	140	150	449.4	12	8.00	2.80	31.2	30.87	16.71	529	4.1	4.4		860	195	445	0.841	524
C	54	X	4	140	150	479.4	8	8.05	3.24	30.0	29.35	17.17	505	1.5	2.9		1510	160	418	0.828	699
C	57	X	4	140	150	507.9	61	8.07	2.55	32.1	26.49	16.03	552	3.0	0.63		1800	132	475	0.861	538
C	60	X	2	140	150	533.4	6	7.95	2.90	27.2	32.34	17.77	508	3.7	1.7		1290	157	418	0.823	647
C	64	X	2	130	140	571.4	20	7.95	3.23	32.3	30.02	17.09	559	6.1	2.8		1210	222	480	0.859	551
C	67	X	1	140	150	598.4	36	7.95	4.74	32.3	28.53	17.00	563	5.3	4.6		610	200	487	0.865	804
C	70	X	4	130	140	631.4	44	8.07	1.407	32.7	25.67	16.57	554	2.8	2.1		1020	160	476	0.860	307
C	74	X	1	140	150	664.9	48	7.95	2.55	33.0	20.95	17.13	568	3.7	2.0		750	188	491	0.865	436
C	77	X	4	130	140	697.8	3	8.05	—	27.2	22.71	17.28	472	2.5	—		—	100	>397	>0.840	—
C	80	X	2	140	150	723.4	20	8.05	2.92	32.4	25.30	18.84	509	3.4	2.5		510	217	490	0.862	691
C	84	X	2	140	150	761.4	30	8.10	1.86	32.8	21.22	18.34	568	2.3	2.0		410	215	494	0.869	481
C	87	X	1	140	150	788.4	25	7.90	3.00	33.7	20.95	18.85	570	2.3	2.2		580	195	498	0.874	504
C	91	X	3	140	150	823.1	27	7.45	16.81	33.9	18.66	22.46	557	3.2	2.1		650	1085	498	0.894	1192

T = Hand Titration; R = Refractometer; I = Ion Chromotography; S = Spectrophotometer.

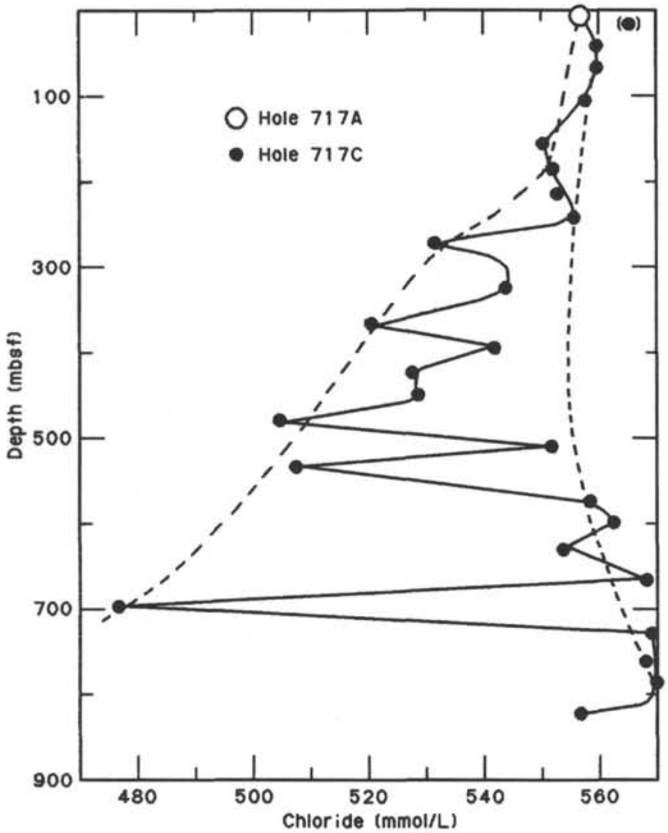

Figure 11. Cl vs. depth at Site 717. Dashed curves: see text.

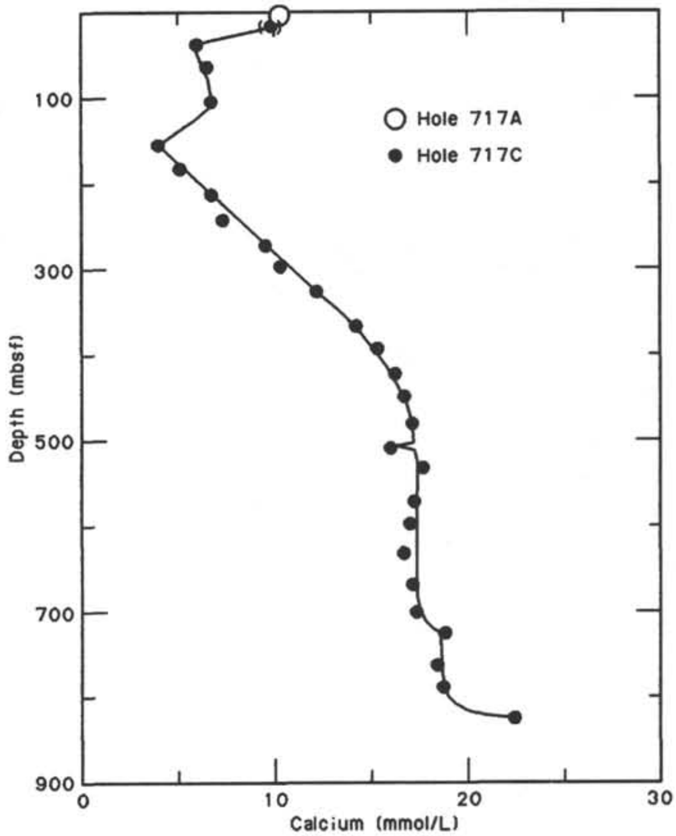

Figure 13. Ca vs. depth at Site 717.

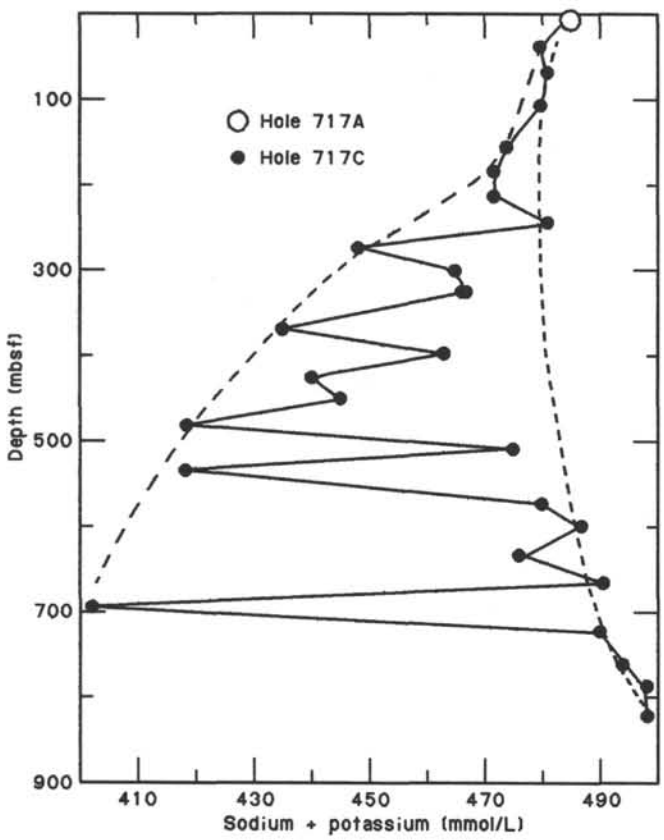

Figure 12. Na + K vs. depth at Site 717. Dashed curves: see text.

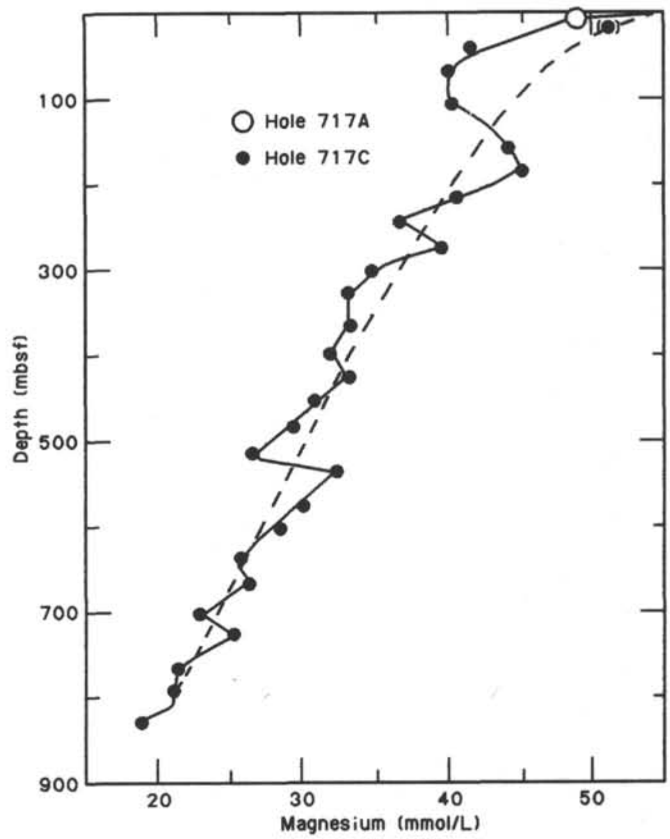

Figure 14. Mg vs. depth at Site 717.

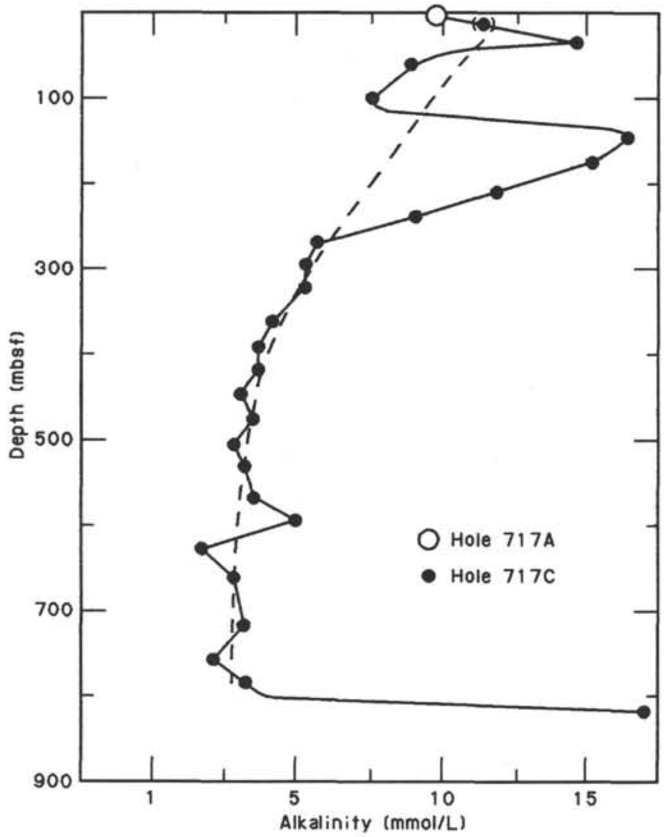

Figure 15. Alkalinity vs. depth at Site 717.

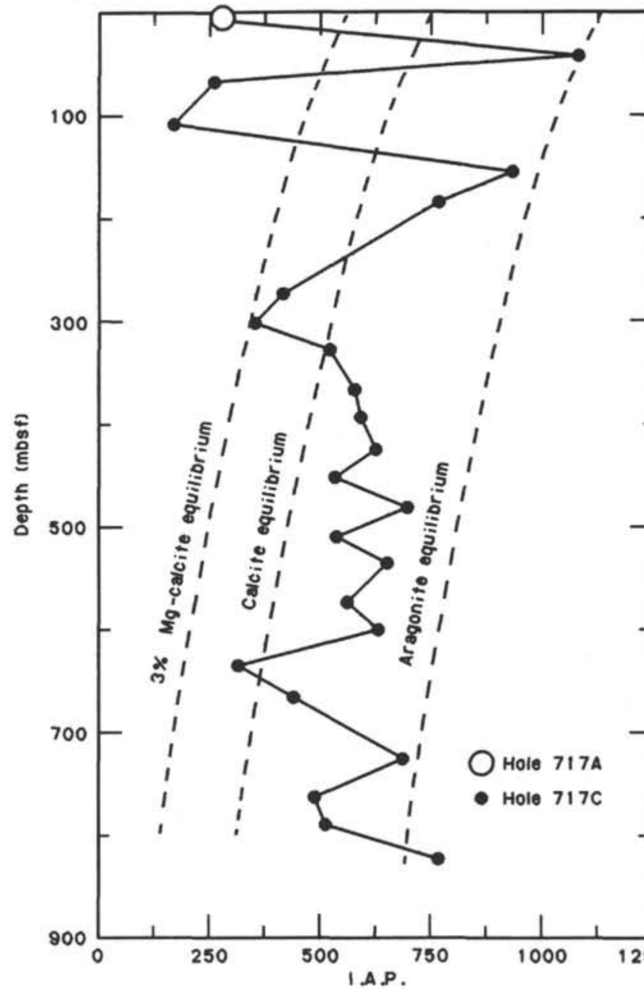

Figure 16. I.A.P. of calcium carbonate vs. depth. The calcite equilibrium line as well as aragonite and 3% Mg calcite has been corrected for temperature and pressure of the samples.

In all, 8,696 susceptibility measurements were made on Site 717 cores. Only 183 of these are from Hole 717B, specifically Core 116-717C-2H. The remainder were obtained from Cores 116-717C-2H to 116-717C-91X. However, as the two holes were situated no more than a few tens of meters apart and were drilled so that the bottom of Hole 717B and the top of the first-recovered core of Hole 717C are coincident, the results from both holes are combined in the following analysis and discussion.

Site 717 cores were strongly magnetic in comparison with most deep-sea sediments. Although the magnetic susceptibility values range from 5 to 897 cgs, the majority of the measurements were between 20 and 80 cgs. However, the susceptibility vs. depth record (Fig. 22) was punctuated with numerous high-amplitude spikes.

On closer examination, the susceptibility record in Figure 22 is not as erratic as it appears at first glance. Susceptibility peaks were almost always correlatable with turbidites. In particular, the highest spikes were measured from dark-gray mud turbidites. Additionally, many silt turbidites gave rise to moderate susceptibility peaks. However, neither relationship displayed a simple one-to-one correspondence. Some dark-gray mud turbidites yielded only small susceptibility peaks, and a few gave none at all. Evidently, the factors that controlled the color and type of sediment do not completely regulate the magnetic minerals, yet there was clearly a close relationship.

A detailed examination also revealed that the susceptibility peaks can be divided into five categories based on shape. The most common morphology was symmetric, with the highest susceptibility values recorded near the center and approximately equal lengths of rising and falling values on either side (Fig. 23). These spikes varied in width from about 10 to 15 cm (the lower limit of resolution with the 5-cm measurement spacing) to 1-2 m. About 40% of the observed peaks could be placed in this category. Figure 23 shows an example of the correlation between these spikes and dark-gray mud turbidites.

The next most common type of peak, comprising about 24% of those observed, was asymmetric with a slow rise in susceptibility with depth followed by an abrupt fall. Two examples from Core 116-717C-48X, which also displayed a good correlation with gray mud turbidites, are shown in Figure 24. The susceptibility values began to rise at the tops of several turbidites and reached large values at their bases. Being relatively heavy, the magnetic minerals apparently settled preferentially to the bottoms of these density-stratified layers. Graded behavior, such as this, was demonstrated by turbidites with widths from about 10-15 cm to 2-3 m. Although not exclusively limited to any particular lithology, susceptibility peaks of this type appeared most commonly in the units characterized by gray mud turbidites.

Other types of susceptibility peaks appeared in lesser numbers. About 14% were flat-topped or multipeaked. These featured a rise in the susceptibility to a higher, nearly constant level or a series of smaller peaks, with a subsequent return to lower values. Another 7% displayed twin peaks, at the top and bottom of the turbidite layer, often with higher than usual values in between. A few susceptibility peaks, about 4% of the those observed, appeared graded, but in the reverse sense. The highest values occurred abruptly at the top of the layer and decreased slowly with depth. These peaks were usually small in amplitude and width and often appeared multipeaked. Approximately 11%

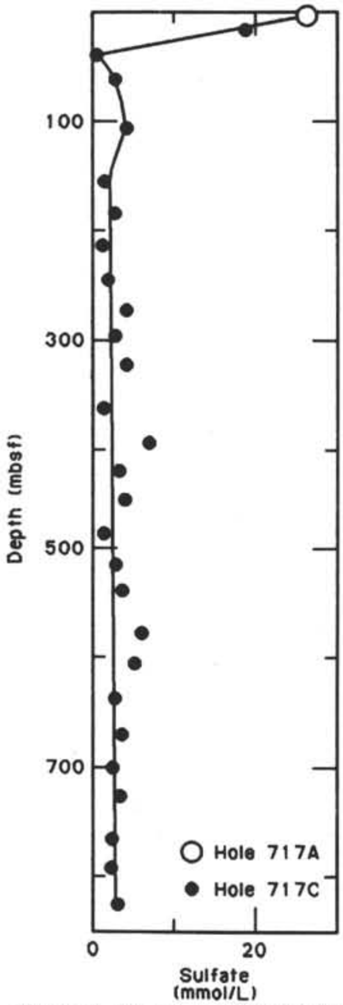

Figure 17. SO_4 vs. depth at Site 717.

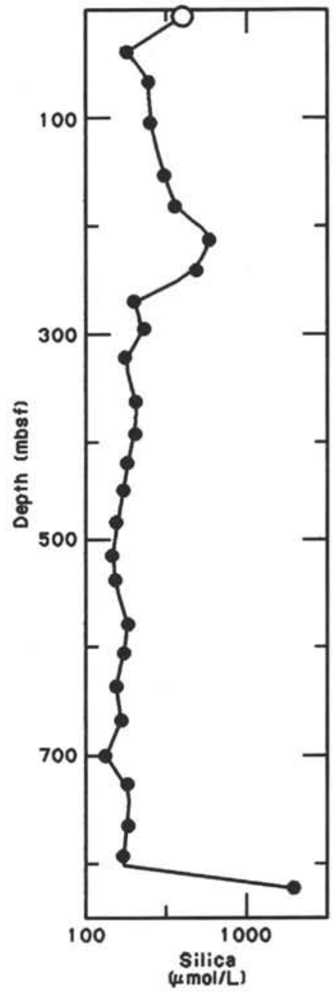

Figure 18. SiO_2 vs. depth at Site 717.

of the peaks could not be fitted into any of these categories, usually because they occurred at the top or bottom of a core or in an interval that was incompletely recovered. Interestingly, a few peaks combined two or more of these characteristics. For instance, a number of layers were noted in which there was a slow rise in susceptibility over several meters depth, similar to the graded behavior, but on top of the rise several thinner, symmetrical peaks occurred. Perhaps this phenomenon was a result of a graded layer consisting of a series of smaller, related turbidites.

It is not clear what minerals gave the sediments from Site 717 their strong magnetism. Detailed shore-based magnetic property studies are required to reveal their identities. However, two properties were evident from the shipboard analysis. First, the high-amplitude susceptibility peaks were correlated with strong remanent magnetization. Apparently, the magnetic susceptibility is carried mainly by a magnetic mineral that is ferromagnetic, eliminating from consideration some minerals, such as pyrite, which were found in Site 717 cores but are paramagnetic. As seen in Figure 24, the correlation between the remanent magnetic intensity and susceptibility can be quite close. Indeed, it might have been better were it not for the drilling disturbance of the core material, which tended to make the intensity values more erratic. Additionally, this relationship was evident on a larger scale as seen by comparison of Figure 22 with Figure 21 in the preceeding section. Second, the carrier of the remanent magnetism in many cases displayed a *soft* unstable behavior. It acquires a strong overprint from exposure to the magnetic field of the drill string. Moreover, this overprint was largely removed with relatively weak alternating magnetic fields. This fact indicated that the carrier of the magnetic remanence has a low coercivity.

The magnetic susceptibility record also contained some interesting features on a broad scale as well. In general, the units of silty turbidites gave rise to the most variable values with many small spikes (Fig. 25). These units apparently consist of many turbidites, with almost every one contributing a susceptibility spike. In the units characterized by mud turbidites, there were often layers of pelagic sediment and light, structureless mud between dark-gray turbidites. The pelagic sediments and light mud usually yielded relatively constant low susceptibility values broken by large spikes resulting from the dark-gray mud turbidites. Additionally, there was a variation with depth of the size of the spikes in Hole 717C that was not clearly related to the type of sediment. These variations were seen as *pulses* of high values at certain depths within the hole (Fig. 22). These pulses were a result of susceptibility peaks with higher amplitudes but not necessarily greater frequency. Prominent pulses were noted between approximately 250–310, 400–480, and 580–620 mbsf. Comparing these pulses to the lithologic units in Hole 717C (see "Lithostratigraphy" section) they were seen to cross the unit boundaries. Evidently these pulses were controlled by

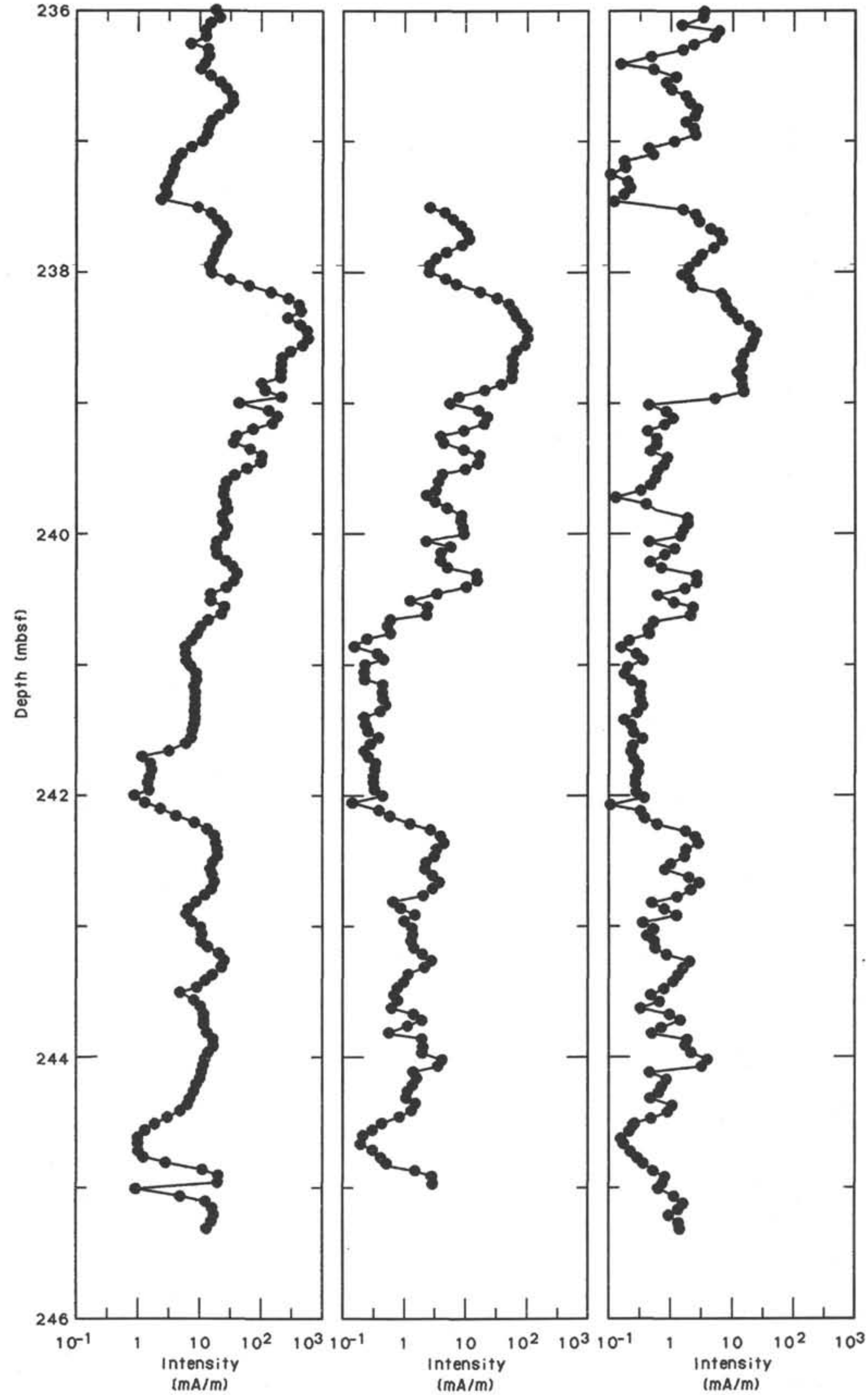

Figure 19. Remanent magnetic intensities vs. depth for Core 116-717C-29X for NRM, 5-, and 9-mT demagnetization measurements.

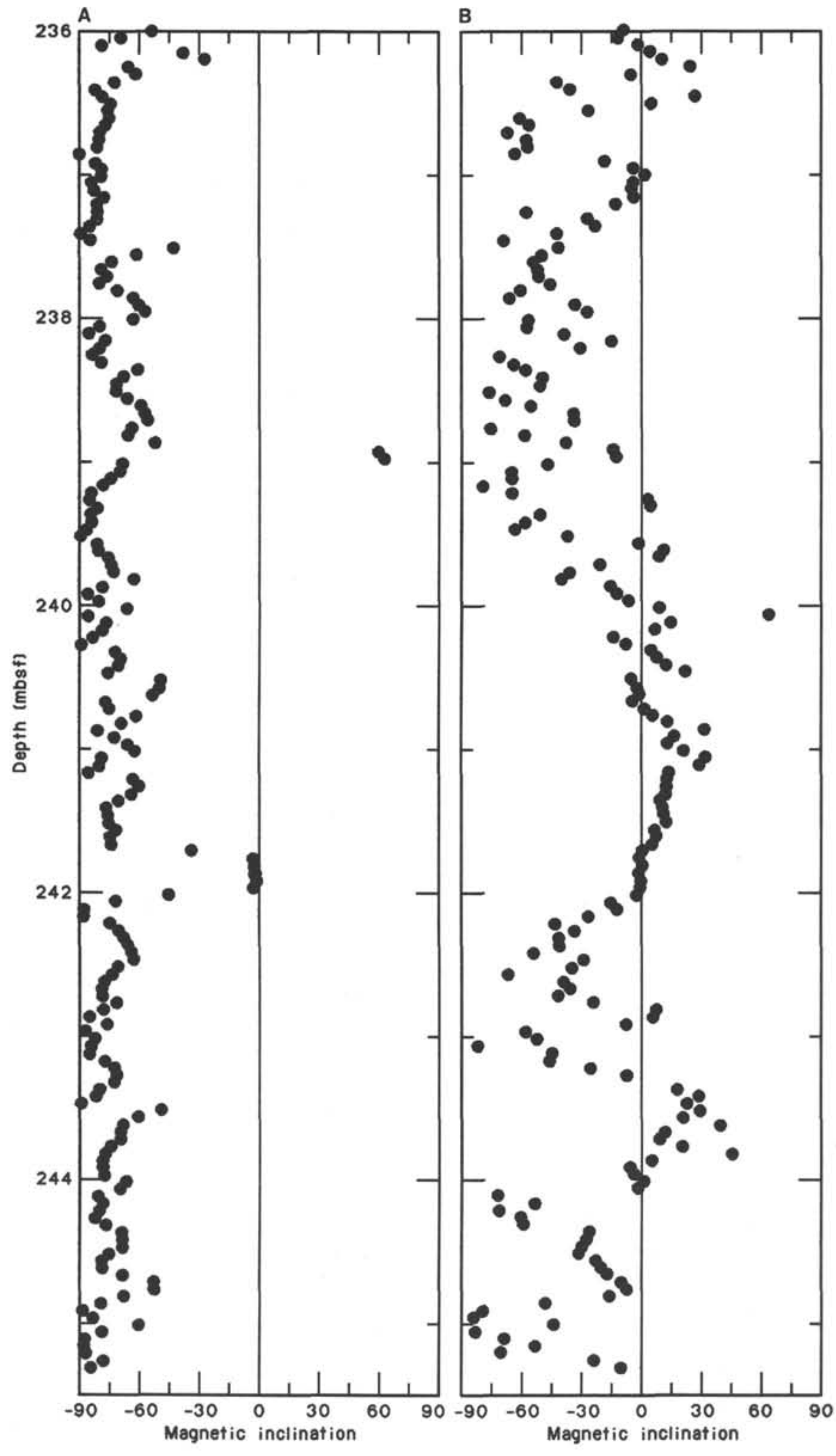

Figure 20. Magnetic inclinations vs. depth for Core 116-717C-29X. (A) NRM, and (B) 9-mT AF demagnetization measurements. Large negative inclination values of NRM are believed caused by overprint from drill pipe.

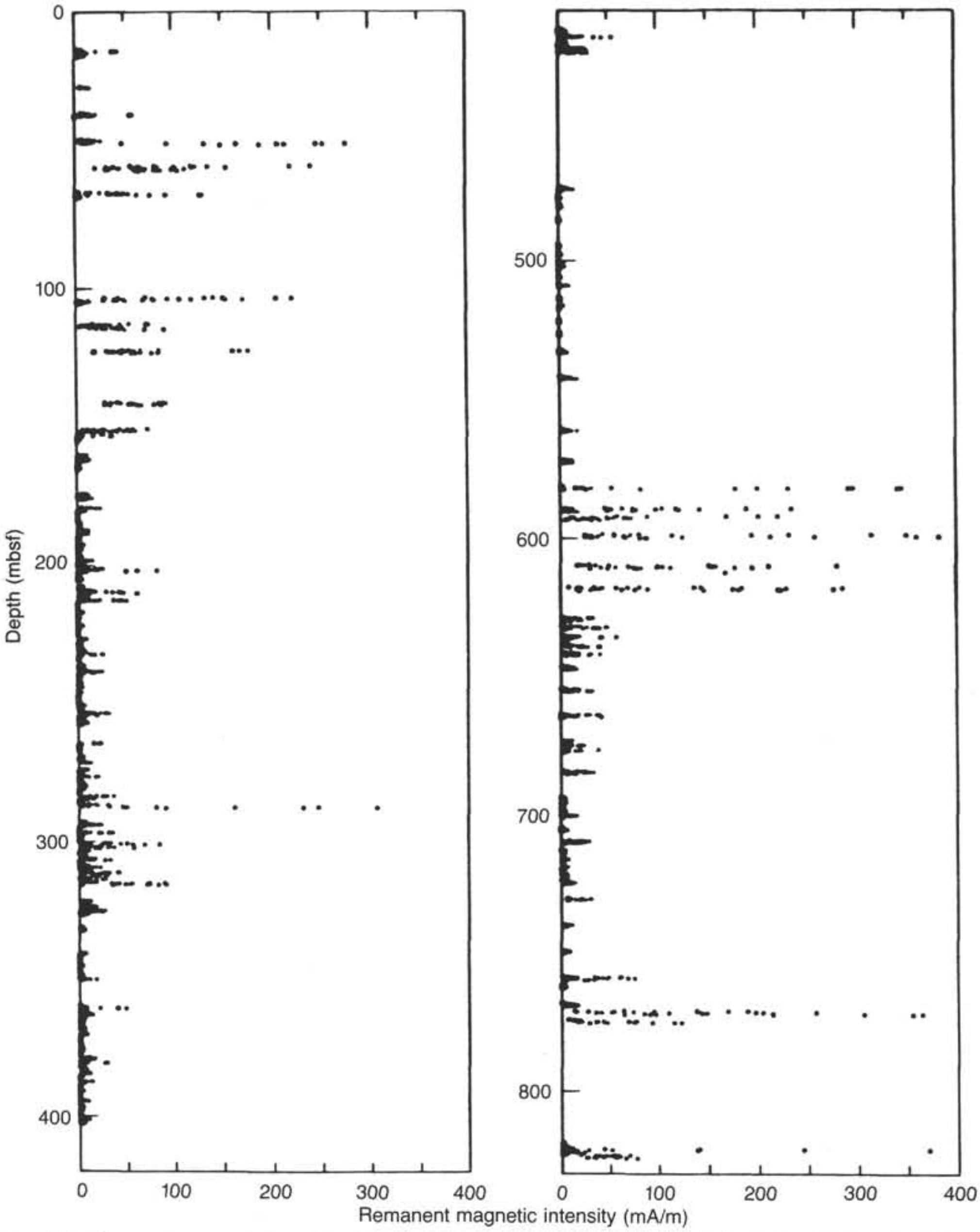

Figure 21. Remanent magnetic intensity after 9-mT AF demagnetization vs. depth for Holes 717B and 717C. Several values exceeding 400 mA/m are not shown.

some process other than the sedimentation regime. Two other possible pulses occurred at the top and bottom of the hole, but these were less certain because of poor core recovery.

PHYSICAL PROPERTIES

Introduction

Cores 116-717A-1H, -717B-1H, -717B-2H, and -717C-2H were obtained by the Advanced Piston Core (APC). Cores 116-717C-2X to -717C-91X were recovered with the Extended Core Barrel (XCB). All cores were used for shipboard analysis of physical properties.

Physical properties measured routinely on all cores recovered at Site 717 include GRAPE density and thermal conductivity from full-round core sections, vane-shear strength, compressional wave velocity, and index properties from split sections (the methods are described in detail in the Explanatory Notes). Results of physical properties measurements at Site 717 are summarized in Tables 9 to 13.

Index Properties

Index properties include wet-bulk density, water content, porosity, and grain density. The measurements were made mainly on fine-grained deposits, with the following results.

Wet-bulk density (Fig. 26A) increased rapidly from 1.5 g/cm^3 at the seafloor to about 1.75 g/cm^3 at 70 mbsf. Below this depth the wet-bulk density increased linearly to about 2.1 g/cm^3 at 810 mbsf. The silt samples had a wet-bulk density of 2.0–2.1 g/cm^3.

The water content (related to wet weight; Fig. 26B) of the clays, silty clays, and claystones exhibited a large variation (15–

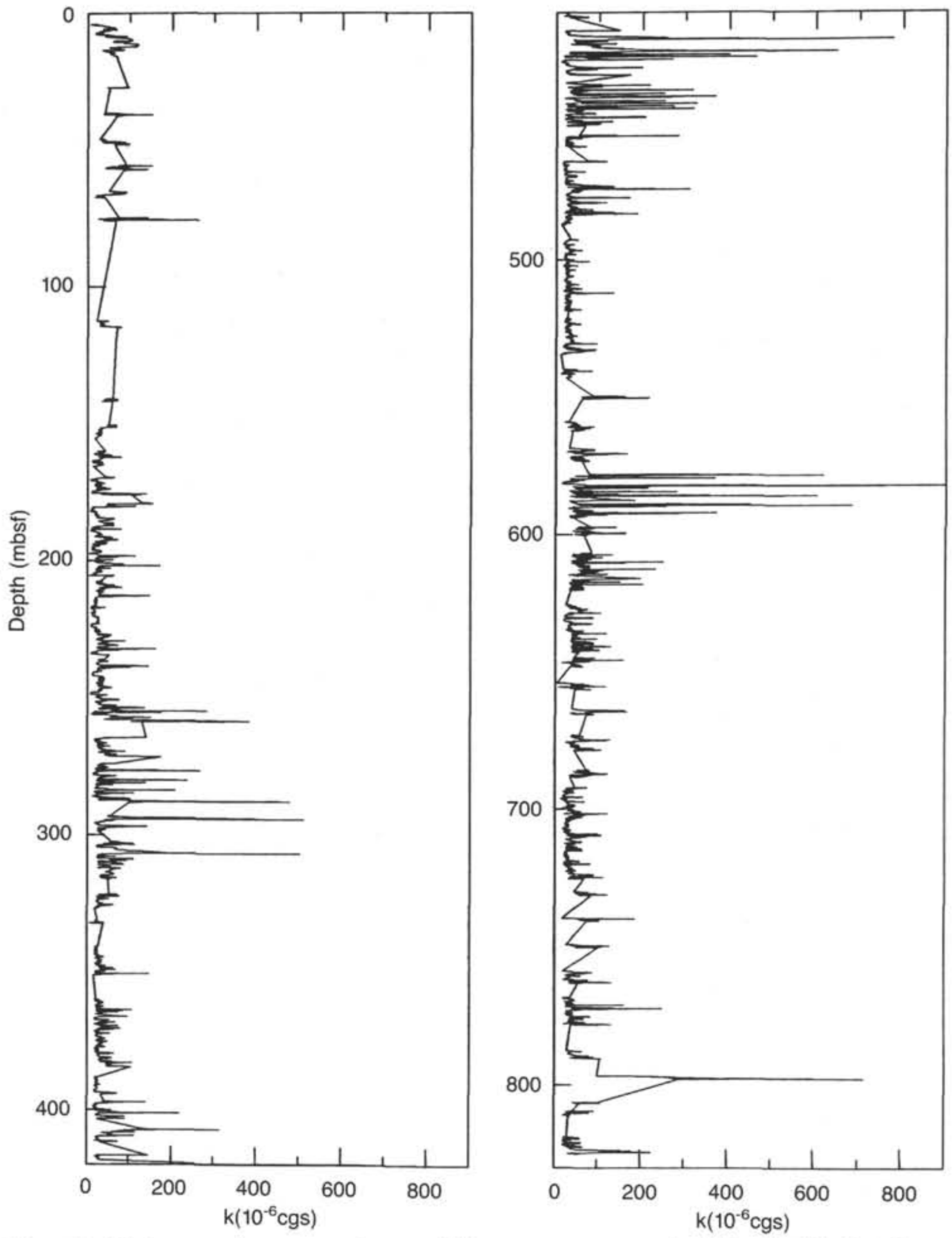

Figure 22. Whole core volume magnetic susceptibility measurements vs. depth for Site 717. Data from both Holes 717B and 717C are included. Susceptibility, k, is given on the abcissa in 10^{-6} cgs units. Depth is shown vertically in meters below the seafloor. In the box on the left are plotted measurements of cores recovered from 0 to 420 mbsf; on the right, values from cores between 410 and 830 mbsf.

60%) over the entire drilled interval. Above 100 mbsf the water content of fine-grained deposits ranged between 30 and 60%. Below 100 mbsf the water content averaged 25–35%, which is very close to the water content of sands.

Porosity (Fig. 26C) decreased downhole from a high of 70–75% for fine-grained sediments at the seafloor to about 55% at 100 mbsf. Below that depth, the decrease of porosity vs. depth was nearly linear, reaching a value of 35% at 810 mbsf. The scattering of data around the trend line was attributed to (a) variations in sediment composition, (b) drilling disturbances, and (c) expanding gas. Drilling disturbance and expanding gas lead to an increase in porosity, water content, and wet-bulk density, whereas the sediment composition can cause a decrease, for instance when organic matter is decomposed.

Grain density (Fig. 26D) varied within the range of 2.65 and 2.85 g/cm^3, values above and below these limits are subject to determination errors.

Compressional Wave Velocity

Sonic velocity measurements range from 1.55 km/s at the mud line to about 1.9 to 2.0 km/s at the bottom of Hole 717C. A quite regular increasing trend is shown (Table 11, Fig. 27) with the exception of one high sonic velocity (4.98 km/s) measured on a cemented sandstone at 790.3 mbsf. The samples taken below 400–500 mbsf were highly affected by drilling disturbances: values on the same core and same lithology usually ranged from 1.6 km/s in Section 1 to about 1.9 to 2.0 km/s in Sections 6 and/or Core Catchers. However, a systematic anisot-

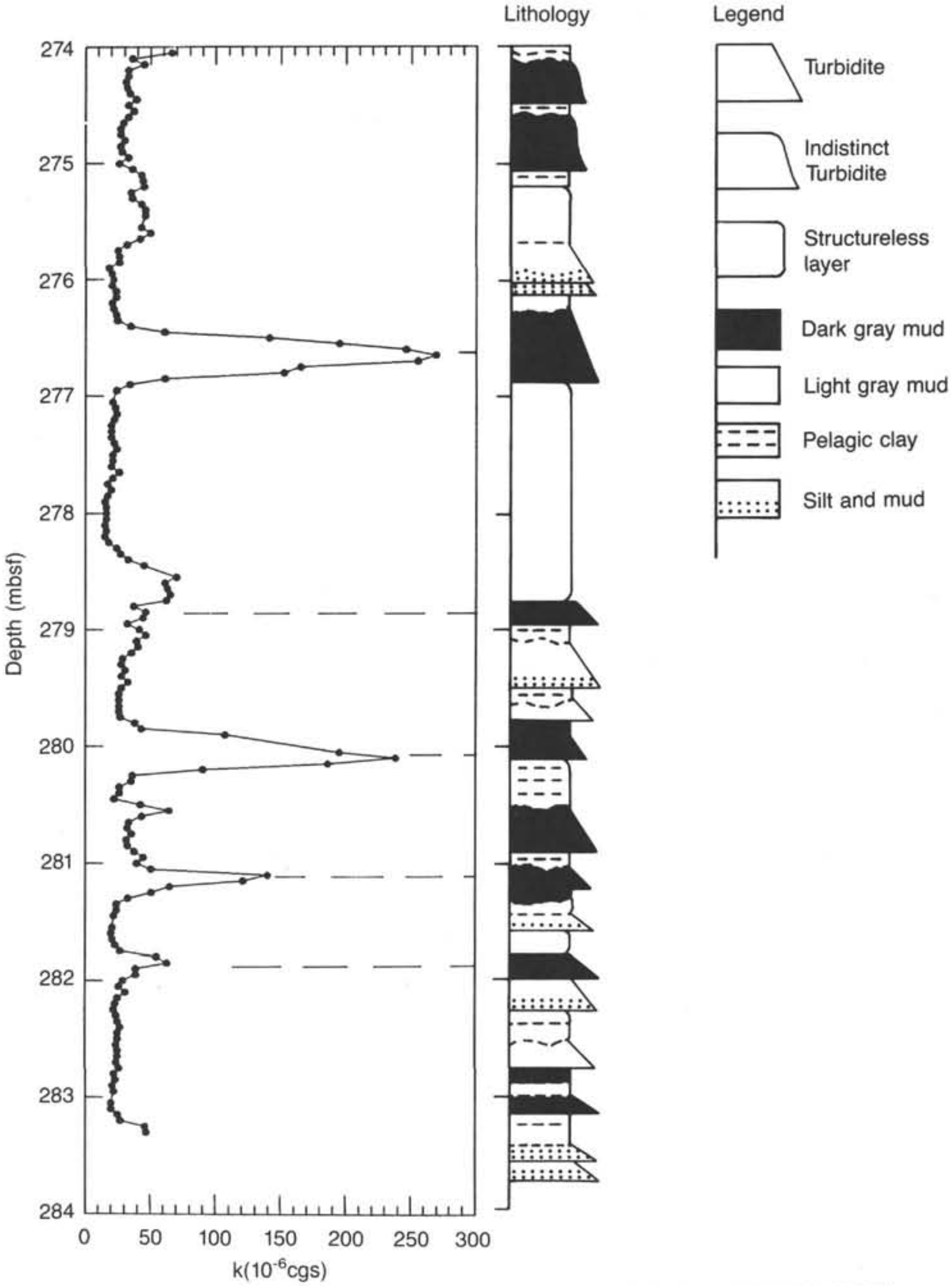

Figure 23. Susceptibility (left) and lithostratigraphy (right) vs. depth for Core 116-717C-33X. These susceptibility peaks are typical of those that display a symmetric shape and are correlated with dark-gray mud turbidites. Dashed lines show correlation between turbidites and susceptibility peaks. Plot conventions as in Figure 22.

ropy (up to 8–10%) has been observed on relatively well-consolidated samples, the horizontal velocities being always higher than the vertical velocities.

Thermal Conductivity

Thermal conductivities were used for the evaluation of the heat flow in connection with temperature measurements in Hole 717C (Table 12, Fig. 28). The thermal conductivity measurements were routinely performed on each section from the mud line to a depth of 395.14 mbsf. Below that depth, drilling disturbances induced a lack of coherence in the measurements. The conductivities varied between 1.41 and 5.26 × 10^{-3} cal/(°C × cm × s). Four main thermal conductivity units were distinguished: (a) the interval from the mud line to about 150 mbsf was characterized by highly variable data [1.6–5.26 × 10^{-3} cal/(°C × cm × s)] which underscore the heterogeneity of lithologic Units I and II (an average thermal conductivity of about 3.2 × 10^{-3} cal/(°C × cm × s) was estimated for this interval using a polynominal least-squares fitting curve); (b) the 150–300 mbsf interval shows more homogeneous values with an average ranging from 2.8 to 3.3 × 10^{-3} cal/(°C × cm × s) (this interval corresponds to lithologic Unit III); (c) the 300–360 mbsf interval again shows heterogeneous data which again can be correlated to the more diversified lithologic Subunit IVa; (d) the fine-grained interval 360–395 mbsf shows homogeneous data ranging around 3.2 × 10^{-3} cal/(°C · cm · s).

Undrained Shear Strength

The measured values of vane-shear-strength are listed in Table 13 and plotted vs. depth in Figure 29. No data were collected

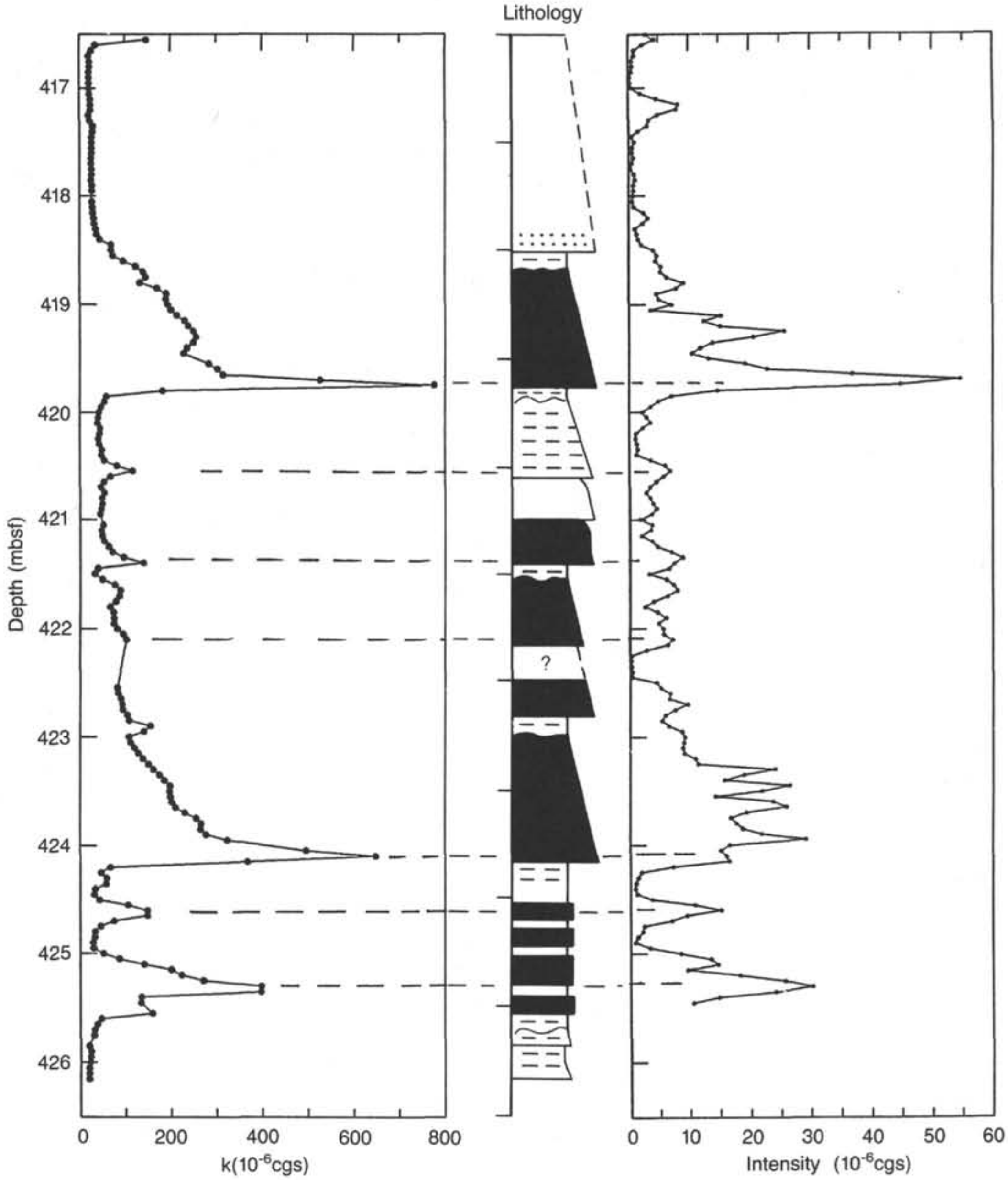

Figure 24. Magnetic susceptibility (left), lithostratigraphy (middle), and remanent magnetic intensity (right) vs. depth for Core 116-717C-48X. The susceptibility peaks are clearly correlated to gray mud turbidites. Several peaks show a graded morphology with a slow rise in susceptibility through the turbidite layer, the highest values at the base, and an abrupt return to lower values below the turbidite. The intensity values were measured after AF demagnetization at 9 mT. They show a close correlation with the susceptibility values. Plot conventions and lithostratigraphic legend as in Figure 23.

in the soupy sediments in the top 14 m of the holes, nor in the more lithified sediments below 350 mbsf.

The values for shear strength in the natural state varied between 9.5 kPa (20.0 mbsf) and 413.8 kPa (234.4 mbsf). Zones of high shear strength were found within the lithologic Unit III between 150 and 300 mbsf. Zones of low shear strength were found within the lithologic Units II and IV between 10–150 and 300–340 mbsf. The relative changes in shear strength corresponded with the content of silt and sand.

To estimate the state of consolidation a method described by Skempton (1970) was applied. This method relates undrained shear strength (cu) to effective overburden pressure (P_o). The effective overburden pressure was calculated for every depth interval using the equation applied for marine sediments by Richards (1962):

$$P_o = \gamma_w - \Delta\, d\ (\mathrm{kPa}) + P_i,$$

where

P_o is effective overburden pressure,

γ_w, the buoyant unit weight (wet-bulk density − density of water),

d, depth interval from the above sample, and

P_i, effective overburden pressure of the above sample.

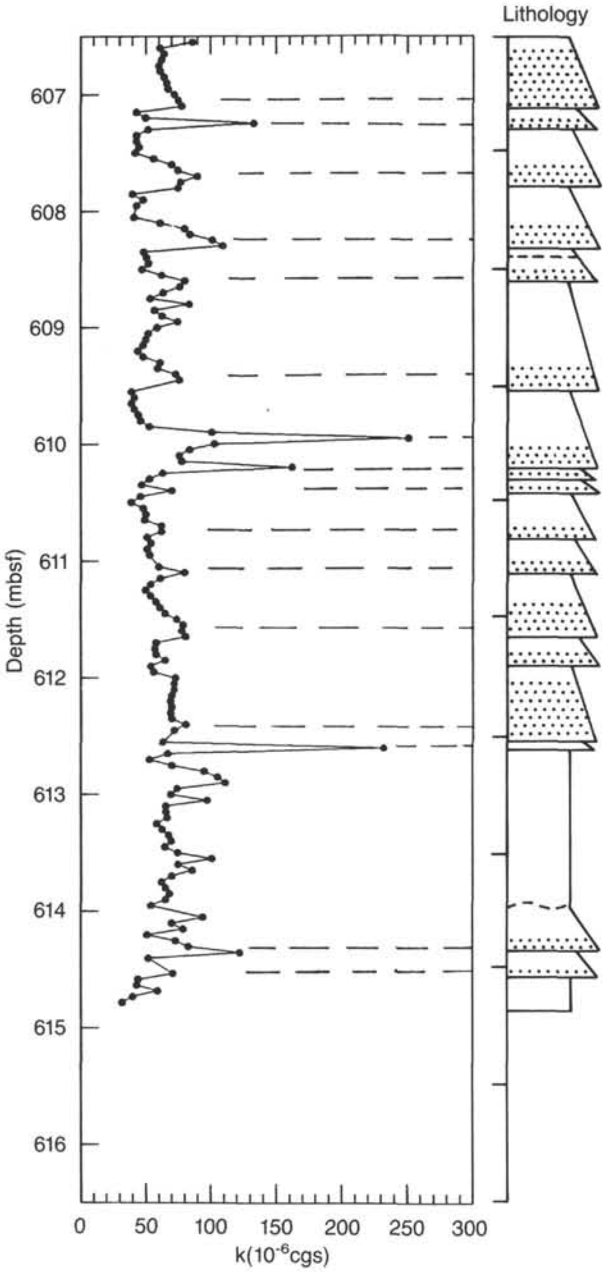

Figure 25. Lithostratigraphy (right) and susceptibility (left) vs. depth for Core 116-717C-68X. This core contains numerous silty turbidites which cause peaks in the susceptibility record. Note that most of the peaks correlate with the base of a turbidite layer. Plot conventions and lithostratigraphic legend as in Figure 23.

Skempton (1970) established that the ratio of undrained shear strength to effective overburden pressure in normally consolidated marine sediments ranges between 0.2 and 0.5. All values of the shear strength/overburden pressure ratio less than 0.2 are assumed to be underconsolidated and those greater than 0.5 are considered to be overconsolidated.

Figure 30 shows the ratio of shear strength to effective overburden pressure plotted versus depth for the sediments of Site 717C. It shows that most of the sediments are slightly underconsolidated, because the ratio of shear strength to effective overburden pressure is lower than 0.2.

HEAT FLOW

The region of intraplate deformation in the central Indian Basin is characterized by heat-flow values that show a great deal of variation, but which average higher than theoretically predicted for seafloor of its age (Weissel et al., 1980, Geller et al., 1983). The heat-flow measurements made during the site survey show both of these characteristics (Fig. 31). Measurements ranged from 44 to 166 mW/m^2 with a mean of 83.7 mW/m^2 and a standard deviation of 21.7 mW/m^2. Topographic corrections were not sufficient to account for the presence of such large variations over a short distance, and the large variation appears to result from the influence of water flow.

Site 717, located at the axis of a synclinal sedimentary structure developed over one of the rotated basement fault blocks, is designed to sample as complete a syn-deformation sequence as possible to serve as a reference section for the other Leg 116 sites. It is thus of interest to know the local heat flow as it is one factor to consider in comparitive studies with Site 718, which is located in an area of locally large heat flow. However, the site survey heat-flow line did not extend as far north as the location of Site 717 (Fig. 31) and therefore heat-flow measurements were carried out as part of the drilling program.

It was initially planned to take measurements using the Von Herzen hydraulic piston corer shoe (APC tool) during piston coring followed by measurements using the Barnes-Uyeda temperature/pore-water/pressure sampler (T-probe) until the sediment became too hard for it to penetrate further. However, on Core 116-717B-2H (Hole 717A missed the mudline and was abandoned), the core barrel broke off in the hole with the result that one of the two APC shoes on board was lost. When the lower section of the APC was bent on Core 116-717C-2H, it was decided to abandon piston coring and to start immediately with the XCB.

Temperature measurements were made in Hole 717C using the T-probe after Cores 116-717C-8X, -717C-12X, and -717C-16X. Good-quality measurements were obtained for the first and third deployment. No data were obtained for the second deployment because of a failure in the recorder. The temperature records are shown in Figures 32 and 33. The temperatures extrapolated to equilibrium are estimated to be 4.6°C [standard error (s.e.) = 0.12°] at 74.5 mbsf and 6.9°C (s.e. = 0.01°) at 131.5 mbsf. A third temperature point can be obtained from the bottom-water temperature that was measured to be 1.7°C on both lowerings. The temperatures are plotted against depth in Figure 34. They fall on a straight line that can be fit with a slope of 39.5°C/km (s.e. = 0.04°).

Thermal conductivity measurements from Site 717 are shown in Figure 28. The average value in the upper 130 m is 3.2×10^{-3} cal/(cm × °C × s) or 1.34 W/m × °C although there is considerable scatter in the data through the upper 150 m. Accepting that value for the conductivity, the heat flow at Site 717 is calculated to be 52.9 mW/m^2. Magnetic anomaly data ("Site Survey" chapter, Fig. 5) shows that the age of the crust beneath the Leg 116 sites is 78 Ma. The theoretical heat flow for 78 Ma-old crust is 53.5 mW/m^2 (Parsons and Sclater, 1977). Although lower than most of the heat-flow measurements taken further south during the site survey, the measurements at Hole 717C are indistinguishable from the theoretical value. This justifies the use of Hole 717C as a reference section for the effects of the higher heat flow at Site 718.

SEISMIC STRATIGRAPHY

Site 717 was chosen on the basis of single-channel seismic reflection data acquired with an air-gun source during a site sur-

Table 9. Index properties from Hole 717B.

Core	Sect.	Top (cm)	Bot. (cm)	Depth (mbsf)	Water content (% wet wt.)	Porosity (%)	Bulk density (g/cm^3)	Grain density (g/cm^3)
1H	1	113	118	1.13	50.68	73.02	1.50	2.66
1H	2	60	65	2.10	58.36	79.68	1.41	2.82
1H	2	113	118	2.63	53.92	76.57	1.48	2.82
2H	1	41	45	4.41	57.17	77.58	1.42	2.61
2H	2	90	94	6.40	31.44	56.36	1.83	2.85

vey by R/V *Robert D. Conrad* on cruise C2706 (Fig. 31). The *Conrad* seismic line was filtered using a time-varying band-pass filter, and a single-channel migration was employed to attempt to improve the resolution and to precisely locate the fault surfaces. The processing greatly improved the amount of detail that could be observed in the acoustic stratigraphy and removed most of the diffractions associated with the faults. However, discrete fault surfaces could not be determined and the faults appear as somewhat chaotic zones 4 to 8 shot points (190–375 m) wide.

The site chosen was located at time 1359Z, 11 July 1986, on the *Conrad* seismic record (Fig. 2). An alternative site was also chosen at 1334 UTC, 11 July 1986, 3.7 km from the prime site, on a parallel seismic line. Because the objective was to obtain a complete reference section, the site was chosen near the northern (lower) end of a tilted fault block at the axis of a synclinal structure developed in the sediments. The site was located approximately 1 km from a small fault (throw-on basement about 0.2 s) separating the target block from the next block to the north. The sediment thickness at the location chosen for the site is 1.96 s.

The seismic records across the fault can be divided into two first-order acoustic units separated by a prominent unconformity labeled "A" on Figures 2 and 35. The lower unit is consistently 1.15 to 1.35 s thick and reflectors within it are parallel and follow the basement. The upper sequence has a maximum thickness of about 0.7 s and thins, mainly through pinch-outs, toward the crest of the rotated blocks. The lower sequence can thus be interpreted as the predeformation section and the upper sequence as the sediments deposited during the deformation. Both sequences exhibit layering, but it is stronger and much more evident in the upper sequence. There is also a difference in the frequency content, with many more high-frequency reflectors in the upper sequence. These differences are not an artifact related to the absorption of energy with depth or to the time-varying filters used in processing since these characteristics can be noted both in the troughs and on the crests of the crustal blocks, while the thickness of the upper unit changes by more than 0.4 s between the two locations.

Curray and Moore (1971) divided the fan sediments into three major seismic stratigraphic units, termed "W," "Y," and "O," separated by unconformities, which they believed to be younger ("W") and older ("Y") fan sediments and prefan ("O") sediments of unknown origin. The two unconformities were traced on seismic records to sites drilled on DSDP Leg 22. The upper unconformity was penetrated at Site 218 where it was found to correspond to a zone of coarser, more sandy turbidites in the upper Miocene (Moore et al., 1974). The lower unconformity was reached at Site 217 and coincides with an apparent hiatus between Paleocene and middle Eocene (Moore et al., 1974). These authors noted that, on structural highs of the distal fan, the "W" fan deposits lap unconformably onto deformed "Y" sediments. This suggests that unconformity "A" is equivalent to the upper unconformity of Curray and Moore (1971).

The upper unit in the vicinity of Site 717 records a complex history of the motion on the fault blocks. The history varies somewhat from block to block. It includes an upper highly-layered sequence about 200 ms thick that is essentially flat lying and has an onlapping relationship with the uplifted sediments on the top of the blocks. This sequence unconformably overlies and truncates reflectors within the underlying sediments (unconformity "B" on Figs. 2 and 35). The syn-deformational sediments between unconformity "B" and unconformity "A" are characterized by numerous reflectors which are tilted up to the south (higher side of the tilted block) and which commonly terminate by pinching out against underlying reflectors, resulting in a thinning of this portion of the section toward the south. At the location chosen for Site 717, this sequence has a thickness of about 0.5 s so that unconformities "A" and "B" both appear to become conformable as Site 717 is approached. The goal at Site 717 was to obtain as complete a section as possible, at least through unconformity "A", to obtain a sedimentological and paleontological record and to serve as a benchmark section for the other sites where portions of the sequence above unconformity "A" are either missing or condensed.

JOIDES Resolution approached the site from the south and a seismic line was run over the site starting 20 km away to obtain a line across all three Leg 116 sites. A spar buoy was dropped when we passed the site and the line was continued to verify the position of the hole relative to the fault to the north. *JOIDES Resolution* then returned to the site and the beacon was dropped 1 km from the fault at the axis of the syncline. The seismic line obtained during this crossing of the site is shown in Figure 35.

Hole 717C was drilled to 828.2 mbsf. The upper portion of the section consisted of a thin upper layer (5.5 m) of mud turbidites and pelagic calcareous muds (lithologic Unit I) over a thicker (145 m) sequence of micaceous silt turbidites (lithologic Unit II). The silts abruptly overlie a sequence of mud turbidites interbedded with pelagic clays (lithologic Unit III) at 151 mbsf. The synthetic seismogram calculated for Site 719 from the well logs shows that the lithologic boundary appears to correspond to Unconformity "B". A similar unit of coarser grained turbidites was encountered at the top of DSDP Site 218, 1000 km to the northeast (Thompson, 1974).

The mud turbidite and pelagic clay sequence (lithologic Units III and IV) extends from 152 to 531.5 mbsf. This sequence has two intervals in which silty turbidites are found, at 302.5 to 335 mbsf (lithologic Unit IVa) and at 456 to 465 mbsf (lithologic Unit IVc). A synthetic seismogram constructed at Site 719, where well-log data is available, shows that there is a good correlation between the boundaries between mud turbidite and silty turbidite intervals and prominent reflectors on the seismic line (Fig. 35). The lowest lithologic unit (Unit V) is a sequence of silty turbidites and interbedded pelagic clays that extended from 534 mbsf to the bottom of the hole at 828.2 mbsf. The synthetic seismogram for Site 719 shows that the top of this unit does not correspond to unconformity "A", but rather to a reflector labeled "Z" on Figure 35. The interval between this reflector and

Table 10. Index physical properties from Hole 717C.

Core	Sect.	Top (cm)	Bot. (cm)	Depth (mbsf)	Water content (% wet wt.)	Porosity (%)	Bulk density (g/cm^3)	Grain density (g/cm^3)
2H	2	80	82	15.80	21.72	43.37	2.03	2.80
4X	1	28	30	27.28	32.34	56.06	1.81	2.71
5X	1	38	40	36.88	29.87	52.75	1.85	2.66
5X	1	110	113	37.60	24.28	45.90	1.96	2.68
6X	1	63	65	46.63	41.10	65.38	1.64	2.74
6X	1	113	118	47.13	39.04	63.31	1.67	2.73
7X	1	103	105	56.53	35.64	59.78	1.71	2.72
7X	2	2	4	57.02	21.02	41.09	2.06	2.66
8X	2	64	69	67.14	40.16	64.14	1.66	2.70
10X	1	76	81	75.26	41.27	63.54	1.72	2.51
10X	1	113	118	75.63	33.50	57.86	1.75	2.76
14X	2	19	22	104.69	29.79	53.64	1.90	2.77
15X	1	108	113	113.58	28.30	52.20	1.91	2.81
15X	1	122	127	113.72	28.84	51.87	1.91	2.70
16X	1	72	77	122.72	34.70	58.96	1.76	2.74
16X	1	109	115	123.09	24.21	46.31	1.97	2.74
19X	1	86	89	141.86	30.06	53.68	1.87	2.73
20X	1	110	113	151.60	28.18	52.04	1.91	2.81
20X	2	89	92	152.89	28.91	52.58	1.82	2.77
20X	3	80	85	154.30	26.40	49.13	1.90	2.73
20X	4	21	24	155.21	34.03	57.12	1.77	2.62
21X	1	107	110	161.07	33.76	56.14	1.72	2.54
21X	2	75	78	162.25	29.38	50.46	1.76	2.48
21X	3	70	73	163.70	31.79	55.08	1.75	2.67
21X	4	66	69	165.16	33.73	54.76	1.66	2.41
22X	1	19	22	169.69	37.33	61.33	1.70	2.70
22X	4	84	89	174.84	33.13	55.28	1.74	2.53
22X	5	15	20	175.65	33.45	56.53	1.73	2.62
23X	1	113	118	180.13	33.45	58.39	1.79	2.83
23X	3	113	118	183.13	34.37	57.17	1.72	2.58
23X	4	60	65	184.10	30.79	54.66	2.17	2.75
23X	5	113	118	186.13	35.44	60.09	2.00	2.78
23X	6	60	65	187.10	39.20	60.75	1.92	2.43
24X	1	20	26	188.70	35.29	58.79	1.71	2.65
24X	2	60	65	190.60	32.51	56.75	1.79	2.76
24X	3	120	124	192.70	34.88	59.12	1.74	2.74
24X	4	60	65	193.60	31.54	54.53	1.80	2.64
24X	5	113	117	195.63	34.09	57.36	1.72	2.64
24X	6	60	65	196.60	33.37	56.86	1.76	2.67
25X	1	114	118	199.14	30.74	54.66	1.86	2.75
25X	2	60	64	200.10	33.32	56.56	1.78	2.64
25X	3	113	117	202.13	34.71	57.19	1.73	2.54
25X	4	60	64	203.10	32.25	56.09	1.81	2.72
25X	5	113	117	205.13	33.17	56.77	1.85	2.68
25X	6	60	64	206.12	36.34	58.25	1.71	2.47
26X	1	70	73	208.20	31.70	55.54	1.81	2.73
26X	3	116	120	211.66	32.97	56.59	1.80	2.69
26X	4	45	49	212.45	27.83	50.57	1.73	2.69
26X	5	113	118	214.63	34.54	58.44	1.77	2.70
26X	6	66	70	215.66	28.49	52.38	1.76	2.80
26X	7	10	14	216.60	31.03	53.98	1.82	2.64
27X	1	143	146	218.43	34.83	59.05	1.75	2.73
27X	2	62	65	219.12	36.88	61.38	1.74	2.76
27X	3	147	150	221.47	30.81	54.65	1.87	2.74
27X	4	60	63	222.10	34.38	57.06	1.75	2.57
27X	5	147	150	224.47	28.32	50.56	1.88	2.62
27X	6	65	68	225.15	36.99	61.72	1.71	2.78
28X	1	128	132	227.78	35.14	58.48	1.76	2.63
28X	2	63	67	228.63	33.43	56.62	1.78	2.63
28X	3	147	150	230.97	28.91	51.52	1.87	2.65
28X	4	63	67	231.63	32.42	55.33	1.81	2.62
28X	5	11	15	232.61	28.83	52.79	1.90	2.80
29X	1	142	145	237.42	34.35	58.83	1.78	2.77
29X	2	63	66	238.13	38.26	62.57	1.71	2.73
29X	3	131	134	240.31	33.46	56.53	1.75	2.62
29X	4	62	65	241.12	31.83	57.16	1.90	2.90
29X	5	141	143	243.41	31.62	54.46	1.83	2.62
29X	6	61	64	244.11	34.92	59.71	1.80	2.80
30X	1	118	123	246.68	32.33	55.10	1.78	2.60
30X	2	60	64	247.60	32.10	56.26	1.85	2.76
30X	4	61	64	250.61	31.77	55.23	1.84	2.69
30X	5	112	116	252.62	35.21	59.56	1.75	2.75
30X	6	63	67	253.63	30.06	54.37	1.90	2.81
31X	1	63	67	255.63	26.73	48.24	1.47	2.59
31X	2	113	117	257.63	29.46	53.41	1.87	2.78
31X	3	20	24	258.20	29.23	53.55	1.89	2.83
32X	1	117	121	265.67	26.24	48.41	1.91	2.68
33X	2	64	68	276.14	29.33	53.40	1.89	2.80

Table 10 (continued).

Core	Sect.	Top (cm)	Bot.	Depth (mbsf)	Water content (% wet wt.)	Porosity (%)	Bulk density (g/cm³)	Grain density (g/cm³)
33X	3	113	117	278.13	34.28	57.95	1.76	2.68
33X	4	61	65	279.11	31.24	54.94	1.81	2.72
33X	5	113	117	281.13	32.63	56.85	1.80	2.76
33X	6	60	64	282.10	26.44	49.69	1.95	2.79
34X	1	118	123	284.68	28.92	52.77	1.93	2.79
34X	2	90	94	285.90	33.70	57.74	1.80	2.72
34X	3	113	118	287.63	34.17	57.91	1.77	2.69
35X	1	113	117	294.13	33.54	56.20	1.76	2.58
35X	2	90	94	295.40	27.19	50.62	1.91	2.78
35X	3	113	118	297.13	34.17	57.91	1.77	2.69
35X	4	60	64	298.10	29.47	52.77	1.86	2.71
35X	5	116	119	300.16	36.89	60.37	1.72	2.64
35X	6	60	64	301.10	32.10	56.74	1.88	2.81
36X	1	116	119	303.66	37.01	60.49	1.72	2.64
36X	2	63	68	304.63	29.14	53.63	2.04	2.85
36X	3	120	124	306.70	26.76	49.52	1.80	2.72
36X	4	60	64	307.60	25.24	47.04	1.95	2.67
36X	5	124	128	309.74	25.46	49.19	1.94	2.88
36X	6	61	65	310.61	31.39	55.39	1.84	2.75
37X	2	136	139	314.86	28.44	52.74	1.91	2.85
37X	3	72	75	315.72	24.01	45.92	2.06	2.73
38X	2	88	90	323.88	27.45	50.04	1.89	2.69
38X	3	56	59	325.06	25.75	48.57	1.92	2.76
39X	1	38	41	331.38	22.61	44.07	2.03	2.74
40X	1	110	114	341.60	23.49	46.04	1.98	2.82
40X	2	55	59	342.55	47.05	70.00	2.29	2.65
40X	4	32	36	345.32	30.20	54.11	1.82	2.76
40X	5	115	119	347.65	31.06	54.30	1.81	2.67
40X	6	47	50	348.47	31.15	51.85	1.82	2.41
41X	1	40	42	350.40	32.22	55.63	1.79	2.67
42X	2	106	109	362.06	25.19	48.35	1.96	2.82
42X	3	72	75	363.22	23.99	45.92	1.96	2.73
42X	4	87	90	364.87	20.77	42.23	2.08	2.83
42X	5	73	76	366.23	24.22	46.40	1.99	2.75
42X	6	104	107	368.04	25.08	46.99	1.95	2.69
43X	1	62	64	369.62	32.29	55.97	1.80	2.70
43X	3	59	62	372.59	29.40	52.81	1.82	2.72
43X	3	59	62	372.59	24.14	46.33	1.94	2.75
43X	4	110	113	374.60	29.95	52.83	1.83	2.66
43X	5	59	63	375.59	31.62	54.83	1.79	2.66
43X	6	110	113	377.60	23.53	45.88	2.04	2.80
44X	1	109	111	379.59	32.73	56.16	1.78	2.67
44X	2	60	62	380.60	30.00	53.65	1.82	2.74
44X	3	113	115	382.63	31.16	55.23	1.83	2.76
44X	4	60	62	383.60	28.02	50.94	1.71	2.71
44X	5	113	115	385.63	24.42	47.23	1.97	2.81
44X	6	60	62	386.60	25.02	47.78	1.96	2.78
45X	1	113	115	389.13	26.83	49.78	1.91	2.74
45X	1	113	115	389.13	22.61	44.31	2.00	2.76
45X	2	60	62	390.10	27.84	50.76	1.88	2.71
45X	3	113	115	392.13	24.46	45.95	1.94	2.66
45X	4	60	62	393.10	25.06	47.59	1.97	2.76
45X	6	59	61	396.09	22.08	43.42	2.00	2.75
46X	2	90	92	399.90	27.29	49.99	1.89	2.70
46X	3	112	114	401.62	25.17	47.44	1.94	2.72
46X	4	59	61	402.59	27.88	50.65	1.98	2.69
47X	2	60	62	409.10	29.60	52.90	1.84	2.71
47X	3	10	12	410.10	22.53	44.14	1.98	2.76
48X	2	114	118	419.14	29.16	52.27	1.86	2.70
48X	4	92	96	421.92	26.52	48.53	1.91	2.65
48X	6	41	46	424.41	23.77	46.40	2.00	2.82
49X	1	146	150	427.46	33.04	56.52	1.75	2.67
49X	2	61	64	428.11	30.95	55.23	1.81	2.79
49X	4	63	64	431.13	26.20	49.12	1.94	2.76
50X	2	59	61	437.59	29.25	53.51	1.87	2.82
50X	4	59	61	440.59	30.86	55.27	1.85	2.81
50X	6	26	28	443.26	25.65	48.12	1.93	2.73
51X	2	12	14	446.62	23.97	46.16	1.99	2.76
51X	3	93	95	448.93	27.63	51.34	1.90	2.80
51X	4	41	43	449.91	24.44	47.10	1.99	2.79
52X	1	104	107	455.54	27.32	50.71	1.91	2.78
52X	2	134	137	457.34	25.23	47.88	1.95	2.76
53X	2	56	60	466.06	20.74	42.25	2.13	2.84
53X	4	138	142	469.88	22.62	44.80	2.02	2.82
53X	5	63	65	470.63	21.04	43.01	2.06	2.88
53X	6	120	122	472.70	27.85	51.56	1.92	2.80
54X	1	113	118	474.63	33.33	57.14	1.76	2.70

Table 10 (continued).

Core	Sect.	Top (cm)	Bot. (cm)	Depth (mbsf)	Water content (% wet wt.)	Porosity (%)	Bulk density (g/cm^3)	Grain density (g/cm^3)
54X	3	113	118	477.63	23.58	46.01	2.00	2.80
54X	4	47	49	478.47	23.07	44.69	2.00	2.74
54X	5	111	116	480.61	21.64	43.35	2.00	2.81
54X	6	142	144	482.42	29.81	53.01	1.87	2.69
54X	7	10	12	482.60	24.51	47.83	2.00	2.87
55X	1	57	59	483.57	25.71	48.96	1.95	2.81
55X	2	73	75	485.23	28.50	50.69	1.89	2.61
55X	3	47	50	486.47	20.57	47.03	2.06	3.48
55X	C	34	37	486.95	27.90	50.37	1.90	2.66
56X	1	68	70	493.18	26.16	49.09	1.94	2.76
56X	4	123	125	498.23	24.04	46.58	2.04	2.80
56X	6	126	129	501.26	26.43	49.28	1.95	2.74
56X	7	13	15	501.63	24.39	46.37	1.95	2.72
57X	1	75	77	502.75	24.93	48.15	1.97	2.84
57X	3	65	66	505.65	25.83	48.63	1.95	2.76
57X	5	88	91	508.88	26.89	49.84	2.02	2.74
58X	1	67	69	512.17	28.08	50.62	1.92	2.66
58X	2	64	66	513.64	31.87	51.70	1.82	2.32
58X	5	40	42	517.91	26.83	50.43	1.96	2.81
59X	1	12	16	521.12	24.51	47.42	1.95	2.82
59X	2	22	26	522.72	23.71	45.92	1.99	2.77
59X	3	92	97	524.92	25.09	48.40	2.00	2.84
59X	4	45	47	525.95	24.58	48.16	2.01	2.89
59X	6	139	144	529.89	28.45	52.36	1.89	2.80
60X	1	114	118	531.64	23.83	46.38	1.98	2.81
60X	2	62	66	532.62	23.66	46.24	1.99	2.82
61X	1	22	26	540.22	21.56	43.49	2.06	2.84
61X	2	128	132	542.78	18.90	39.06	2.15	2.79
63X	1	134	136	560.34	25.57	48.80	1.95	2.82
63X	2	50	53	561.00	23.50	46.20	2.01	2.84
64X	1	141	145	569.91	22.06	44.08	2.04	2.83
64X	2	38	42	570.38	26.11	49.70	1.94	2.84
65X	2	76	78	580.26	22.91	45.49	2.03	2.85
65X	3	41	44	581.41	25.19	48.43	1.95	2.83
65X	6	21	23	585.71	23.00	45.74	2.01	2.86
65X	C	17	20	586.18	24.59	46.99	1.96	2.76
66X	1	115	117	588.65	22.47	44.71	2.02	2.83
66X	2	14	16	589.14	22.07	43.99	2.08	2.82
66X	3	83	86	591.33	22.54	44.48	2.03	2.80
66X	4	21	23	592.21	52.99	65.91	2.04	1.72
68X	1	88	91	607.38	24.30	47.47	1.97	2.86
68X	2	106	108	609.06	23.20	45.90	2.02	2.85
68X	3	96	98	610.46	23.95	46.86	1.98	2.84
68X	5	70	72	613.20	22.40	44.01	2.00	2.76
69X	1	115	117	617.15	22.68	44.68	2.01	2.80
69X	2	33	36	617.83	22.03	44.27	2.04	2.85
69X	3	63	66	619.63	21.96	44.19	2.11	2.86
70X	2	65	67	627.65	23.78	46.55	2.37	2.83
70X	3	85	87	629.35	21.74	43.43	2.02	2.80
70X	4	58	60	630.58	19.77	40.62	2.17	2.82
70X	4	58	60	630.58	19.77	40.62	2.17	2.82
70X	6	70	72	633.70	20.69	41.34	2.06	2.74
70X	C	6	8	634.56	20.53	41.33	2.13	2.77
71X	1	50	53	635.50	21.13	42.52	2.03	2.80
71X	2	49	51	636.99	20.36	41.65	2.07	2.83
71X	3	42	46	638.42	18.37	38.98	2.10	2.88
71X	4	15	17	639.65	21.27	42.60	2.03	2.79
71X	C	14	16	642.85	20.81	42.35	2.13	2.84
72X	1	83	85	645.33	20.45	40.96	2.09	2.74
72X	2	84	86	646.84	21.89	43.75	2.01	2.82
73X	2	61	63	656.11	20.43	41.33	2.07	2.79
74X	1	112	115	664.62	21.13	42.81	2.04	2.84
75X	1	103	108	674.03	20.44	41.06	2.12	2.75
75X	2	78	83	675.28	20.94	41.98	2.08	2.77
75X	3	105	110	677.05	18.75	39.11	2.13	2.83
75X	4	65	70	678.15	20.31	41.33	2.10	2.81
76X	1	38	43	682.88	14.07	30.97	2.28	2.78
76X	2	90	97	684.90	21.38	42.92	2.06	2.81
76X	3	121	126	686.71	15.16	32.31	2.22	2.71
76X	4	46	51	687.46	18.03	37.91	2.21	2.82
77X	1	126	129	693.26	18.09	37.76	2.15	2.79
77X	2	36	40	693.86	19.24	39.09	2.13	2.74
77X	3	123	126	696.23	22.14	43.75	2.03	2.78
77X	4	23	27	696.73	18.81	38.70	2.09	2.77
77X	5	118	123	699.18	19.98	41.06	2.09	2.83
77X	6	40	44	699.90	19.56	39.33	2.05	2.71
78X	1	121	123	702.71	21.09	42.68	2.10	2.83

Table 10 (continued).

Core	Sect.	Top (cm)	Bot. (cm)	Depth (mbsf)	Water content (% wet wt.)	Porosity (%)	Bulk density (g/cm³)	Grain density (g/cm³)
78X	2	74	77	703.74	21.18	41.96	2.06	2.73
78X	3	58	61	705.08	19.80	39.77	2.09	2.72
78X	4	109	112	707.09	20.48	40.56	2.09	2.69
78X	5	114	117	708.64	20.37	41.61	2.09	2.83
78X	6	143	146	710.43	19.81	40.86	1.86	2.84
79X	1	116	118	712.16	19.76	40.09	2.12	2.76
79X	2	7	9	712.57	20.26	41.32	2.11	2.81
79X	3	110	114	715.10	21.31	43.07	2.09	2.84
79X	4	62	64	716.12	21.02	41.97	2.16	2.76
79X	5	134	136	718.34	20.57	41.89	2.13	2.83
79X	6	24	26	718.74	21.24	42.90	2.12	2.83
80X	1	109	111	721.59	19.53	39.96	2.15	2.79
80X	2	110	112	723.10	20.38	41.75	2.13	2.84
80X	3	105	108	724.55	22.19	44.20	2.07	2.82
83X	1	65	69	749.65	17.61	38.09	2.26	2.93
84X	1	2	4	758.52	26.71	48.94	2.07	2.67
84X	1	37	40	758.87	20.27	41.46	2.07	2.83
84X	2	26	28	760.26	18.77	39.18	2.18	2.83
84X	3	23	25	761.73	20.27	41.82	2.16	2.87
84X	C	11	13	762.86	19.30	39.91	2.14	2.82
85X	1	80	83	768.80	18.99	39.20	2.15	2.79
85X	2	112	115	770.62	18.58	39.10	2.17	2.86
85X	3	117	120	772.17	18.61	39.32	2.22	2.88
85X	4	98	101	773.48	20.16	40.94	2.11	2.79
85X	5	123	125	775.23	21.04	42.76	2.11	2.85
85X	6	105	108	776.55	17.89	38.90	2.13	2.97
87X	1	134	138	788.34	19.07	39.54	2.20	2.82
87X	2	87	91	789.37	24.22	47.02	2.04	2.82
89X	1	43	45	806.43	20.39	41.39	2.10	2.80
90X	1	35	39	809.55	18.40	38.90	2.18	2.87
91X	1	87	89	819.57	18.45	38.10	2.18	2.76
91X	2	58	60	820.78	24.24	47.47	2.03	2.87
91X	3	38	40	822.08	18.23	39.20	2.29	2.94

"A" does thin over the top of the rotated blocks, but not nearly as much as overlying intervals do. Unconformity "A" occurs about 0.09 s (90 m) below the top of lithologic Unit V at about 620 mbsf. The age determined for this depth by interpolation between paleontological dates is 7.5 Ma.

LOGGING

Logging was attempted but the bottom-hole assembly parted from the drill string before the logging tools reached open hole (See "Operations" section).

SUMMARY AND CONCLUSIONS

Three holes were drilled at Site 717 on the distal Bengal Fan in a water depth of 4735 m. Hole 717A missed the mud line so that a second hole was spudded-in at a depth a few meters shallower. Holes 717B and 717C together drilled a continuous section from the seafloor to 828.2 mbsf. Core recovery averaged 58%, being good in the finer grained mud lithologies and poor in unconsolidated silts. Only two APC cores were obtained, but a new record for XCB penetration was set at total hole depth. Loss of the bottom-hole assembly near the mud line prevented the scheduled logging run being carried out.

Site 717 was drilled on a tilted fault block into the thickest part of the sedimentary section between adjacent faults (Fig. 2). Two main units are identified on the seismic reflection records, a lower predeformational sequence (1.15 to 1.35 s thick) and an upper postdeformational sequence (0.7 s thick). Seismic reflectors "A" and "B", representing unconformities on the uplifted parts of fault blocks (Fig. 2), appear to be conformable at Site 717.

The stratigraphic section recovered ranges from late Quaternary to the base of late Miocene and has been divided into five main lithologic units (Fig. 4). Unit I (0-5.5 mbsf) represents the topmost muds, mud turbidites, and pelagites of (?) Holocene and latest Pleistocene age. Although the surface layer was probably washed away during penetration, a minimum sediment accumulation rate of about 25 m/m.y. can be calculated. Unit II (5.5-152 mbsf) is dominated by micaceous silt turbidites, with thin intervening muds and pelagites, deposited very rapidly during the late Pleistocene at a rate probably in excess of 350 m/m.y. The base of Unit II corresponds to seismic reflector "B" (Fig. 35). Units III and IV (152-533.3 mbsf) together represent a thick section of mainly mud turbidites and thin interbedded pelagic clays that accumulated at a slower average rate of nearly 70 m/m.y. through the latest Miocene to early Pleistocene. Distinctive biogenic mud turbidites were characteristic of the upper part of these units and at least two distinct pulses of silty turbidites occurred within Unit IV. The top of Unit V corresponds to seismic reflector "Z" (Fig. 35). The unit (533-828.2 mbsf) comprises repeated micaceous silt and silt-mud turbidites separated by intervals (5-20 m thick) of muds and pelagic clays. The average accumulation rate for the whole of this late Miocene interval is about 90-100 m/m.y., although it is assumed that the silt turbidites were deposited much more rapidly than the intervening muds. Seismic reflector "A" occurred at approximately 90 m below the top of the unit (Fig. 35).

The biostratigraphic control at Site 717 was based largely on nannofossils, as most of the other microfossil groups were either poorly preserved or absent in all but the uppermost unit. The site has clearly been below or very close to the carbonate compensation depth (CCD) from at least 10 Ma to the present. Slightly better preservation of carbonate microfossils from about 0.5 m.y. onward compared with the very barren pelagic intervals before that time indicates a general increase in the depth of the CCD to the present. Most of the biota studied have been resedimented as turbidites derived from shallower water, but the ab-

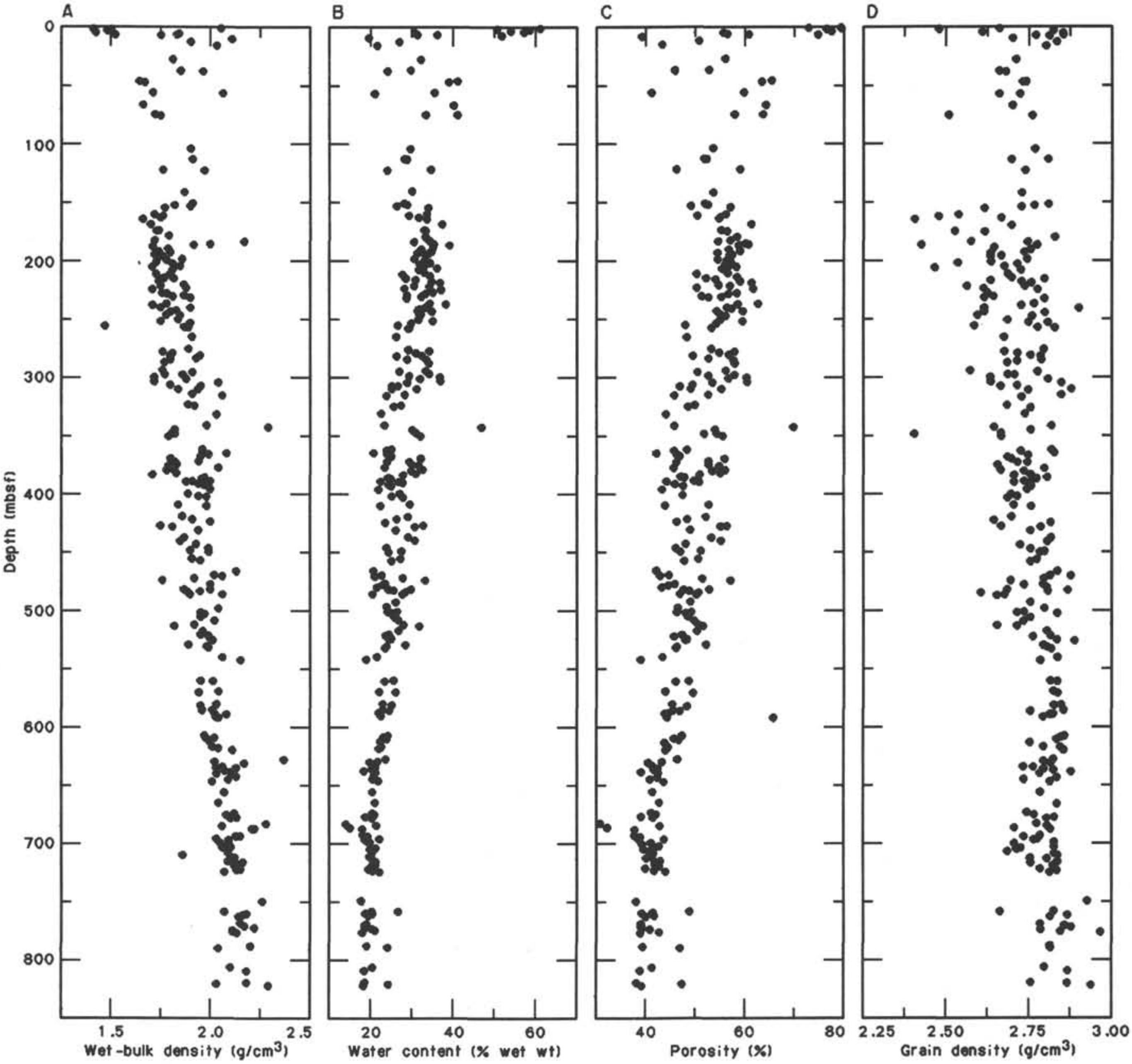

Figure 26. Index properties at Site 717. Data are from Holes 717B and 717C.

sence of mixing between nannofossil zones indicates that resedimentation took place shortly after deposition. The almost complete absence of siliceous microfossils beneath the supposed equatorial upwelling, high-productivity zone remains a problem to be resolved.

For the most part, the downhole pore-water geochemical trends were typical of those found in similar sequences on previous DSDP/ODP legs (Figs. 8 and 11 to 15). The data for Ca, Mg, alkalinity, and organic compounds together suggest that most of the section should be subject to carbonate precipitation. The downhole carbonate measurements indicate higher carbonate content within the silts than the muds so that precipitation may be taking place in the more permeable beds. Visual examination of smear slides revealed a small amount of rhombic authigenic carbonate and much silt and clay-sized carbonate of indeterminate origin. Toward the base of the hole certain horizons have been fully lithified with carbonate cement. The pore water from muds in the very bottom core had a completely different chemistry (high Si, Ca, and alkalinity; low Mg and chlorinity) with a distinct odor of polyalkylamine compounds derived from the fermentation of organic-rich sapropelic material. The most likely explanation involves the origin of the water from a zone of higher temperature water-sediment interaction, a convective circulation system, and horizontal flow of water beneath an impermeable horizon near 800 mbsf.

Total organic carbon measurements showed two features of interest at Site 717 (Fig. 10). In the upper 530 m (Units I to IV), the content ranged from about 0.5% to 3% and shows a marked cyclicity of between 20 and 40 m (i.e., half-million year cycles). In the lower silty Unit V, the content dropped to generally less than 0.5%. Shipboard Rock Eval and visual description indicated that this carbon is of terrigenous origin, mostly inertinite

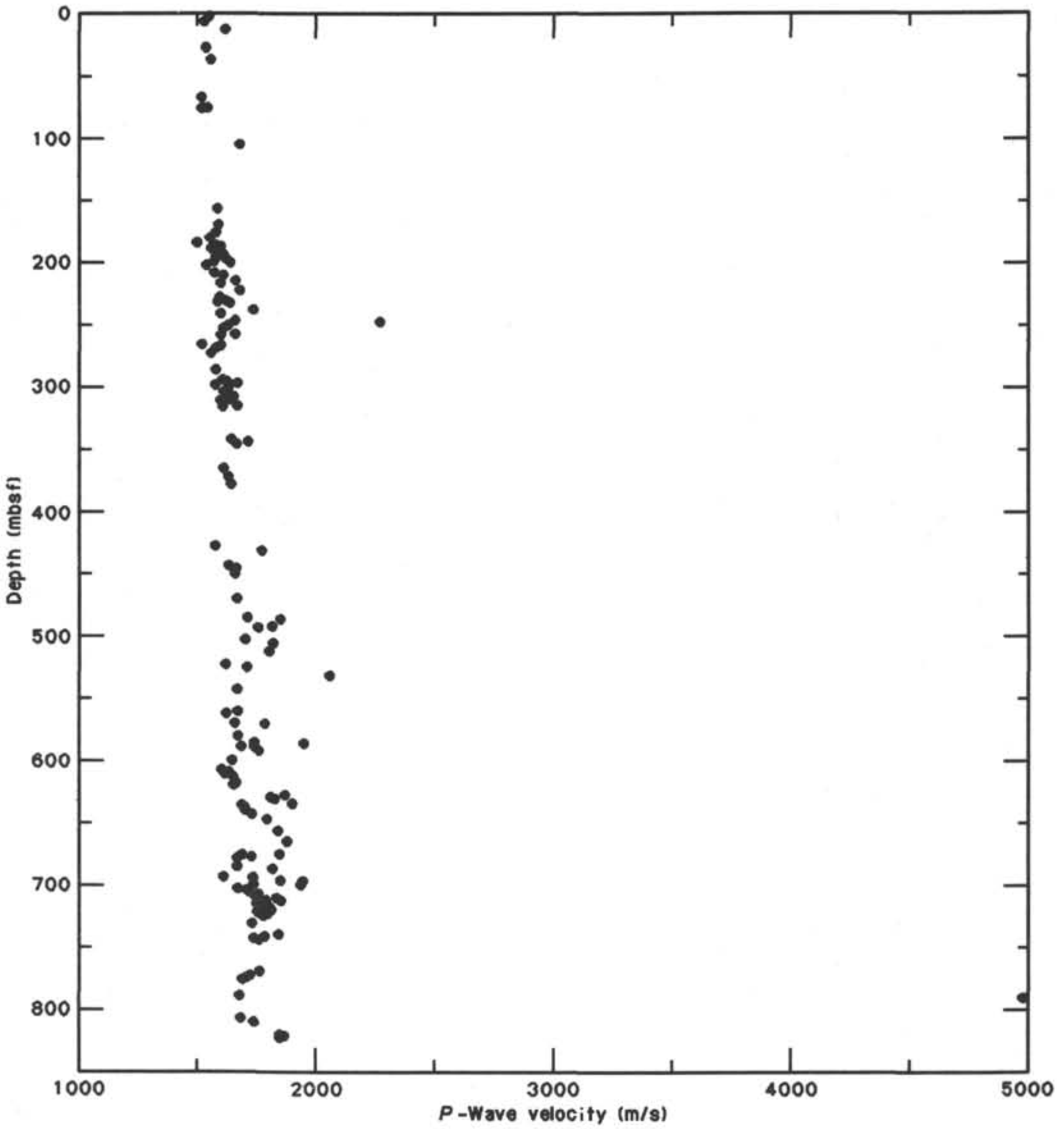

Figure 27. Sonic velocity vs. depth at Site 717.

(Type IV) and some vitrinite (Type III). The content was highest in the dark-gray muds and lowest in the silts. Methane contents were low and methane/ethane ratios very high, so that although a gas-prone source rock exists, the maturity is low.

Conventional paleomagnetic measurements were made on board, but due to the equatorial location, nonorientated XCB cores, and extensive core disturbance in the older sections recovered, reliable magnetostratigraphy was not possible. However, the magnetic susceptibility properties of different lithofacies types proved extremely interesting. In part, high susceptibility correlates closely with the dark-gray mud turbidites and in part, it follows a larger scale periodicity (Fig. 22). These results and the nature and distribution of the magnetic or paramagnetic material involved are under further investigation.

Sediment physical properties show consistent downhole variation (Figs. 26A to 26C), although many of the data from deeper within the section have been adversely influenced by drilling disturbance. The sense and downhole increase in the anisotropy of sonic velocity, which showed that the horizontal velocity through the sediments is greater than the vertical, is particularly significant. This provided clear evidence that the sediments are experiencing a lateral stress in excess of the vertical stress due to overburden pressure. The thermal conductivity measurements convert downhole temperatures obtained from the heat probe into heat flow. The resulting heat flow calculated through the top 150 m of section at Site 717 is about normal for the age of the ocean crust.

In summary, the principal results of drilling at Site 717 are as follows.

1. A successful reference section was obtained through seismic reflectors "A" and "B" to the base of the late Miocene. There is evidence of lateral stress, but heat flow is normal and no marked unconformities are apparent.

2. A very good record of extremely distal fan sedimentation was recovered showing the nature, thickness, and vertical sequence of turbidites that have been transported over 2500 km. Correlations can be made with a similar sequence of fan sediments recovered at Site 218 some 1000 km further north.

3. At least three different sources of turbidites can be tentatively identified: silts and muds from the Ganges-Brahmaputra delta front, dark-gray organic-rich muds from the upper slope in the northern or western Bay of Bengal, and greenish biogenic turbidites from a more local seamount or outer shelf source.

Table 11. Sonic velocity from Site 717.

Hole	Core-Sect.	Interval (cm)	Depth (mbsf)	Sonic velocity (km/s)
B	01H-2	060–065	002.13	1.550
B	02H-2	090–094	006.42	1.530
B	02H-6	113–115	012.61	1.620
C	04X-1	028–030	027.29	1.540
C	05X-1	038–040	036.81	1.560
C	08X-2	064–069	067.15	1.520
C	10X-1	076–081	075.29	1.545
C	10X-1	113–118	075.65	1.520
C	14X-2	019–022	104.70	1.680
C	20X-4	021–024	156.72	1.586
C	22X-1	019–022	169.70	1.590
C	22X-5	015–020	175.70	1.580
C	23X-1	113–118	180.15	1.555
C	23X-4	060–065	184.13	1.500
C	23X-5	113–118	186.15	1.580
C	23X-6	060–065	187.13	1.600
C	24X-1	020–024	188.71	1.560
C	24X-3	113–117	192.65	1.580
C	24X-4	060–065	193.63	1.610
C	24X-5	120–125	195.80	1.580
C	24X-6	060–065	196.63	1.620
C	25X-1	114–118	199.15	1.570
C	25X-2	060–064	200.12	1.640
C	25X-3	113–117	202.15	1.540
C	26X-1	070–073	208.21	1.573
C	26X-2	124–127	210.25	1.610
C	26X-5	113–118	214.65	1.662
C	26X-7	010–014	216.62	1.599
C	27X-4	060–063	222.62	1.680
C	28X-1	128–132	227.79	1.595
C	28X-3	147–150	230.98	1.623
C	28X-4	063–067	231.65	1.586
C	28X-5	011–015	232.63	1.637
C	29X-2	063–066	238.15	1.737
C	29X-4	062–065	241.14	1.599
C	30X-1	118–123	246.69	1.660
C	30X-2	060–064	247.62	2.270
C	30X-4	061–064	250.62	1.630
C	30X-5	112–126	252.64	1.610
C	31X-2	113–117	257.65	1.660
C	31X-3	020–024	258.22	1.600
C	32X-1	117–121	265.69	1.520
C	33X-2	064–068	266.65	1.600
C	33X-3	113–117	268.64	1.580
C	33X-6	060–064	272.62	1.560
C	34X-2	090–094	285.92	1.580
C	35X-1	113–117	294.00	1.608
C	35X-2	090–094	295.42	1.626
C	35X-4	060–064	298.12	1.578
C	35X-3	060–064	296.62	1.670
C	35X-6	060–064	301.12	1.633
C	36X-1	116–119	303.67	1.612
C	36X-2	063–068	304.65	1.622
C	36X-3	120–124	306.72	1.628
C	36X-4	060–064	307.62	1.655
C	36X-5	124–128	309.76	1.636
C	36X-6	061–065	310.63	1.600
C	37X-2	136–139	314.86	1.670
C	37X-3	072–073	315.74	1.609
C	40X-1	110–114	341.62	1.645
C	40X-3	104–107	343.55	1.716
C	40X-4	032–036	345.34	1.667
C	42X-4	087–090	364.88	1.612
C	43X-2	110–113	371.62	1.632
C	43X-6	110–113	377.62	1.644
C	49X-1	146–150	427.48	1.577
C	49X-4	063–064	431.13	1.773
C	50X-6	026–028	443.27	1.634
C	52X-1	104–107	445.55	1.665
C	51X-4	041–043	449.92	1.660
C	53X-4	138–140	469.90	1.668
C	55X-2	073–075	485.24	1.712
C	55X-3	047–050	486.48	1.851
C	55X-C	035–037	492.30	1.817
C	56X-1	068–070	493.18	1.757
C	57X-1	075–077	502.76	1.703
C	57X-3	065–068	505.65	1.821
C	58X-1	067–069	512.18	1.804

Table 11 (continued).

Hole	Core-Sect.	Interval (cm)	Depth (mbsf)	Sonic velocity (km/s)
C	59X-2	022–026	522.74	1.619
C	59X-3	092–097	524.94	1.710
C	60X-1	114–118	531.66	2.060
C	61X-2	128–132	542.80	1.670
C	63X-1	134–136	560.35	1.672
C	63X-2	050–053	562.01	1.624
C	64X-1	141–145	569.95	1.660
C	64X-2	038–042	570.40	1.787
C	65X-2	076–078	580.27	1.673
C	65X-6	021–023	585.72	1.743
C	65X-C	017–020	586.30	1.951
C	66X-1	115–117	588.66	1.687
C	66X-2	014–016	589.15	1.742
C	66X-4	021–025	592.23	1.761
C	67X-2	120–122	599.71	1.648
C	68X-1	088–091	607.40	1.604
C	68X-2	106–108	609.07	1.635
C	68X-3	096–098	610.47	1.616
C	68X-5	070–072	613.21	1.653
C	69X-1	115–117	617.16	1.661
C	69X-2	033–036	617.85	1.666
C	69X-3	063–066	619.65	1.654
C	70X-2	065–067	627.66	1.872
C	70X-3	085–087	629.36	1.811
C	70X-4	058–060	630.59	1.829
C	70X-C	006–008	634.57	1.903
C	71X-1	050–053	635.51	1.689
C	71X-2	049–051	637.00	1.699
C	71X-3	042–046	638.44	1.703
C	71X-4	015–017	639.66	1.704
C	71X-C	014–016	642.85	1.732
C	72X-2	083–086	646.85	1.796
C	73X-2	061–062	656.12	1.843
C	74X-1	112–115	664.63	1.881
C	75X-1	103–108	675.05	1.850
C	75X-2	078–083	675.30	1.690
C	75X-3	105–110	677.07	1.730
C	75X-4	065–070	678.17	1.670
C	76X-2	090–097	684.94	1.670
C	76X-3	121–126	686.73	1.820
C	77X-1	126–129	693.26	1.612
C	77X-2	036–040	693.88	1.737
C	77X-3	123–126	696.25	1.853
C	77X-4	023–027	696.75	1.948
C	77X-5	118–125	699.21	1.740
C	77X-6	040–044	699.92	1.939
C	78X-1	121–123	702.72	1.672
C	78X-2	074–077	703.75	1.710
C	78X-3	058–061	705.10	1.720
C	78X-4	109–112	707.11	1.760
C	78X-5	114–117	708.65	1.744
C	78X-6	143–146	710.45	1.837
C	79X-1	116–118	712.17	1.793
C	79X-2	007–009	712.58	1.855
C	79X-3	110–114	715.12	1.753
C	79X-4	062–064	716.13	1.790
C	79X-5	134–136	718.35	1.809
C	79X-6	024–026	719.85	1.815
C	80X-1	109–111	721.60	1.755
C	80X-2	110–112	723.11	1.799
C	80X-3	105–108	724.57	1.780
C	83X-1	065–069	730.67	1.733
C	84X-1	002–004	739.53	1.845
C	84X-2	026–028	741.27	1.786
C	84X-3	023–025	742.74	1.740
C	84X-C	011–013	743.90	1.761
C	85X-1	080–083	768.81	1.765
C	85X-3	117–120	772.18	1.723
C	85X-4	098–101	773.49	1.710
C	85X-5	123–125	775.24	1.690
C	87X-1	134–138	788.35	1.680
C	87X-C	031–035	790.29	4.978
C	89X-1	041–045	806.43	1.685
C	90X-1	035–039	809.55	1.740
C	91X-1	087–089	819.57	1.849
C	91X-2	058–060	820.78	1.869
C	91X-3	038–040	822.08	1.850

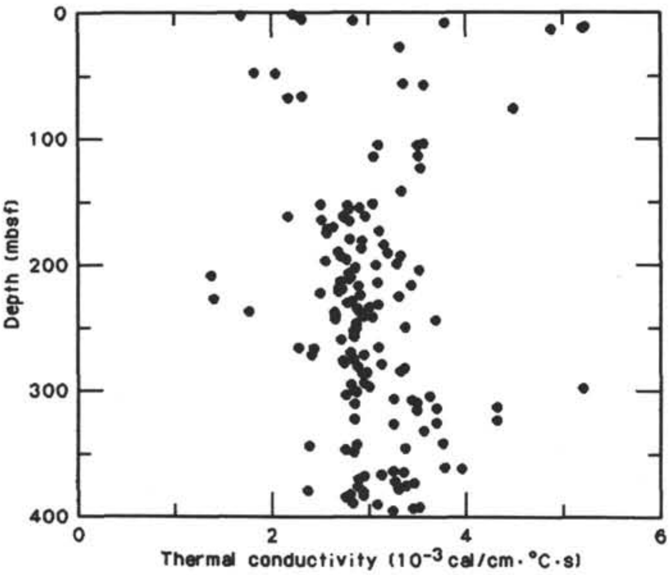

Figure 28. Thermal conductivity vs. depth at Site 717.

4. One of the main controls on sedimentation appears to have been sea-level variation (low stands for the silt turbidites, high stands for the mud turbidites). A second important control was probably changes in rates of erosion related to particular phases of Himalayan uplift. Local tectonic effects, perhaps related to intraplate deformation, may have resulted in the more local supply of biogenic turbidites from seismically triggered slumps on adjacent seamounts.

REFERENCES

Berggren, W. A., Kent, D. V., and van Couvering, J. A., 1985. The Neogene: Part 2, Neogene geochronology and chronostratigraphy. *In* Snelling, N. J. (Ed.), The Chronology of the Geological Record. *Geol. Soc. (London) Mem.* 10:211–260.

Blanc, G., Boulegue, J., Badaut, D. and Stouff, P., 1986. Premiers résultats de la campagne oceanographique Hydrotherm du Marion Dufresne sur la fosse Atlantis II. *C. R. Acad. Sci.* Paris, 302:175–180.

Bukry, D., 1985. Tropical Pacific silicoflagellate zonation and paleotemperature trends of the Cenozoic. *In* Mayer, L., Theyer, F., et al., *Init. Repts. DSDP*, 85: Washington (U.S. Govt. Printing Office), 477–497.

Claypool, G. E., and Kaplan, I. R., 1974. The origin and distribution of methane in marine sediments, *In* Kaplan, I. R. (Ed.), *Natural Gases in Marine Sediments*: New York (Plenum), 94–129.

Curray, J. R. and Moore, D. G., 1971. Growth of the Bengal deep-sea fan and denudation of the Himalayas. *Geol. Soc. Am. Bull.*, 82: 563–572.

Curray, J. R., Emmel, F. J., Moore, D. G. and Raitt, R. W., 1982. Structure, tectonics and geological history of the northeastern Indian Ocean. *In* Nairn, A.E.M., and Stehli, F. G. (Eds.), *The Ocean Basins and Margins* (Vol. 6). *The Indian Ocean*: New York (Plenum Press), 399–450.

Degens, E. T., and Mopper, K., 1976. Factors controlling the distribution and early diagenesis of organic material in marine sediments. *In* Rilley, J. P., and Chester, R. (Eds.), *Chemical Oceanography*: New York (Academic Press), 6:60–114.

Geller, C. A., Weissel, J. K., and Anderson, R. N., 1983. Heat transfer and intraplate deformation in the central Indian Ocean. *J. Geophys. Res.*, 88:1018–1032.

Gieskes, J., and Petersman, G., 1986. Water chemistry procedures aboard *JOIDES Resolution*—Some comments. *ODP Technical note*, 5:46.

Kvenvolden, K. A., and McDonald, T. J., 1986. Organic geochemistry aboard *JOIDES Resolution*, an assay. *ODP Technical Note* 6:5–6.

Ling, H. Y., 1975. Radiolaria: Leg 31 of the Deep Sea Drilling Project. *In* Karig, D. E., Ingle, J. C., et al., *Init. Repts. DSDP*, 31: Washington (U.S. Govt. Printing Office), 703–761.

Locker, S., and Martini, E., 1986. Silicoflagellates and some sponge spicules from the southwest Pacific, Deep Sea Drilling Project, Leg 90. *In* Kennett, J. P., von der Borch, C. C., et al., *Init. Repts. DSDP*, 90, Pt. 2: Washington (U.S. Govt. Printing Office), 887–924.

Moore, D. G., Curray, J. R., Raitt, R. W., and Emmel, F. J., 1974. Stratigraphic-seismic section correlation and implications to Bengal fan history. *In* Von der Borch, C. C., Sclater, J. G., et al., *Init. Repts. DSDP*, 22: Washington (U.S. Govt. Printing Office), 403–412.

Okada, H., and Bukry, D., 1980. Supplementary modification and introduction of code numbers to the low latitude coccolith biostratigraphic zonation (Bukry, 1973; 1975). *Mar. Micropaleont.*, 5:321–325.

Parsons, B., and Sclater, J. G., 1977. An analysis of the variation of ocean floor bathymetry and heat flow with age. *J. Geophys. Res.*, 82:803–827.

Perch-Nielsen, K., 1985. Silicoflagellates. *In* Bolli, H. M., Saunders, J. B., and Perch-Nielsen, K. P., *Plankton Stratigraphy*: Cambridge, U.K. (Cambridge University Press), 811–846.

Powell, C.M.A., and Conaghan, P. J., 1973. Plate tectonics and the Himalayas. *Earth Planet. Sci. Lett.*, 20:1–12.

Richards, A. F., 1962. Investigations of deep sea sediment cores II: Mass physical properties. U.S. Navy Hydrographic Office, *Tech. Rep.* 106:146.

Sayles, F. L., and Manheim, F. T., 1975. Interstitial solutions and diagenesis in deeply buried marine sediments: results from the Deep Sea Drilling Project. *Geochim. Cosmochim. Acta*, 39:103–127.

Sclater, J. G., and Fisher, R. L., 1974. The evolution of the east central Indian Ocean with emphasis on the tectonic setting of the Ninety East Ridge, *Geol. Soc. Am. Bull.*, 85:683–702.

Sclater, J. G., Luyendyk, B. P., and Meinke, L., 1976. Magnetic lineations in the southern part of the Central Indian Basin. *Geol. Soc. Am. Bull.*, 87:371–378.

Skempton, A. W., 1970. The consolidation of clay by gravitational compaction. *Q. J. Geol. Soc. London*, 125:373–411.

Stein, S., and Okal, E. A., 1978. Seismicity and tectonics of the Ninety East Ridge area: Evidence for internal deformation of the Indian plate. *J. Geophys. Res.*, 83:2233–2245.

Thompson, R. W., 1974. Mineralogy of sands from the Bengal and Nicobar Fans, sites 218 and 211, eastern Indian Ocean. *In* von der Borch, C. C., Sclater, J. G., et al., 1974. *Init. Repts. DSDP*, 22: Washington (U. S. Govt. Printing Office), 711–714.

Tissot, B. P., and Welte, D. H., 1984. *Petroleum Formation and Occurrence* (2nd Ed.): Berlin (Springer-Verlag), 699.

Weissel, J. K., Anderson, R. N., and Geller, C. A., 1980. Deformation of the Indo-Australian plate. *Nature*, 287:284–291.

Ms 116A-105

Table 12. Thermal conductivity measurements from Site 717.

Core-Sect.	Interval (cm)	Depth (mbsf)	Conductivity 10^{-3} cal/ (°C · cm · s)
Hole 717B			
01H-1	115	001.15	02.2310
01H-2	063	002.13	01.6957
01H-3	063	003.63	02.3159
02H-1	115	005.15	02.3282
02H-2	063	006.13	02.8586
02H-3	115	008.15	03.8068
02H-5	115	011.15	05.2592
02H-6	063	012.13	05.2333
02H-7	030	013.30	04.9084
Hole 717C			
04X-1	025	027.25	03.339
06X-1	147	047.47	01.831
06X-2	052	048.02	02.053
07X-1	063	056.03	03.374
07X-2	003	057.30	03.587
08X-1	115	066.13	02.329
08X-2	085	067.35	02.186
10X-1	140	075.93	04.517
14X-1	070	103.70	03.588
14X-2	040	104.90	03.115
14X-2	079	105.29	03.520
15X-1	120	113.70	03.526
15X-2	025	114.25	03.065
16X-1	115	123.15	03.551
19X-1	063	141.63	03.353
20X-1	115	151.65	03.058
20X-2	003	152.03	02.518
20X-2	063	152.63	02.797
20X-3	110	154.60	02.921
20X-4	054	155.54	02.812
21X-1	115	161.15	02.758
21X-2	003	161.53	02.181
21X-2	005	161.55	02.981
21X-2	063	162.13	02.758
21X-3	115	164.15	02.528
21X-4	063	165.13	02.816
22X-1	038	169.88	02.647
22X-2	038	171.38	02.587
22X-3	052	173.02	03.125
22X-4	046	174.46	02.582
23X-1	046	179.46	02.822
23X-2	033	180.83	02.949
23X-4	040	183.90	03.175
23X-6	040	186.90	02.941
24X-1	115	189.65	02.702
24X-2	062	190.62	03.215
24X-3	115	192.65	03.351
24X-4	062	193.62	02.733
24X-5	115	195.65	02.785
24X-6	062	196.62	02.567
25X-1	115	199.15	03.305
25X-2	062	200.12	03.089
25X-3	115	202.15	02.875
25X-4	062	204.12	03.538
25X-5	115	206.65	02.808
26X-1	115	208.65	01.381
26X-2	062	209.62	02.830
26X-3	062	211.12	02.806
26X-4	113	213.13	02.719
26X-5	063	214.13	03.106
26X-5	115	216.13	03.453
26X-7	028	216.88	02.908
27X-1	115	218.15	02.709
27X-2	063	219.13	02.738
27X-3	115	221.15	02.703
27X-4	063	222.13	02.513
27X-5	115	224.15	02.929
27X-6	063	225.15	03.327
28X-1	115	227.15	01.410
28X-2	063	228.63	02.843
28X-3	115	230.15	02.791
28X-4	063	231.63	03.115
28X-5	115	233.65	03.025
28X-6	040	234.40	02.896
29X-1	113	237.13	01.776
29X-1	149	237.49	02.659
29X-2	060	238.10	02.930
29X-3	113	240.13	02.672
29X-4	060	241.10	02.966
29X-4	113	241.63	03.054
29X-5	115	243.15	02.668
29X-6	063	244.13	03.708
30X-1	115	246.65	02.889
30X-2	063	247.63	02.889
30X-3	115	249.65	03.393
30X-4	063	250.63	02.889
30X-5	115	252.65	02.861
30X-6	063	253.63	02.866
31X-2	061	257.11	02.865
31X-2	148	259.48	02.731
32X-1	113	265.63	03.118
32X-1	148	265.98	02.292
32X-2	061	266.61	02.451
32X-3	115	271.65	02.427
32X-4	062	269.62	02.830
32X-5	115	271.65	02.968
33X-1	115	275.15	02.860
33X-2	062	276.12	02.753
33X-3	115	278.15	02.763
33X-4	062	279.12	03.152
33X-5	115	281.15	02.904
33X-6	062	282.12	03.388
34X-1	115	284.65	03.344
34X-2	062	285.62	02.999

Table 12 (continued).

Core-Sect.	Interval (cm)	Depth (mbsf)	Conductivity 10^{-3} cal/ (°C · cm · s)
34X-3	115	287.12	02.955
35X-1	115	294.15	02.969
35X-2	062	295.12	02.832
35X-3	115	297.15	03.021
35X-4	062	298.12	05.236
35X-5	115	300.15	02.866
35X-6	062	301.12	02.888
36X-1	115	303.65	02.777
36X-2	062	304.62	03.648
36X-3	115	306.65	03.273
36X-4	062	307.62	03.462
36X-5	115	309.65	03.514
36X-6	062	310.62	02.868
37X-1	115	313.15	04.344
37X-2	062	314.12	03.717
37X-3	062	315.62	03.513
38X-1	115	322.65	02.868
38X-2	062	323.62	04.344
38X-3	115	325.65	03.717
38X-4	062	326.62	03.273
39X-1	095	331.95	03.587
40X-1	115	341.65	03.784
40X-2	062	342.62	02.894
40X-3	115	343.65	02.401
40X-4	062	345.62	03.394
40X-5	115	346.65	02.775
40X-6	062	348.62	02.863
42X-1	115	360.65	03.804
42X-2	062	361.62	03.982
42X-3	115	363.65	03.271
42X-4	062	364.62	03.378
42X-5	115	366.65	03.149
42X-6	063	367.62	02.972
43X-1	115	370.15	02.915
43X-2	062	372.12	03.291
43X-3	115	373.15	03.488
43X-4	062	375.12	03.405
43X-5	115	376.15	02.906
43X-6	062	378.12	03.322
44X-1	068	379.18	02.383
44X-2	068	380.18	02.959
44X-3	068	382.18	02.823
44X-4	075	383.25	02.959
44X-4	148	384.48	02.774
45X-1	113	389.13	02.849
45X-2	061	390.11	03.103
45X-3	115	392.15	03.541
45X-4	062	393.12	03.471
45X-5	114	395.14	03.263

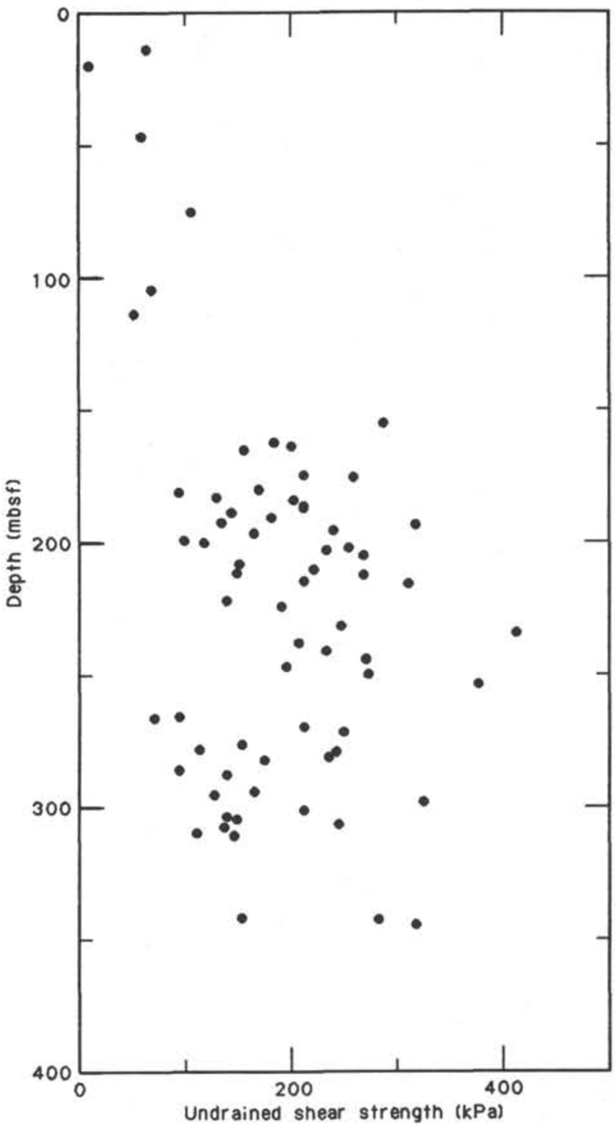

Figure 29. Undrained shear strength vs. depth at Site 717.

Table 13. Shear-strength measurements from Site 717, Hole C.

Core	Sect.	Int. (cm) top	bot.	Depth (mbsf)	Shear strength (kPa)
2H	1	36	38	13.86	63.8
2H	3	53	55	20.0	9.5
6X	1	77	79	46.77	59.1
10X	1	80	82	75.30	106.4
14X	2	20	22	104.70	68.6
15X	1	131	131	113.81	52.0
20X	4	15	17	155.15	288.4
21X	2	89	91	162.39	184.4
21X	3	77	79	163.77	201.0
21X	4	72	74	165.22	156.0
22X	4	78	80	174.78	212.8
22X	5	11	13	175.61	260.1
23X	1	110	112	180.10	170.2
23X	2	59	61	181.09	94.6
23X	3	105	107	183.05	130.0
23X	4	57	59	184.07	203.3
23X	5	128	130	186.28	212.8
23X	6	57	59	187.07	212.8
24X	1	30	32	188.80	144.2
24X	2	66	68	190.66	182.1
24X	3	110	112	192.60	134.8
24X	4	55	57	193.55	319.2
24X	5	110	112	195.60	241.2
24X	6	55	57	196.55	165.5
25X	1	120	122	199.20	99.3
25X	2	58	60	200.08	118.2
25X	3	110	112	202.10	255.3
25X	4	57	59	203.07	234.1
25X	5	110	112	205.10	269.5
26X	1	65	65	208.15	151.3
26X	2	122	122	210.22	222.2
26X	3	110	112	211.60	149.0
26X	4	42	44	212.42	269.5
26X	5	110	112	214.60	212.8
26X	6	72	74	215.72	312.1
27X	4	50	52	222.00	139.5
27X	5	120	122	224.20	191.5
28X	4	73	75	231.73	248.3
28X	6	34	36	234.34	413.8
29X	2	60	62	238.10	208.1
29X	4	68	70	241.18	234.1
29X	6	71	73	244.21	271.9
30X	1	130	132	246.80	196.2
30X	3	124	126	249.74	274.3
30X	6	59	61	253.59	378.3
32X	1	110	112	265.60	94.6
32X	2	16	18	266.16	70.9
32X	4	58	60	269.58	212.8
32X	5	108	110	271.58	250.6
33X	2	72	74	276.22	153.7
33X	3	110	112	278.10	113.5
33X	4	57	59	279.07	243.5
33X	5	110	112	281.10	236.4
33X	6	56	58	282.06	175.0
34X	2	86	88	285.86	94.6
34X	3	110	112	287.60	139.5
35X	1	110	112	294.10	165.5
35X	2	83	85	295.33	127.7
35X	4	60	62	298.10	326.3
35X	6	69	71	301.19	212.8
36X	1	110	110	303.60	139.5
36X	2	57	59	304.57	149.0
36X	3	110	112	306.60	245.9
36X	4	57	59	307.57	137.1
36X	5	120	122	309.70	111.1
36X	6	70	72	310.70	146.6
40X	1	130	132	341.80	153.7
40X	2	47	49	342.47	283.7
40X	3	95	97	344.45	319.2

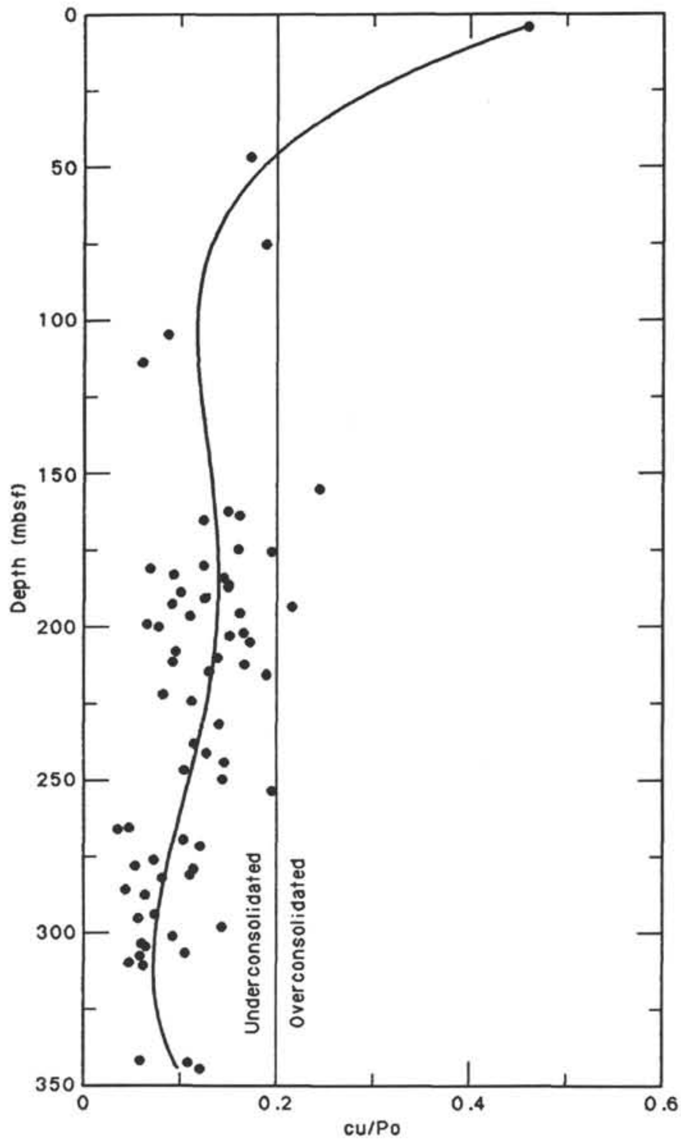

Figure 30. Ratio of undrained shear strength (cu) to effective overburden pressure (P_o) vs. depth at Site 717. Sediments with a ratio of less than 0.2 are underconsolidated.

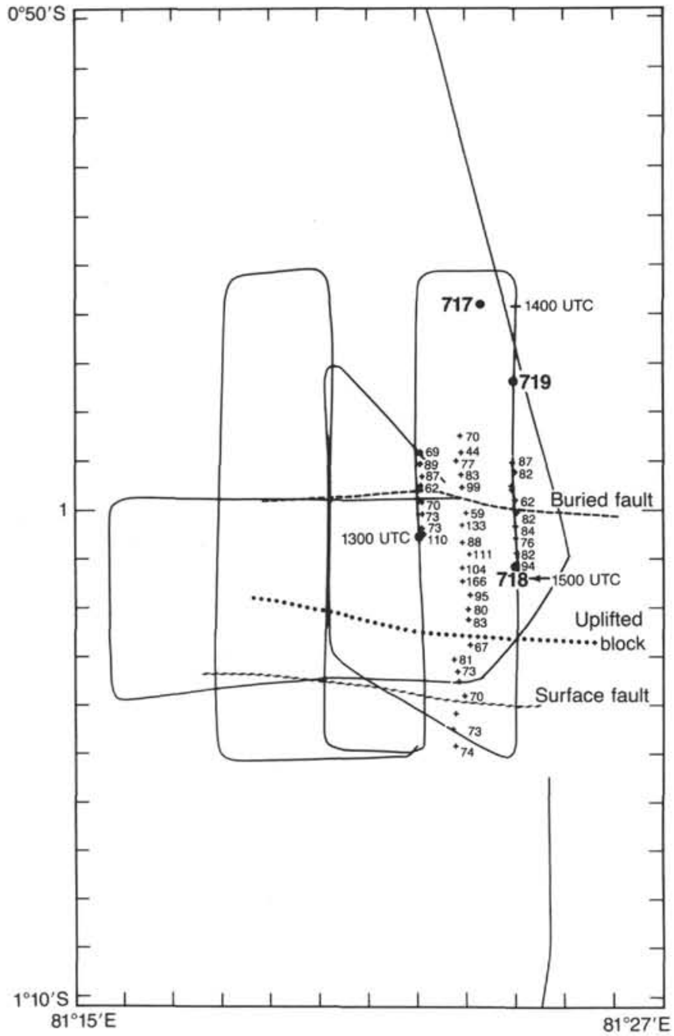

Figure 31. Site survey carried out in 1986 on board *Robert D. Conrad*. Heat-flow stations are shown by small crosses with value in mW/m^2. Locations of Sites are shown by large dots. Also shown are locations of seismic reflection lines (solid lines).

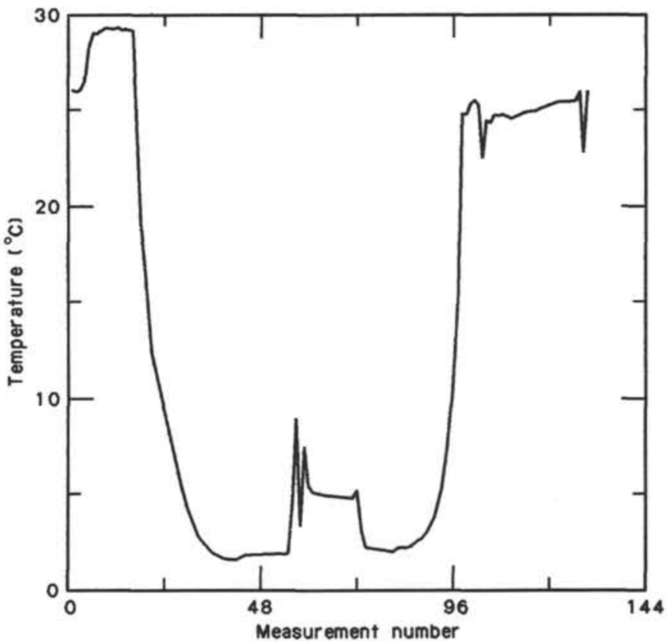

Figure 32. Temperature vs. time record obtained with the T-probe during Core 116-717C-9I.

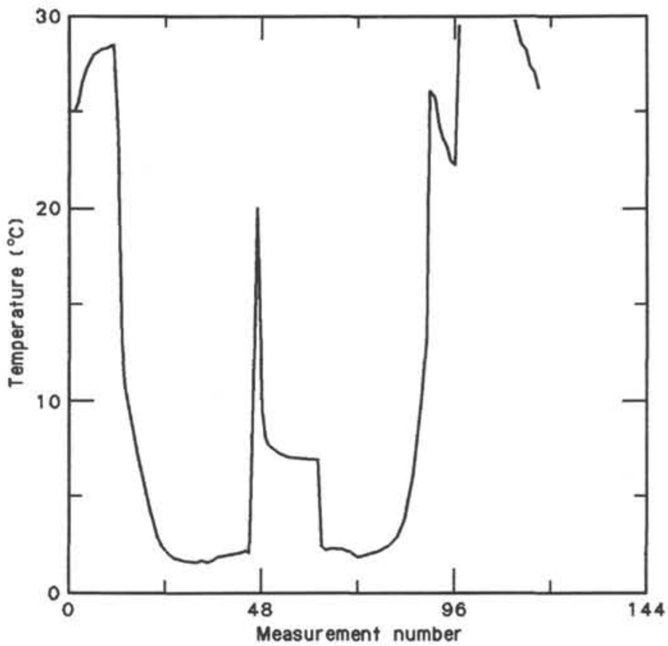

Figure 33. Temperature vs. time record obtained with the T-probe during Core 116-717C-17I.

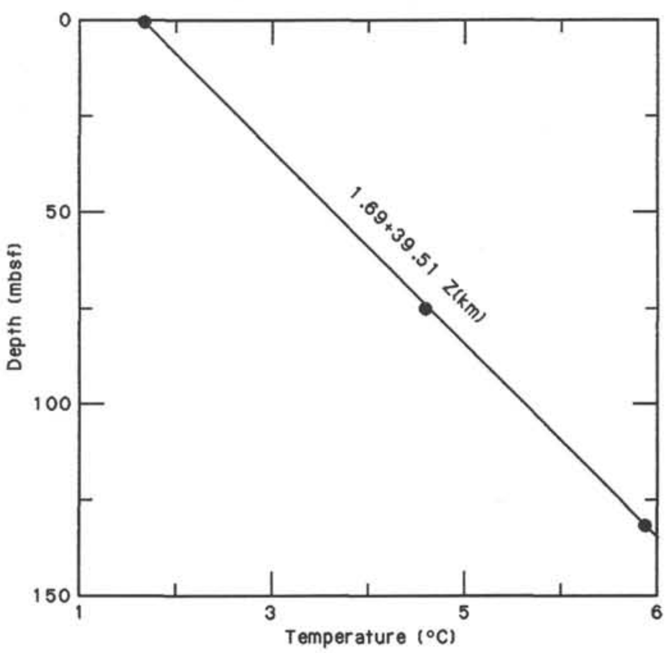

Figure 34. Temperature in Hole 717C vs. depth. Line is the geothermal gradient determined by a least-squares fit to a straight line.

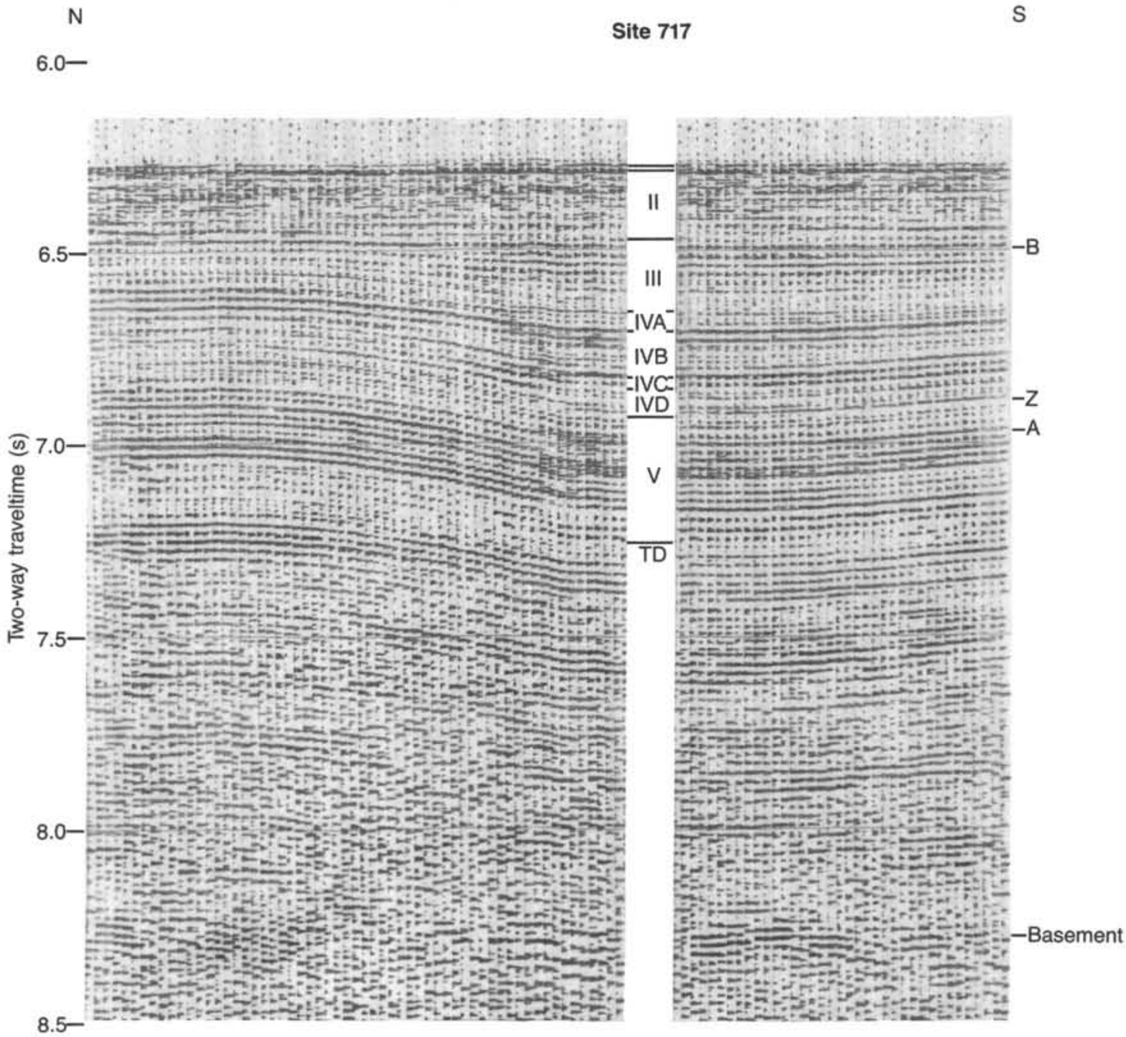

Figure 35. Single-channel seismic reflection line obtained by *JOIDES Resolution* on the final approach to Site 717. Lithologic units from Hole 717C are shown at Site 717 with depths to lithologic boundaries converted to two-way traveltime. The position of the lithologic boundaries in the seismic section were determined by tracing reflectors from Site 719, where a tie between the cores and the seismic section was obtained from a synthetic seismogram constrained by well-log data. Unconformities "A" and "B" and Reflector "Z" discussed in text are noted to the right of the profile. Total length of the seismic section shown is about 5 km.

NOTE: All core description forms ("barrel sheets") and core photographs have been printed on coated paper and bound as Section 3, near the back of the book, starting on page 213.